Properties of Tellurium based II-VI semiconducting materials

Mullins, J.T.

PROPERTIES OF TELLURIUM BASED II-VI SEMICONDUCTING MATERIALS

by

J.T. Mullins, B.Sc.

A Thesis Submitted for the
Degree of Doctor of Philosophy
in the University of Durham

April 1990

ABSTRACT

Opto-electronic devices operating as radiation detectors in the infra-red region of the electromagnetic spectrum are currently of interest. By operating in the infra-red, particularly in the 8-12 μm wavelength range, it is possible to detect the infra-red radiation emitted by objects at ordinary temperatures and so to image in darkness. Furthermore, at such wavelengths, vision is also possible in mist, fog or smoke.

Semiconducting materials which have an energy gap corresponding to the photon energy of the radiation of interest are suitable for fabricating such devices. The growth and characterisation of two such materials, both formed from elements in groups IIB and VIA of the periodic table and generally refered to as II-VI compounds, forms the subject matter of this thesis.

The first of these materials is the ternary compound mercury cadmium telluride ((Hg,Cd)Te). This is a well established infra-red material and was grown for this work in thin film form by Metal Organic Vapour Phase Epitaxy (MOVPE) using the Inter-diffused Multilayer Process (IMP). The resulting layers were characterised optically and electrically and were shown to be of excellent compositional uniformity, an important consideration for infra-red devices, but to contain extremely high acceptor concentrations in the as grown state. These high acceptor concentrations were attributed to mercury vacancies present due to the inherent weakness of the material. Fitting of the electrical data obtained from p-type samples using a multicarrier/multilayer transport model suggested that the mercury vacancy concentrations were also highly non-uniform.

A more novel alternative to (Hg,Cd)Te is the HgTe:ZnTe superlattice system. By forming a superlattice from the two constituent binary compounds, rather than alloy, quantum confinement and strain effects may, in principle, be used to tailor the optical and electronic properties to some extent independently of the composition. The resulting material may also be structurally more stable than an equivalent alloy. Here the development of a thermal MOVPE growth process for this superlattice system is described and it is shown that such superlattices may be preferable to the equivalent alloys as they are easier to grow by MOVPE. Initial structural and optical studies and theoretical calculations have confirmed the suitability of MOVPE for the growth of this superlattice system and its applicability for infra-red applications.

DECLARATION

I declare that the work reported in this thesis, unless otherwise stated, was carried out by the candidate, that it has not previously been submitted for any degree and that it is not currently being submitted for any other degree.

ACKNOWLEDGEMENTS

This thesis would not be complete without mention of all those who contributed to the work described in it. Thanks are due to Prof. J. Woods for providing me with the opportunity of performing this work at Durham. I would also like to thank British Aerospace plc. for my financial support. Dr. A.W. Brinkman and the late Dr. G.J. Russell provided day to day support. All of the work described in this thesis was performed in close collaboration with the other members of the MOVPE team. Janet Hails originally constucted the MOVPE equipment for the growth of HgTe, CdTe and (Hg,Cd)Te and subsequently modified it to allow the growth of ZnTe and MnTe. Janet was in charge of the MOVPE equipment during the initial phase of my work on (Hg,Cd)Te. The later work on (Hg,Cd)Te and all of the work on ZnTe and HgTe:ZnTe and CdTe:ZnTe superlattices was performed in conjunction with Paul Clifton who had responsibility for the MOVPE reactor during that phase of the work. The contributions made by Paul Brown with TEM studies and David Hall with electronic structure calculations are also gratefully acknowledged. Many seemingly daunting tasks were made possible by the technical, workshop and secretarial staff of the department. In addition, Ken Durose at Durham and many friends at R.S.R.E. Malvern and at the University of Hull provided an enormous amount of helpful advice and discussion and were always willing to divert their various experimental specialities to 'look' at my samples.

CONTENTS

1. Properties of Tellurium Based II-VI Materials

1.1 Introduction

This thesis is concerned with the properties of tellurium based II-VI materials. Of particular interest are the tellurides of mercury (HgTe), cadmium (CdTe) and zinc (ZnTe), together with some of their related alloys and superlattices. The work was initially driven by a requirement for the electrical and optical characterisation of epitaxial layers of the narrow-gap ternary alloy mercury cadmium telluride ((Hg,Cd)Te) and this forms a major part of the thesis. (Hg,Cd)Te had been grown at Durham for approximately two years prior to the commencement of the work reported here and extensive structural studies had already been performed on this material. During the course of this work, the growth system was upgraded to enable the growth of ZnTe. This was done with the intention of developing growth techniques for and then characterising zinc telluride and mercury zinc telluride. The characterisation of ZnTe is also reported in this thesis although the growth of (Hg,Zn)Te was rejected as impractical. The other major part of the work described here is the development of the growth techniques for, and the initial characterisation of, superlattices formed from the binary compounds HgTe and ZnTe and from CdTe and ZnTe. By forming a superlattice structure consisting of alternating layers of two semiconductor materials which are thin compared to the wavelength of an electron, it is possible to effectively create a new material, as proposed by Esaki and Tsu[1] and Esaki[2] , the properties of which may be tailored by appropriate choice of the thicknesses of the constituent compounds. The HgTe:ZnTe superlattices considered here were designed to be narrow-gap materials and were investigated as possible alternatives to (Hg,Cd)Te for devices operating at infra-red wavelengths. In contrast, the CdTe:ZnTe superlattices have potential for devices operating at visible wavelengths[3] although they are considered here from the point of view of providing buffer layers for HgTe:ZnTe superlattices.

All of the samples considered here were grown, mainly at Durham, by Metal Organic Vapour Phase Epitaxy (MOVPE). This technique involves the growth of thin crystalline layers of the required materials onto suitable substrates. The component elements are supplied to the substrate in the vapour phase generally in the form of metal-organic compounds which are thermally cracked to release the required elements for growth. In general, vapour phase epitaxial techniques are favoured for the growth of infra-red materials for the following reasons[4] :

1. Growth may be achieved at temperatures significantly below the materials' melting point.

2. Epitaxial layers may be grown on foreign substrates which may be of higher structural quality than the native bulk grown material.

3. Growth may be performed on substrates which offer integrated circuit capability, such as GaAs or Si.

4. In-situ doping and the growth of heterojunctions and multilayer structures is possible.

It is the flexibility, low growth temperatures and high degree of control offered by MOVPE which makes the growth of the superlattices considered in this work possible.

In this chapter, an overview of the properties of the materials considered in this thesis is presented. All of the binary and ternary compounds of interest crystallise in the sphalerite structure and so this is described in section 1.2. The properties and applications of (Hg,Cd)Te are described in section 1.3. The HgTe:ZnTe and CdTe:ZnTe superlattices referred to above are examples of strained layer superlattices and so in section 1.4, structural aspects of the growth of strained layer systems in general are presented. A description of the electronic properties of HgTe based superlattices is given in section 1.5. Finally, in section 1.6, the contents of this thesis are described.

1.2 The Sphalerite Structure

The sphalerite structure[5] is illustrated in Fig.1.1. The cations (Hg, Cd or Zn) and anions (Te) both sit on separate interpenetrating face-centered cubic lattices which are separated from each other by $\frac{1}{4}$ body diagonal. Bonding between the ions is tetrahedral as in the diamond structure. In this structure, the {111} oriented planes are close packed. It is important to note that there are two distinct types of {111} planes: those comprising close packed planes of the cation and those corresponding to close packed planes of the anion. This is illustrated in Fig.1.2. Following the convention of Gatos and Levine[6] , the cation planes are labelled {111}A while the tellurium planes are designated $\{\bar{1}\bar{1}\bar{1}\}$B. It is of considerable practical importance to be able to determine which face of a {111} orientated wafer is the A face and which is the B face, as the nucleation and growth of epitaxial layers may be significantly different on these two opposite polar faces.

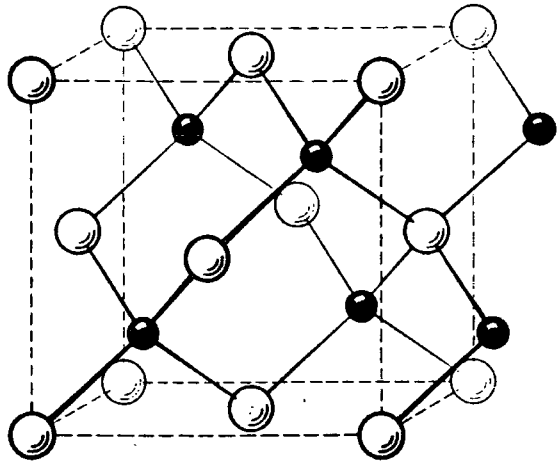

Fig.I.1. The Sphalerite Structure.

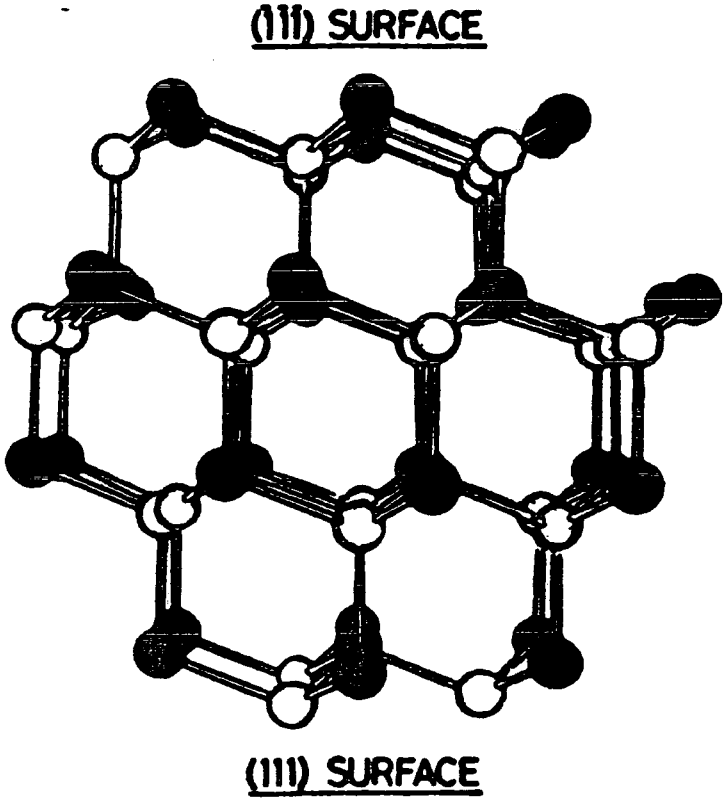

Fig.I.2. Polarity in the sphalerite structure.

The stacking of close packed planes to form the sphalerite structure may be described using the notation of Roth[7] . Stacking of the constituent ions on the three possible sites for tetrahedral bonding is denoted by:

$$a\alpha b\beta c\gamma a\alpha b\beta c\gamma....$$

where Roman letters refer to one type of close packed planes and the Greek letters refer to the other.

A common defect in sphalerite materials occurs when this stacking sequence is altered to:

$$a\alpha b\beta c\gamma b\beta a\alpha c\gamma....$$

This defect is termed a first order twin and has a low energy of formation as it involves only slight alteration of the tetrahedral bonding.

1.3 Mercury Cadmium Telluride ($Hg_{1-x}Cd_xTe$)

The ternary alloy $Hg_{1-x}Cd_xTe$ offers a room temperature energy gap which is direct and tunable between that of the semimetallic HgTe at -0.14 eV and that of CdTe at 1.5 eV[8] , by appropriate choice of the mole fraction of cadmium (x). One advantage of this alloy is that the lattice parameters of HgTe and CdTe differ by only 0.3%[9] and so changes in the composition, and hence energy gap, of the alloy do not alter its lattice parameter greatly thus simplifying growth and the choice of substrate. The principal application of this material is for infra-red detector devices with operating wavelengths in the 10-14 μm ($x = 0.2$) and 3-5 μm ($x = 0.3$) atmospheric windows where such devices offer the best detectivity currently attainable[10] .

The electronic structure of $Hg_{1-x}Cd_xTe$[11] is shown in Fig.1.3. For $x <\sim 0.1$ the Γ_6 conduction-like band lies below the Γ_8 valence-like band and the material is semimetallic, like HgTe, with a negative $\Gamma_6 - \Gamma_8$ energy gap. As the proportion of Hg is reduced, the energy gap increases and the material becomes a semiconductor with an electronic structure similar to other sphalerite semiconductors such as GaAs. As indicated in Fig.1.3., the electron effective mass varies with the energy gap, having a minimum at the zero gap crossing.

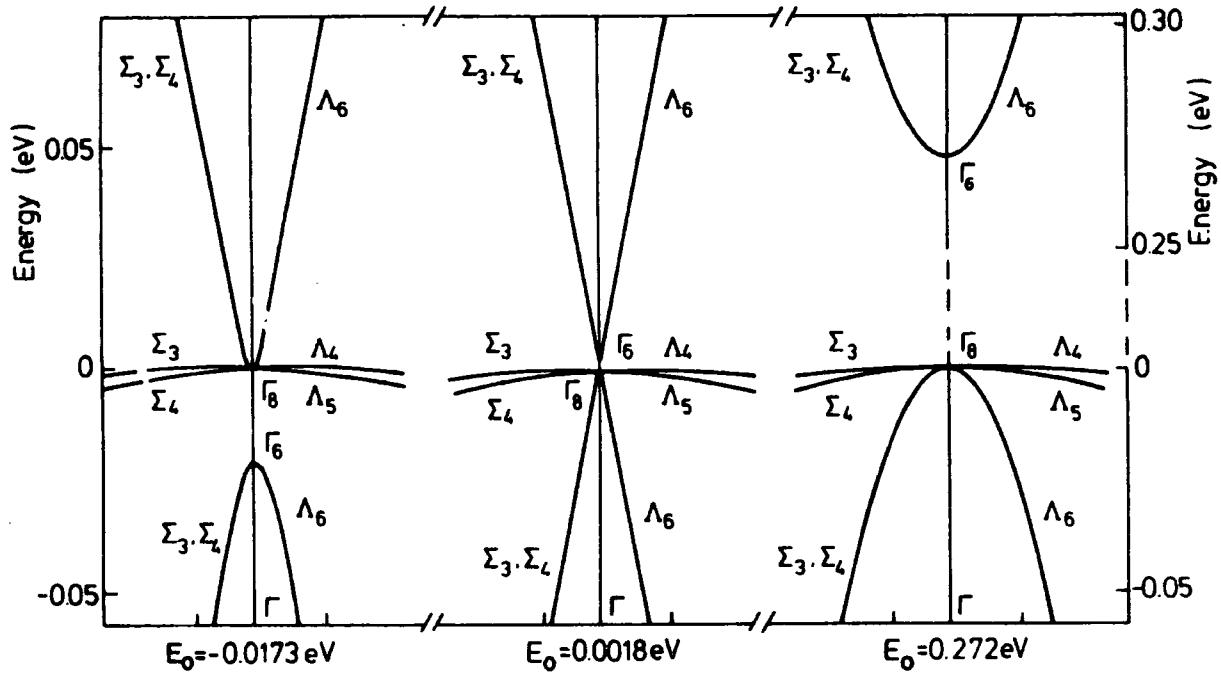

Fig. 1.3 The electronic structure of $Hg_{1-x}Cd_xTe$ for three different values of the $\Gamma_6 - \Gamma_8$ energy gap.

1.4 Lattice Mismatched and Strained Layer Systems

The HgTe:ZnTe and CdTe:ZnTe superlattices referred to in the introduction together with epitaxial layers of ZnTe grown on GaAs are all examples of lattice mismatched systems. Table 1.1 gives the lattice parameters of all of the binary materials of interest in this thesis together with the lattice mismatches between them. Considering first the case of a material with a cubic structure having a lattice parameter a_1 grown epitaxially onto a cubic substrate with a lattice parameter a_0, the mismatch f between the two materials may be defined as:

$$f = \frac{2(a_0 - a_1)}{a_0 + a_1} \tag{1.1}$$

If its thickness is not too great, an epitaxial layer may grow coherently with the substrate[12] , as shown in Fig.1.4(a). In this case, the layer will be biaxially stressed and has an in-plane lattice parameter equal to that of the substrate, assuming that the substrate is thick enough to be unaffected by the stress. Thus, the unit cell of the layer is tetragonally distorted with the strain in the in-plane directions being approximately equal to f for small strains. If, however, the thickness of the layer is beyond some critical value, determined by the magnitude of the strain and the elastic properties of the layer, then it becomes energetically favourable for the layer to relax towards its unstrained or freestanding lattice parameter by the generation of misfit dislocations at the interface between the layer and the substrate. This is illustrated in Fig.1.4(b). The presence of these misfit dislocations at the interface will probably be associated with the presence of threading dislocations which propagate through the layer and reduce its structural quality. Such threading dislocations may grow out as the layer thickness increases and it may be possible to obtain active layers of sufficient quality on mismatched substrates if they are sufficiently thick. Alternatively, a passive buffer layer, lattice matched to the required active layer can be grown and used to grow out most of the threading dislocations before growing the active layer itself.

For the case of a superlattice, the two component materials may be lattice mismatched with respect to each other and either or both may be mismatched with respect to the substrate or buffer layer on which it is grown. It is possible to define a free standing in-plane lattice parameter for the superlattice which depends only on the thicknesses

		lattice mismatches (%)				
	a_0 (Å)	HgTe	CdTe	ZnTe	GaSb	GaAs
HgTe	6.462		0.3	5.7	5.8	13
CdTe	6.481			6.0	6.1	14
ZnTe	6.101				0.1	7.6
GaSb	6.095					7.5
GaAs	5.653					

Table 1.1 Lattice constants (a_0) and lattice mismatches.

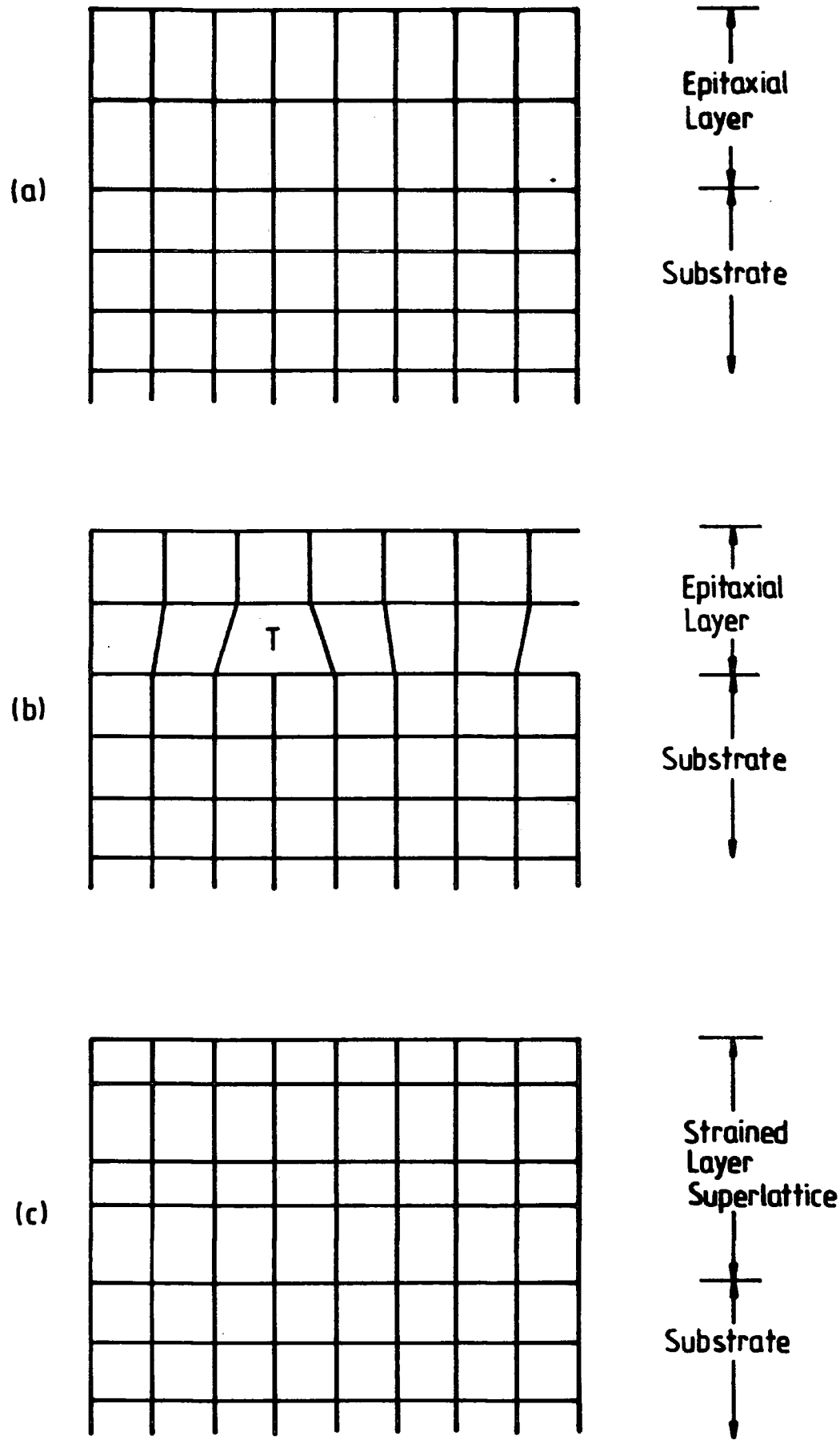

Fig.1.4. Lattice Mismatched Growth. (a) Coherently strained epitaxial layer. (b) Relaxed epitaxial layer. (c) Strained Layer Superlattice.

and elastic properties of the component layers and is the in-plane lattice parameter which the superlattice would have if it were free from any substrate and the individual layers were coherently strained. The individual layers may be strained to have the same in-plane lattice parameter as the substrate if the critical thickness for the required degree of strain is not exceeded for either of the constituent layers, and if the superlattice as a whole does not exceed the critical thickness dictated by the mismatch between the substrate and the free standing lattice parameter of the superlattice. If the substrate or buffer layer is exactly lattice matched to the free standing in-plane lattice parameter of the superlattice then, in principle, growth of the superlattice may be continued to any desired thickness without the generation of misfit defects regardless of the mismatch between the component layers provided that each layer is below its critical thickness for the required strain[13] . This is illustrated in Fig.1.4(c). If the superlattice is mismatched with the substrate and beyond its critical thickness for that degree of strain then it may break away from the substrate and relax to its free standing configuration in a similar way to the single epitaxial layers described above.

Strained layer superlattices are of interest as buffer layers for active semiconducting layers. By tailoring the free standing lattice parameter of the buffer superlattice to that of the active layer, lattice matching may be achieved. Furthermore, the alternating strains present in such a structure may act to bend over dislocations propagating from the substrate/buffer interface[13] .

1.5 HgTe Based Superlattices

In section 1.3, the ternary alloy $Hg_{1-x}Cd_xTe$ was discussed with regard to its application as an infra-red material. In that case, alloying the semimetal HgTe with the semiconductor CdTe produced a material with an intermediate energy gap which could be tuned to the required value by appropriate choice of x. An alternative method of producing a narrow gap material is to grow a superlattice consisting of HgTe wells between barrier layers of a wider gap semiconductor. Quantum confinement and strain effects then act to increase the $\Gamma_6 - \Gamma_8$ energy gap of the HgTe and so may produce a material with a small direct energy gap. The most widely studied example of this is the HgTe:CdTe superlattice system[14] which is closely related to the $Hg_{1-x}Cd_xTe$ alloy. Such superlattices may offer improved hole mobilities[15] and stronger optical absorption[16] than equivalent alloys. Furthermore, the destabilising influence of Cd

on the weak Hg-Te bond in $Hg_{1-x}Cd_xTe$[17] is eliminated by the use of a multilayer structure. This system also has the advantage of employing binary layers which are almost lattice matched, thus relaxing the constraint of critical thickness. However, the extremely high interdiffusion coefficient between these two compounds[18] makes the growth of such low dimensional structures impracticable at the growth temperatures necessary for the thermal MOVPE process used for this work and so requires the much lower temperatures of Molecular Beam Epitaxy (MBE).

Another possible alternative to $Hg_{1-x}Cd_xTe$, and the one considered in this thesis, is the HgTe:ZnTe superlattice system which until the work reported here was performed had only been grown by MBE[19] . For this system, interdiffusion was expected to be much lower than in the HgTe:CdTe system[20] , making growth by thermal MOVPE feasible. There is, however, a large lattice mismatch (6%) between the two constituents which requires that strain is accounted for both in terms of the critical thickness and in the determination of the electronic structure of the material. In Fig.1.5. the effects of quantum confinement and strain on the HgTe well layers in HgTe:ZnTe superlattices are qualitatively illustrated. The HgTe well layers are biaxially compressed by the ZnTe barrier layers and the resulting strain in the HgTe may be resolved into a hydrostatic compression and a uniaxial tension perpendicular to the plane of the layers. Quantum confinement has the effect[21] of moving the Γ_6 conduction-like band up in energy and the Γ_8 valence-like band down in energy, with the light hole Γ_8 band moving to a lower energy than the heavy hole band, thus increasing the energy gap, as does the hydrostatic compression[22] . The uniaxial component of the strain has the effect[22] of splitting the light and heavy hole Γ_8 bands, with the heavy hole band moving up in energy and the light hole band moving down. Accordingly, a direct, positive energy gap may be created between the Γ_6 conduction band and the Γ_8 heavy hole valence band. In addition to this, the strain causes valence band to become anisotropic, as illustrated in Fig.1.6, with the effective mass of the heavy hole derived highest valence band (HH1) becoming greater in the growth direction ($k_|$) and but lower in the in-plane direction ($k_{||}$). For the lower light hole derived valence band (LH1) the effect of strain is reversed and this band becomes light in the growth direction and heavy parallel to the layers. It is of interest to note that, in the case of HgTe:CdTe superlattices, the small strain which does exist in the HgTe wells is in the opposite sense (i.e. biaxial tension).

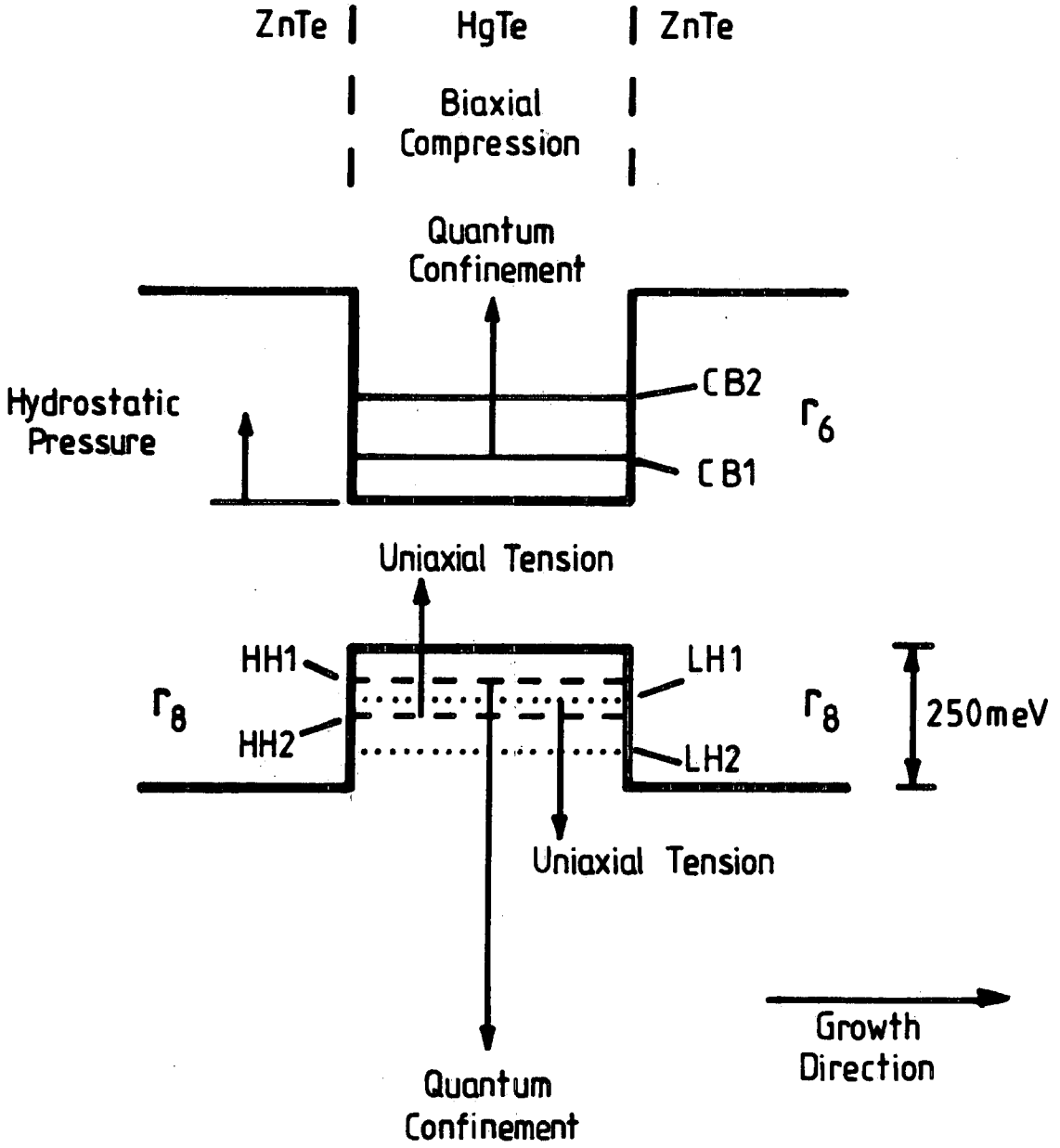

Fig.1.5. The effects of quantum confinement and strain on the HgTe well layers in HgTe:ZnTe superlattices.

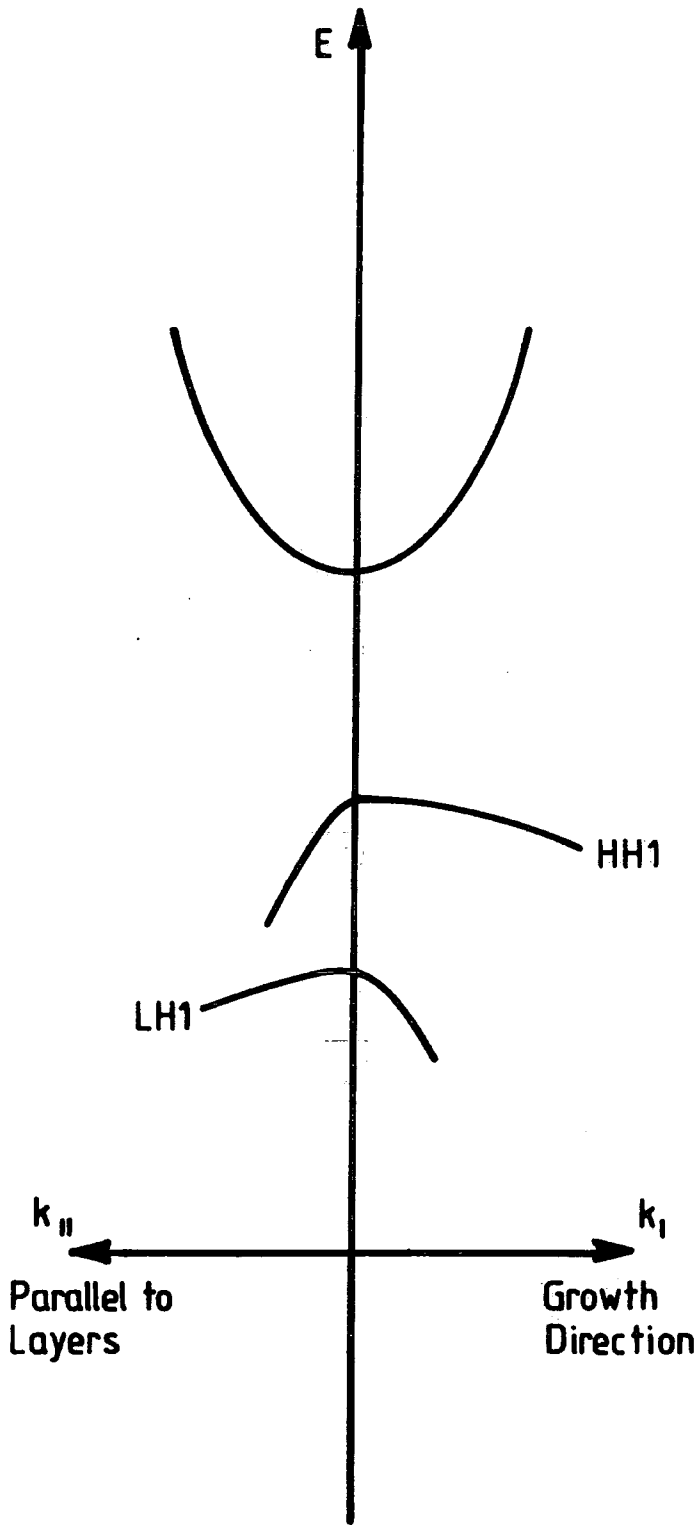

Fig.1.6. Anisotropic valence band structure of HgTe:ZnTe superlattices.

1.6 The Present Work

As described in the introduction, this thesis is concerned with the properties of tellurium based II-VI compounds grown by MOVPE. Accordingly, chapter two is devoted to a description of the MOVPE growth system and the processes used at Durham to grow the materials of interest. In particular, the processes developed during the course of this work for the growth of the superlattices are described and discussed with regard to the applicability of MOVPE to the growth of such structures.

In chapter three, the experimental techniques used to characterise the layers are described. This mainly involves a description of the apparatus which was designed and constructed in order to measure the Hall coefficient and resistivity of epitaxial layers of $Hg_{1-x}Cd_xTe$ as a function of temperature. Techniques used for the optical, structural and compositional analysis of the layers are also briefly outlined.

The electrical transport properties of $Hg_{1-x}Cd_xTe$ are often complicated by the simultaneous contribution of both holes and electrons. A model accounting for such effects and the intrinsic properties of the material which was used to interpret the experimental data from $Hg_{1-x}Cd_xTe$ samples is described in chapter four.

In chapter five, the results of the optical and electrical characterisation of $Hg_{1-x}Cd_xTe$ layers grown during the course of this work are described. The optical data yield information on the composition and quality of the layers, while the electrical data was interpreted using the model described in chapter four to give the carrier concentrations and mobilities in the material. This information is interpreted in the light of the growth conditions.

Chapter six begins with the structural properties of epitaxial layers of ZnTe which were grown as a prerequisite for the growth of the superlattices. The results obtained for the HgTe:ZnTe superlattices are then given. This information is mainly structural although some optical data is also given and interpreted in terms of a calculation of the electronic structure of the superlattice. Finally, some preliminary studies of CdTe:ZnTe superlattices which were of interest as possible buffer layers for HgTe:ZnTe superlattices are reported.

All of the above work is concluded in chapter seven.

REFERENCES

1. L. Esaki and R. Tsu, IBM J. Res. Dev. **Jan.1970** 61.
2. L. Esaki, IEEE Journal of Quantum Electronics **QE-22** (1986) 1611.
3. R.H. Miles, J.O. McCaldin and T.C. McGill, J. Crystal Growth **85** (1987) 188.
4. J.B. Mullin, S.J.C. Irvine, J. Giess, J.S. Gough, A. Royle, M.C.L. Ward and G. Crimes, SPIE **Vol. 1106** Future Infrared Detector Materials (1989) 17.
5. D.B. Holt, J. Mater. Sci., **23** (1988) 1131.
6. H.C. Gatos and M.C. Lavine, J. Electrochem. Soc. **107** (1960) 427.
7. W.L. Roth in Physics and Chemistry of II-VI Compounds, Ed. M. Aven and J.S. Prener, North-Holland (1967).
8. G.L. Hansen, J.L. Schmidt and T.N. Casselman, J. Appl. Phys. **53** (1982) 7099.
9. J.C. Brice in Properties of Mercury Cadmium Telluride, EMIS Datareviews Series No. 3 (1987) Ed. J.C. Brice and P. Capper.
10. C.T. Elliot J. Crystal Growth **72** (1985) 453.
11. H. Overhof, Phys. Stat. Sol. **B 45** (1971) 315.
12. J.W. Matthews and A.E. Blakeslee, J. Crystal Growth **27** (1974) 118.
13. J.W. Matthews and A.E. Blakeslee, J. Crystal Growth **27** (1974) 265.
14. J.P. Faurie, IEEE Journal of Quantum Electronics **QE-22** (1986) 1656.
15. J.P. Faurie, I.K. Sou, P.S. Wijewarnasuriya, S. Rafol and K.C. Woo, Phys. Rev. B **34** (1986) 6000.
16. G.Y. Wu, C. Mailhiot and T.C. McGill, Appl. Phys. Letters **46** (1985) 72.
17. W.E. Spicer, J.A. Silberman, J. Morgan, I. Lindau, J.A. Wilson, A.B. Chen and S. Sher, Phys. Rev. Lett. **49** (1982) 948.
18. J. Tunnicliffe, S.J.C. Irvine, O.D. Dosser and J.B. Mullin, J. Crystal Growth **68** (1984) 245.
19. J.P. Faurie, S. Sivananthan, X. Chu and P.A. Wijewarnasuriya, Appl. Phys. Letters **48** (1986) 785.

20. J.B. Mullin, J. Giess, S.J.C. Irvine, J.S. Gough and A. Royle, Mat. Res. Soc. Symp. Proc. **90** (1987) 367.

21. J.R. Meyer, F.J. Bartoli, C.A. Hoffman and J.N. Schulman, Phys. Rev. B **38** (1988) 12457.

22. E.P. O'Reilly, Semicond. Sci. Technol. **4** (1989) 121.

2. Growth of Epitaxial Layers by MOVPE

2.1 Introduction

As described in section 1.1, it is often desirable to grow semiconducting materials in the form of epitaxial layers. In the case of II-VI materials, the most widely used epitaxial growth techniques are Liquid Phase Epitaxy (LPE), Molecular Beam Epitaxy and MOVPE.

LPE[1] is a relatively simple, well developed, technique which is currently used for the growth of $Hg_{1-x}Cd_xTe$ for device fabrication[2] . In this technique, growth takes place when the substrate is brought into contact with a supersaturated solution containing the required compound. The nature of this technique restricts growth to relatively high temperatures and precludes the use of foreign substrates. Additionally, it is not feasible to grow low dimensional systems or to control the doping of the material in situ.

In contrast, MBE[3] involves the use of molecular or atomic beams which are allowed to impinge on the surface of a substrate where, under suitable conditions of temperature and particle flux, epitaxial growth may take place. Such epitaxy can only take place under Ultra High Vacuum (UHV) and so this technique is extremely complex and expensive. MBE is widely used for research purposes, however, due to its high degree of flexibility. Growth may be performed on foreign substrates and at very low temperatures. In addition, in-situ doping is possible. Low, well controlled, growth rates and the ability to switch rapidly between different sets of source materials allow the growth of heterostructures and low-dimensional systems. The use of molecular or elemental source materials in a UHV environment also assists in the growth of extremely pure material. A disadvantage of this technique for the growth of mercury containing compounds is that extremely high mercury fluxes are required necessitating the use of specially modified reactors and the consumption of large quantities of mercury[4] .

MOVPE offers many of the advantages of MBE with growth at low temperatures, growth on foreign substrates, the growth of heterostructures and low-dimensional systems and in-situ control of doping being possible. In addition growth is performed in a carrier gas stream, rather than under UHV, and so the equipment required is relatively simple. In contrast to the case of MBE, mercury containing compounds may be grown without the problems associated with maintaining a high mercury flux. This

technique does, however, require the development of suitable metal-organic precursors. Furthermore, the growth mechanisms are more complex than in the case of MBE and this may restrict the flexibility of the technique. The use of metal-organic compounds also introduces the possibility of contamination of the epitaxial layers.

In this chapter the growth, by MOVPE, of the epitaxial layers and superlattices considered in chapters five and six is described. After an overview of the principles of MOVPE in section 2.2, the growth system used at Durham is described in section 2.3. Details of the substrate preparation procedures, which are of extreme importance for epitaxial growth, are presented in section 2.4. In section 2.5, after giving the conditions used for the growth of the binary compounds of interest (HgTe, CdTe and ZnTe), the Interdiffused Multilayer Process[5] (IMP) as used in this work for the growth of the alloy $Hg_{1-x}Cd_xTe$ is described. This process is similar to those required for the growth of the superlattice systems, which are also described in this section. Finally, in section 2.6, conclusions as to the applicability of MOVPE to the growth of II-VI materials are drawn.

2.2 Principles of Metal-Organic Vapour Phase Epitaxy (MOVPE)

In essence, the growth of epitaxial layers of compound semiconductors by MOVPE involves the transport, in the vapour phase, of the constituent elements to the surface of a suitable substrate where growth takes place. At least one of the constituents is supplied in the form of a metal-organic compound and such compounds are pyrolysed at or near the substrate surface to release their component metal ions for growth. Metal-organic precursors are chosen which have sufficiently high vapour pressures at or slightly below room temperature to be picked up from bubblers by a carrier gas (usually hydrogen) and carried to the substrate at atmospheric pressure. Further, these compounds may be chosen such that pyrolysis, which determines the growth temperature, occurs at a temperature significantly below the melting point of the material being grown. Thus MOVPE is a low temperature, non-equilibrium vapour phase growth technique.

In this work, the metal-organic precursors used were di-methyl cadmium (DMC), di-methyl zinc (DMZ) and either di-ethyl tellurium (DET) or di-isopropyl tellurium (DIPT). Mercury was supplied from a heated mercury source inside the growth reactor as the vapour pressure of mercury, at temperatures significantly below that of the growth, is

sufficiently high to allow this. The chemistry of the decomposition of the metal-organic precursors to produce epitaxial growth is beyond the scope of this thesis.

2.3 The MOVPE Growth System

The MOVPE growth system was originally designed and constructed in this laboratory in order to grow HgTe, CdTe and $Hg_{1-x}Cd_xTe$. To this end the system consisted of a silica reactor tube containing an elemental mercury source, two metal-organic source lines used for di-methyl cadmium and diethyl tellurium, a hydrogen dilution line and a hydrogen bypass line. Subsequently two additional source lines were added for di-methyl zinc and tricarbonylmethylcyclopentadienyl manganese to enable the growth of ZnTe and MnTe although no MnTe was grown during the course of the work presented in this thesis and accordingly the manganese precursor is not considered further. At the same time another hydrogen dilution line was added. During the development of growth procedures for superlattice growth, the controlling computer was upgraded from a BBC microcomputer to an Acorn Archimedes. Here only the later version of the apparatus is described as this retains all the features of the original design. Schematic diagrams of the system are given in Figs. 2.1 to 2.3. The reactor is shown in Fig. 2.1. Fig. 2.2 shows the gas handling system and the control system is outlined in Fig. 2.3.

The Reactor

The reactor (Fig. 2.1) was specifically designed for the growth of mercury containing materials. Elemental mercury was placed in a silica boat situated at the front of the reactor. On entering the reactor the incoming gas stream, containing the metal-organic precursors, first passed over this boat picking up mercury vapour before passing over the graphite substrate holder where the substrates sat and growth took place. A reduction in the reactor's cross section above the substrate holder helped to laminarise the flow over the substrates. The substrate holder was resistively heated to a temperature sufficient to crack the precursors and produce epitaxial growth. A furnace comprising four 250 W quartz-halogen bulbs were used to heat the mercury boat through the reactor wall and so provide the required mercury vapour pressure. This method of heating ensured that the reactor walls in the vicinity of the boat and susceptor were always hotter than the mercury and so prevented the mercury from condensing prior to reaching the substrates. Downstream of the susceptor the reactor tube continued for some distance and incorporated a silica dump tube. This was not heated and allowed the mercury

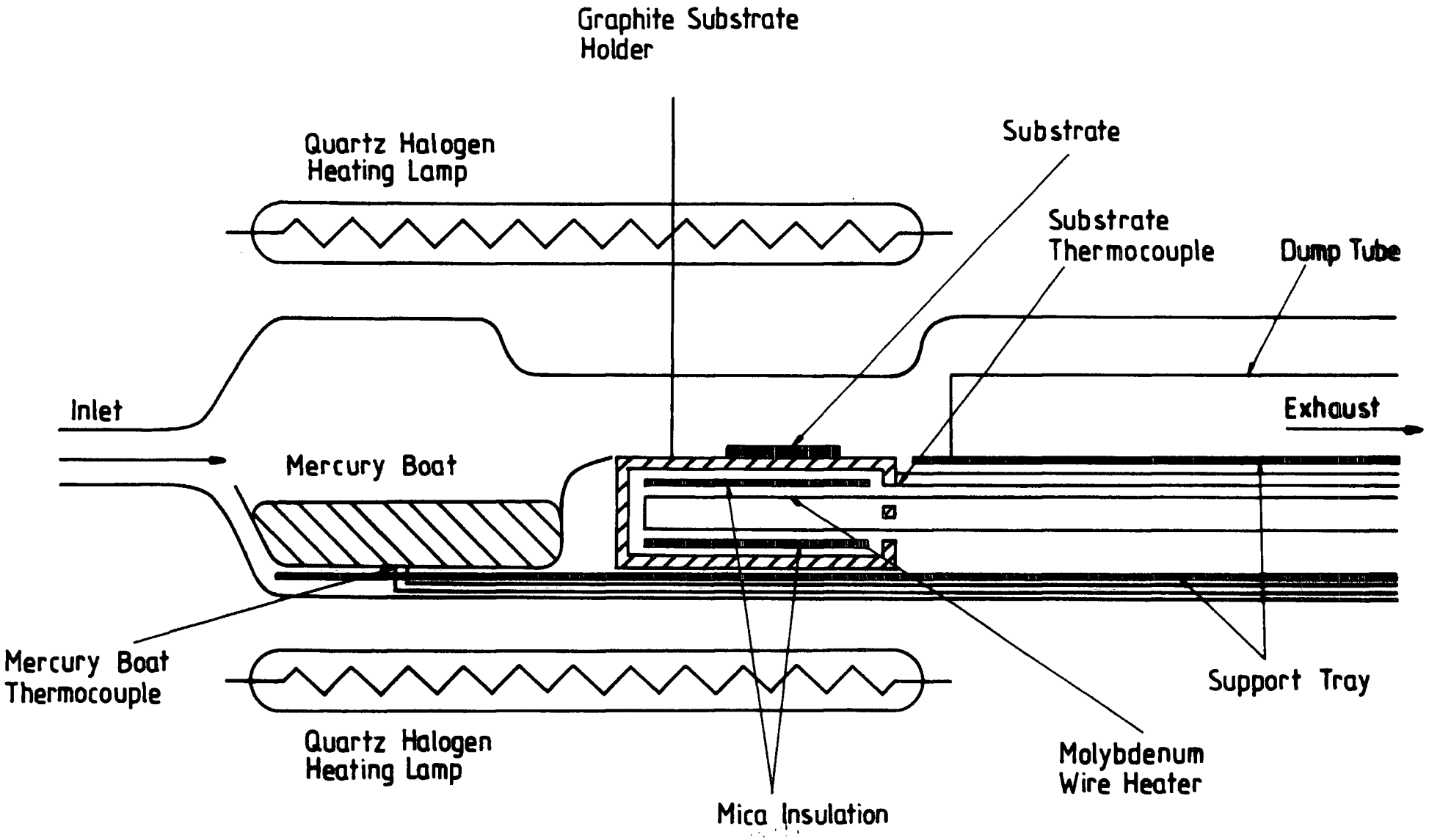

Fig. 2.1 MOVPE growth reactor.

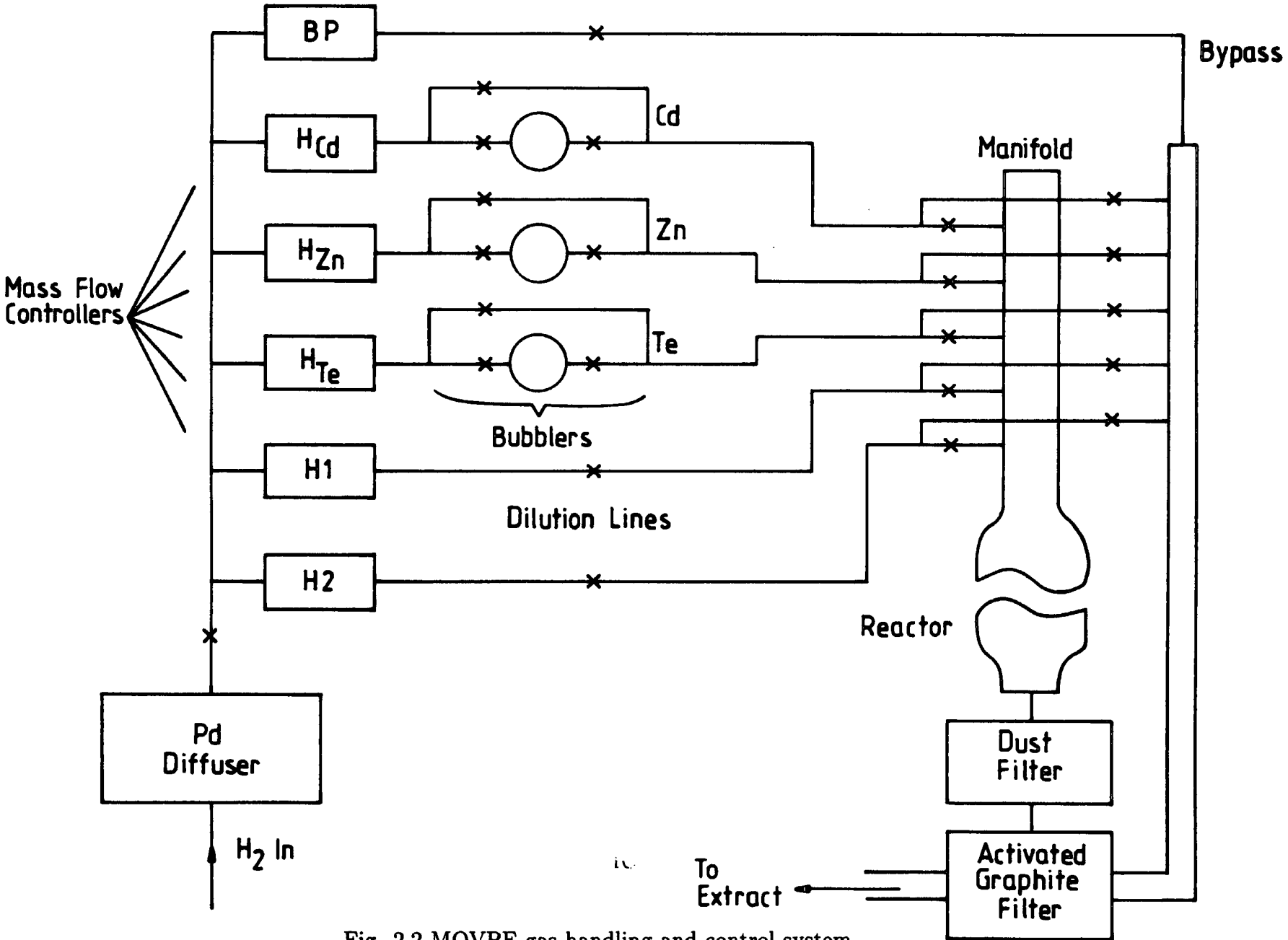

Fig. 2.2 MOVPE gas handling and control system.

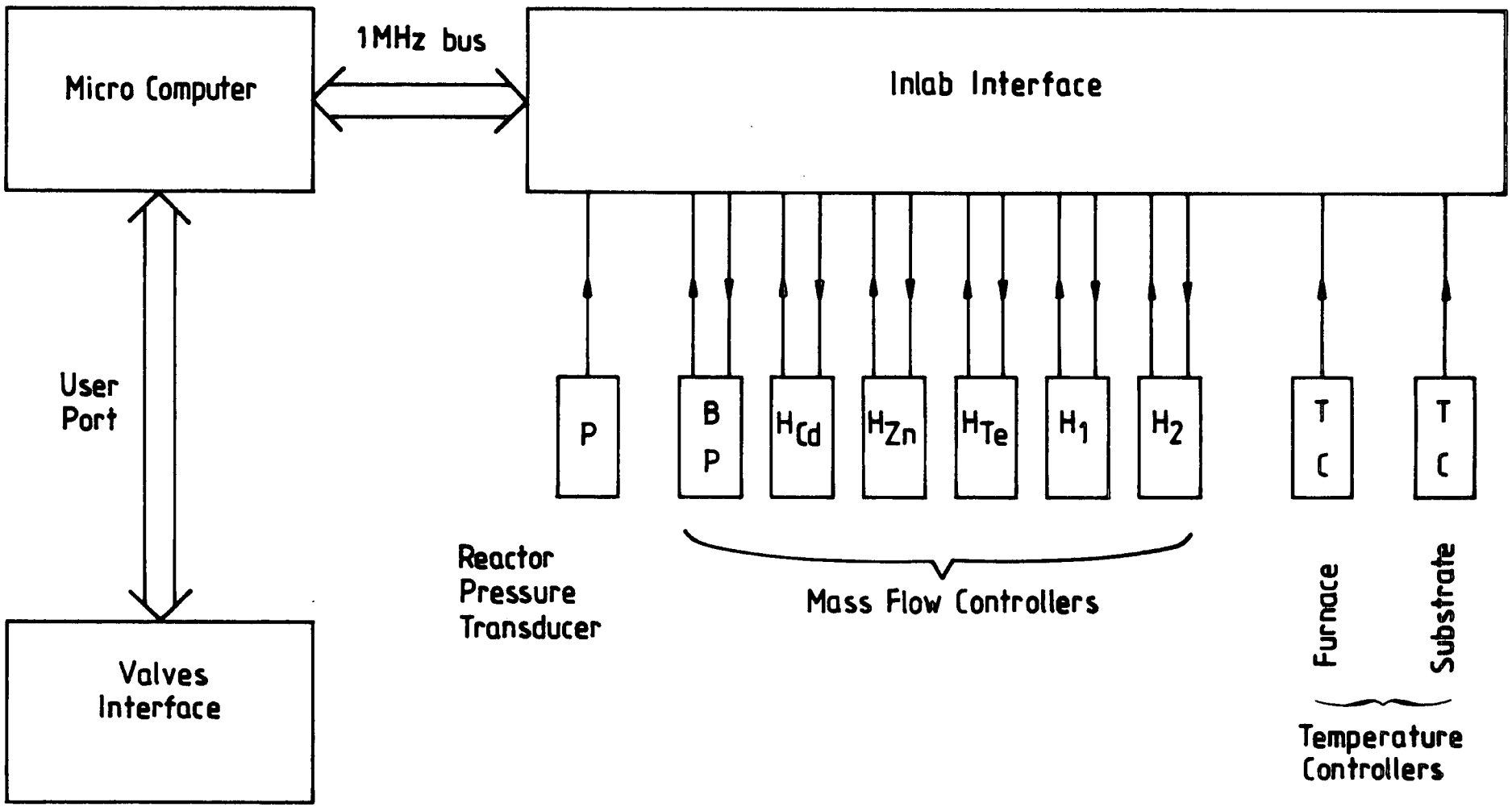

Fig. 2.3 MOVPE control system.

vapour and any reaction products which were involatile at the tube's temperature to condense out. Condensation was enhanced at the end of the reactor by a compressed air cooling collar (not shown). The incorporation of a dump tube made the reactor tube relatively long and accordingly it had a large volume which damped pressure surges caused by valve switching events.

Gas Handling

The system was of conventional vent-run design (Fig. 2.2) in which the metal-organic precursors were carried by a hydrogen carrier gas stream from their separate bubblers at an essentially fixed rate to a switching manifold at the reactor inlet. Here the flows could be switched either into the reactor or to bypass. This arrangement permitted multilayer growth while maintaining constant conditions in the bubblers and so ensured that the partial pressures of the metal-organic precursors in the reactor were reproducible from growth cycle to growth cycle. Large dead volumes were also effectively eliminated allowing fast switching from one set of precursors to another without the creation of ill-defined periods of precursor partial pressure. The hydrogen carrier gas was supplied via a palladium diffuser which provided hydrogen with a purity of better than 99.99995% . The flow rates passing through the bubblers were regulated by a series of mass flow controllers H_{Cd} to H_{Te}. It was also possible to supply hydrogen directly to the reactor via mass flow controllers H_1 and H_2 in order to provide a dilution flow during growth or for heat cleaning. A hydrogen flow was maintained in the bypass line (by mass flow controller BP) in order to ensure that all residual metal-organics were flushed out of the system. These hydrogen supplies were also operated in a vent-run configuration. The use of two dilution lines in this way allowed two dilution flows to be used in different parts of the growth cycle without delays in setting of the flows being introduced by the finite response time of the mass flow controllers. This ability to switch precisely defined flows with precisely defined precursor partial pressures quickly in or out of the reactor was essential for the growth of the superlattices as described in section 2.5.

The precursor bubblers sat in temperature controlled baths of large thermal mass in order to ensure that their temperature, and hence the vapour pressure of the metal-organics, remained constant throughout a growth run. These baths could be heated or cooled according to the precursor and the requirements of the growth process.

The metal-organic precursors used in this work and their reaction residues were highly toxic. In view of this, the outlet from the reactor was scrubbed before being

released into the atmosphere via a fume extract. This scrubbing took the form of a dust filter followed by an activated graphite filter. The dust filter removed any fine dust formed by reactions in the gas phase while activated graphite removed any unreacted metal-organics and uncondensed mercury by adsorption.

Provision was also made for evacuating the entire system via a liquid nitrogen cold trap using an oil diffusion pump backed by a rotary pump. This was useful for both leak testing and outgassing of the system. On warm up the cold trap could be flushed using nitrogen.

The Control System

The growth system was controlled (Fig. 2.3) by a microcomputer which was interfaced to the mass flow controllers, the temperature controllers and the pressure transducers by a series of digital to analogue and analogue to digital converters (3D Digital Design and Development Ltd. 'Inlab' interface) and to the valves via a digital switching interface. By latching the next required state of the valves and then transfering this data to the valve switching circuitry at a single command from the computer, the valve interface ensured that all valves switched simultaneously. It was also possible, using this unit, to control the valves manually which was useful for testing of the system. The computer controlled the valves and monitored temperatures, pressures, flows and the status of valves in the system displaying this information in real time in the form of a mimic diagram. Initially a BBC B microcomputer equiped with a 6502 second processor running a control program written in BASIC and 6502 assembly language was used to provide this control and monitoring. However, for the growth of superlattices, where it was necessary to have valve switching events at intervals as short as 4 seconds, it was found that this system was not fast enough to both monitor the growth and perform changes of valve state at exactly the required time. Due to the time taken to perform the various monitoring functions, the timing of valve switches could be delayed by up to 2 seconds resulting in unacceptable variations in the lengths of the shorter growth periods. This problem was solved by substituting an Acorn Archimedes microcomputer for the BBC B. The Archimedes ran a slightly modified version of the previously used BASIC program approximately 50 times faster and provided identical interfaces for the control electronics. A further advantage of this system was the increased memory capacity available for BASIC (650 Kbytes as opposed to 48 Kbytes) which allowed further program development.

2.4 Substrate Preparation

CdTe

{111} oriented wafers of CdTe were cut from CdTe boules the properties of which are described in chapter 5. Suitable grains were selected by observation and alignment was performed to $\pm 1°$ using the Laue back reflection X-ray technique. Initial alignment was often assisted by the presence of twin bands lying parallel to {111} planes which could be observed at the surface of the boule. As described in chapter one, it was necessary to distinguish between the {111}A and $\{\bar{1}\bar{1}\bar{1}\}$B planes of the sphalerite structure. In order to do this, a revealing etch consisting of a 1:1:1 mixture of HF:HNO_3:Acetic acid was used. This leaves the $\{\bar{1}\bar{1}\bar{1}\}$B (Te) growth face shiny and has been shown to be the most reliable polarity determining etch for CdTe[6] .

Polishing was carried out using a hydroplane polisher as shown in Fig. 2.4. This was similar to that developed by Gormley et al,[7] although the speed of rotation was slower at 75 rev min^{-1} instead of 1200 rev min^{-1}. The wafers being polished hydroplane on a thin layer of the polishing solution without contacting the polishing pad which serves only to hold the polishing solution. This method eliminates mechanical damage and introduces fresh polishing solution to the wafers very rapidly. Wafers were mounted on a PTFE stub using wax. The stub was constrained horizontally by the spinner but was free to find its own level in the vertical direction according to the flow of polishing solution. As the turntable rotated, the spinner, and hence the stub, rotated in the opposite direction thus preventing ridging of the wafer being polished. The polishing solution used was 1% bromine in a 4:1 methanol:ethanediol mixture. It was necessary to remove several hundered micrometers of CdTe during polishing in order to ensure that all residual mechanical damage from the cutting process was completely removed[8]

.

After removal from the stub, the CdTe wafers were degreased in 1,1,1-trichloroethane vapour. Following this, and immediately prior to loading into the MOVPE reactor, the CdTe substrates were given a brief (~5 sec) dip in a 2% solution of bromine in methanol followed by rinsing in 'Aristar' grade methanol. This etchant has been shown by X-ray photoelectron spectroscopy (XPS) to leave CdTe surfaces which are almost stoichiometric[9] The CdTe surfaces produced by this process were completely single crystal as attested to by the use of Reflection High Energy Electron Diffraction (RHEED) (see chapter three).

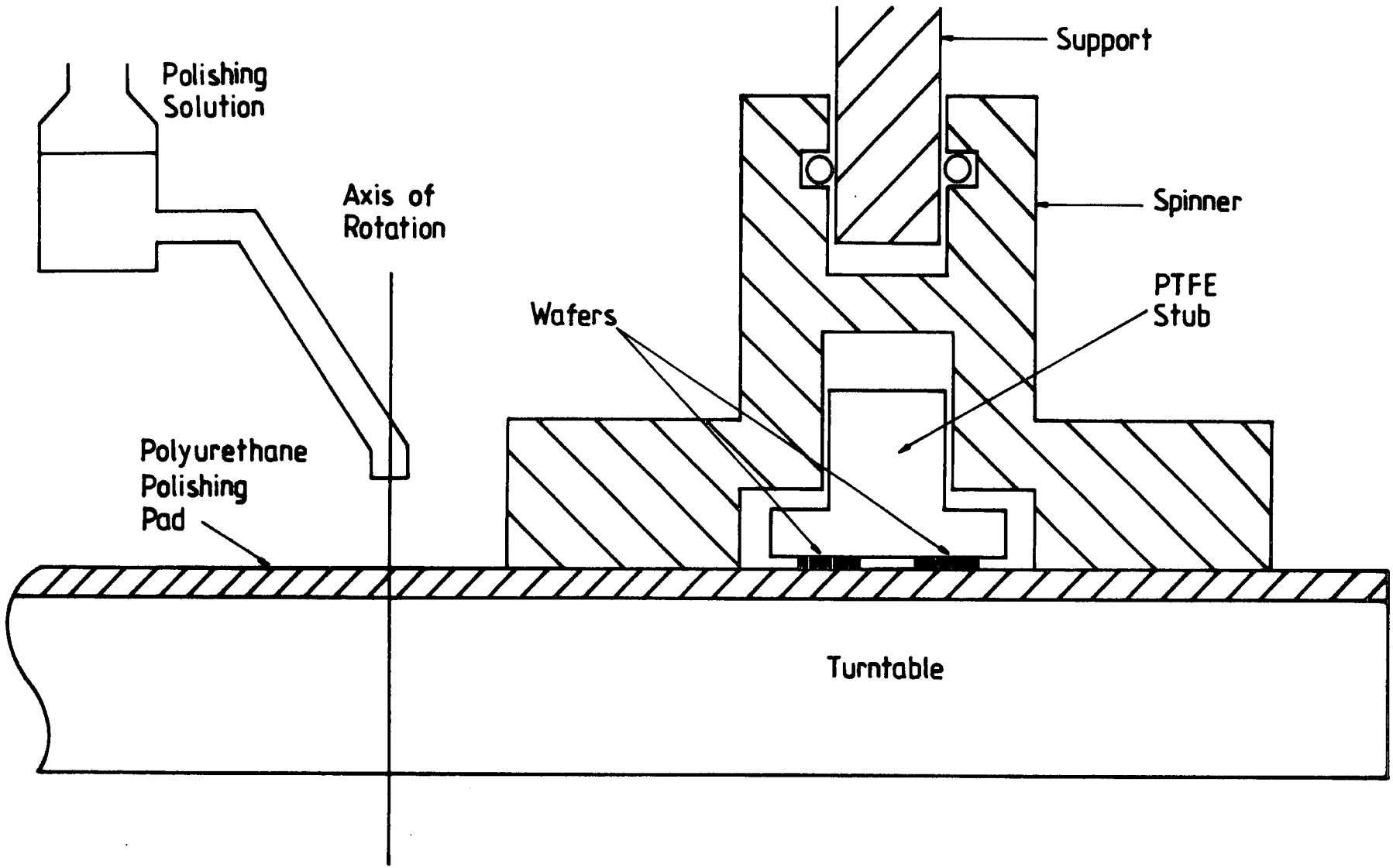

Fig. 2.4 Hydroplane polisher.

$\{\bar{1}\bar{1}\bar{1}\}$B orientated CdTe substrates were used for all of the $Hg_{1-x}Cd_xTe$ layers considered during the course of this work and were also used for some of the early HgTe:ZnTe and CdTe:ZnTe superlattices.

GaAs

Mechanically polished {100} and $\{\bar{1}\bar{1}\bar{1}\}$B oriented GaAs wafers were supplied by ICI Wafer Technology Ltd. and MCP Electronic Materials Ltd. respectively. Preparation of these substrates was performed immediately prior to growth and followed the widely adopted procedure of degreasing in 1,1,1-trichloroethane vapour, etching in a 4:1:1 solution of H_2SO_4:H_2O_2:H_2O and then rinsing in flowing 18MΩcm de-ionised water. The H_2SO_4:H_2O_2:H_2O etch was performed at 40°C for 4 minutes and had the effect of etching the GaAs by an oxidation process thereby removing damage left by the mechanical polishing and leaving the GaAs surface protected by a thin oxide layer. All stages of this preparation were carried out with the substrates held in specially constructed silica jigs which ensured that no mechanical damage was introduced by handling. During the H_2SO_4:H_2O_2:H_2O etch it was extremely important to ensure that the substrates were maintained with the intended growth surface uppermost to allow any O_2 bubbles which formed on the GaAs to escape. Failure to do this resulted in ridging of the GaAs caused by a reduction in the quantity of material removed from areas masked by the bubbles.

Both {100} and $\{\bar{1}\bar{1}\bar{1}\}$B oriented GaAs substrates were used for the growth of ZnTe layers and HgTe:ZnTe and CdTe:ZnTe superlattices.

GaSb

RHEED studies showed that the surfaces of GaSb wafers supplied, mechanically polished, by MCP Electronic Materials Ltd. were polycrystalline and therefore unsuitable for epitaxial growth. The H_2SO_4:H_2O_2:H_2O etch is not suitable for the preparation of GaSb as it causes severe damage to the GaSb surface. Accordingly, mechanical damage was removed from these substrates using the hydroplaning technique described above. This was followed by degreasing in 1,1,1-trichloroethane and rinsing in 18MΩcm deionised water. As in the case of CdTe substrates this treatment was found to yield GaSb surfaces which gave excellent single crystal RHEED patterns. XPS studies[10] have shown that bromine/methanol etching leaves only a thin layer of gallium and antimony oxides on GaSb surfaces.

{100} oriented GaSb substrates were used for the growth of some of the ZnTe layers

investigated during the course of this work.

Heat Cleaning of Substrates

After preparation, as described above, the substrates were loaded into the MOVPE reactor which was then flushed with hydrogen for at least 1 hour to ensure the removal of any oxygen from the system. The substrates were then heat cleaned in flowing hydrogen for 10 minutes with the intention of reducing any native oxide present at the surface which might have interfered with epitaxial growth. In the case of CdTe substrates this was carried out at 410°C [11] while for GaAs and GaSb a temperature of ~550°C was used. For GaAs, this treatment has been found by X-ray photoelectron spectroscopy to be effective in removing both the native oxide and carbonaceous deposits from the surface[12] . After the heat clean, the susceptor temperature was reduced to the growth temperature and the growth began as described in the following sections.

2.5 Growth of Binary Compounds

The three binary compounds of interest in this work, (HgTe, CdTe and ZnTe) were grown using elemental mercury, di-methyl cadmium and di-methyl zinc as the group II precursors together with either di-ethyl tellurium or di-isopropyl tellurium as the group VI precursor. DET was used for the growth of $Hg_{1-x}Cd_xTe$ and the early superlattices and constrained the growth temperature to a minimum of ~ 395°C . The substitution of DIPT for DET as the tellurium precursor allowed growth at temperatures as low as 300°C .

Table 2.1 gives the conditions of total flow and precursor partial pressure typically used for the growth of the three binary compounds. The growth of HgTe requires low flow conditions together with high vapour pressures of mercury and tellurium. For the growth of HgTe in the IMP process for $Hg_{1-x}Cd_xTe$, the mercury boat was maintained at 205°C , giving a mercury vapour pressure of 20 Torr[13] , while in the case of HgTe:ZnTe superlattice growth, the boat temperature was reduced to 185°C , which corresponds to a mercury vapour pressure of 10 Torr, in order to prevent prereaction of the zinc and tellurium alkyls over the boat. Both CdTe and ZnTe were grown under similar high flow conditions with the partial pressures of the cadmium, zinc and tellurium precursors being approximately equal.

	total flow (sccm)	P_{Hg} (Torr)	P_{Cd} (Torr)	P_{Zn} (Torr)	P_{Te} (Torr)
HgTe	1500	20	-	-	3.0
CdTe	5500	-	1.5	-	1.5
ZnTe	5000	-	-	0.5	0.8

(a)

	total flow (sccm)	P_{Hg} (Torr)	P_{Cd} (Torr)	P_{Zn} (Torr)	P_{Te} (Torr)
HgTe	1000	10	-	-	3.4
CdTe	5500	-	0.5	-	0.4
ZnTe	5000	-	-	0.4	0.4

(b)

Table 2.1 Typical conditions used for the growth of binary compounds (a) using di-ethyl tellurium and (b) using di-isopropyl tellurium.

2.6 Growth of $Hg_{1-x}Cd_xTe$ by the Interdiffused Multilayer Process

As described in the previous section, the conditions used for the growth of HgTe and CdTe individually are considerably different. For $Hg_{1-x}Cd_xTe$ the lowest growth temperature attainable is determined by the requirement for efficient pyrolysis of the DET in the growth of HgTe and is lowest for low total flow rates. The growth temperature sets the minimum temperature for the mercury boat, and hence the reactor wall, as the mercury vapour pressure must be above the tellurium rich solidus for the required x value. Conversely, growth of CdTe may take place at lower temperatures than HgTe due to the formation of a DMC:DET adduct. In order to prevent pre-reaction over the boat and at the reactor walls, a low boat temperature and high flow rates are required. It is therefore impossible to grow the alloy $Hg_{1-x}Cd_xTe$ directly under conditions which are optimum for both HgTe and CdTe. Early attempts to do this were beset by problems of poor uniformity due to these effects. This lead to the development of the Interdiffused Multilayer Process[5] . In this process, alternating, thin ($\sim$ 1000 Å) layers of HgTe and CdTe are grown, each under optimised conditions, and then these are interdiffused to produce the alloy. This process is possible due to the close lattice match and extremely high interdiffusion coefficient ($\sim 5 \times 10^{-13}$ cm^2s^{-1} at 410°C for $x = 0.2$[14]) between HgTe and CdTe.

A timing diagram illustrating one cycle of events during the IMP growth of $Hg_{1-x}Cd_xTe$ is given in Fig. 2.5. Each cycle comprises two phases. In the first, a high flow is maintained and CdTe is grown, and in the second, a low flow regime is established and HgTe is grown. Although both the tellurium precursor and mercury vapour are present during the CdTe phase, the presence of di-methyl cadmium switches the HgTe reaction off and no HgTe is grown. This suppression of the HgTe reaction is so effective that if the di-methyl cadmium was not switched off under these conditions, then an epitaxial layer consisting only of CdTe would be grown.

At the end of the deposition, the susceptor and furnace were maintained at the growth temperatures for 10 minutes to ensure complete interdiffusion of the final IMP layers which typically have a period of 2000 Å. At the end of this period, the furnace and susceptor heating was switched off and the reactor was allowed to cool under flowing hydrogen.

Growth of ZnTe Capped $Hg_{1-x}Cd_xTe$

Some $Hg_{1-x}Cd_xTe$ layers were capped with ZnTe in order to investigate the use of ZnTe as a passivation/insulator layer. For these samples, after the growth of the $Hg_{1-x}Cd_xTe$ layer and subsequent annealing, the furnace heating was switched off while the susceptor temperature was ramped up to 410°C for the ZnTe growth which was then initiated. Ramping of the susceptor took approximately 6 minutes during which time, the mercury boat temperature fell to 90°C . The ZnTe growth time was 200 seconds which was expected to give a ZnTe cap thickness of $\sim$ 1000 Å. After the growth of the capping layer, the reactor was allowed to cool normally.

2.7 Growth of HgTe:ZnTe Superlattices

The first attempts to grow this superlattice made use of the conditions which had been established for the growth of the two binary constituents; i.e. substrate temperatures of 395 - 410°C, a Hg source temperature of 205°C and high flow rates during the ZnTe growth phase and low flow rates during the HgTe growth. For equal growth times, the resulting superlattice should have been Hg rich, due to the higher HgTe growth rate. However, under these conditions no HgTe grew at all. On closer inspection it was found that a skin had formed on the surface of the Hg in the boat although there had been some evaporation, as attested by weight loss from the boat and the condensation of Hg downstream of the substrate. When the growth run was repeated under identical conditions of flow and temperature but without the DMZ switched in to the reactor, HgTe was found to grow satisfactorily, although at a significantly reduced rate. From this and other similar experiments it was concluded that :

(i) The skin which had formed on the surface of the Hg was probably the result of pre-reaction. It thus appeared that in growing ZnTe under the heated wall conditions necessary for HgTe growth, gas phase reactions were more severe. This problem was largely overcome by increasing the hydrogen dilution flow through the reactor and reducing the mercury boat temperature.

(ii) The presence of even residual amounts of DMZ in the reactor had suppressed the reaction of Hg with DET, suggesting that flushing between the ZnTe and HgTe cycles was inadequate. A minimum flushing period of about 20 seconds appeared to be necessary.

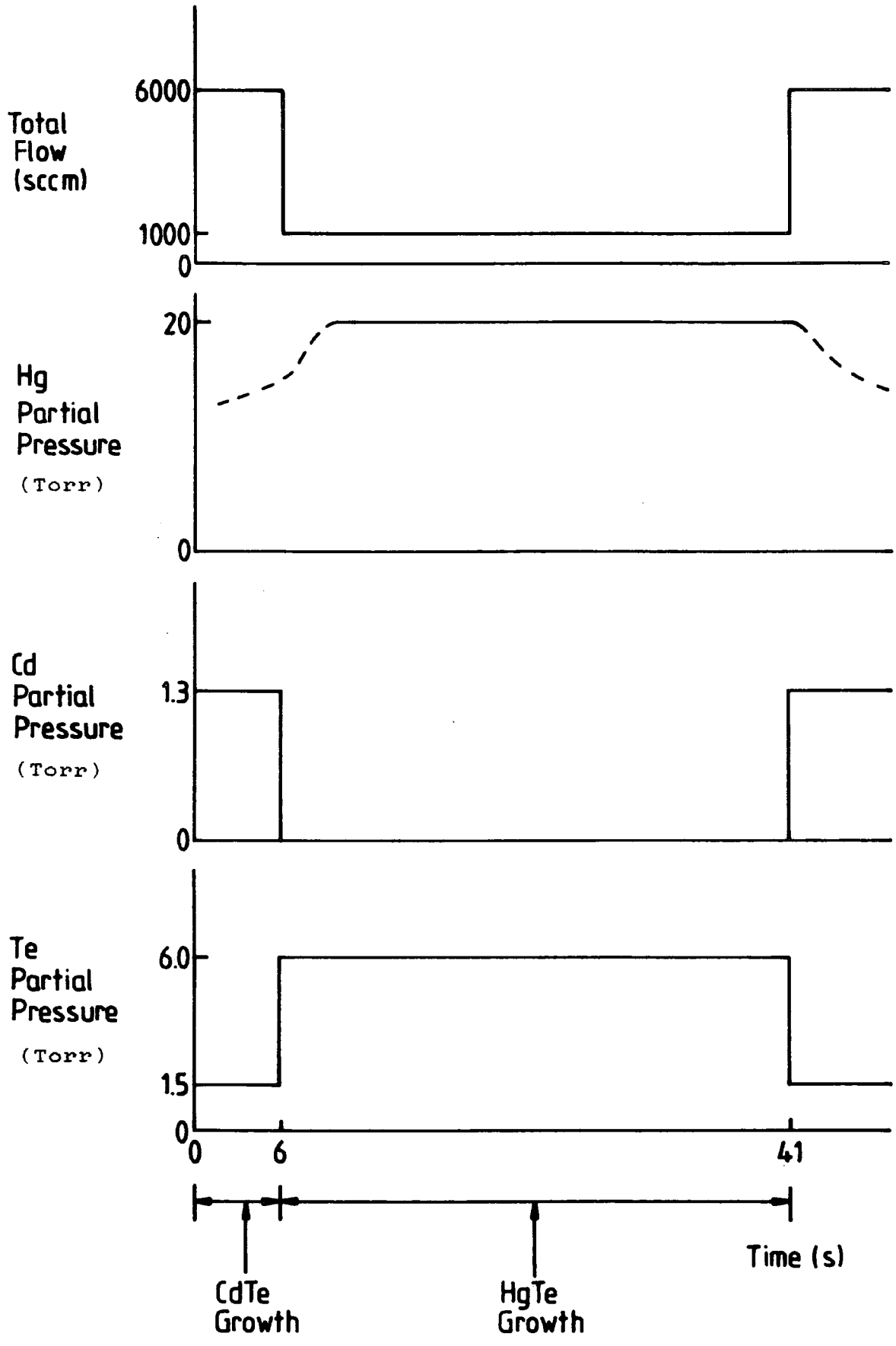

Fig. 2.5 Growth cycle for $Hg_{1-x}Cd_xTe$.

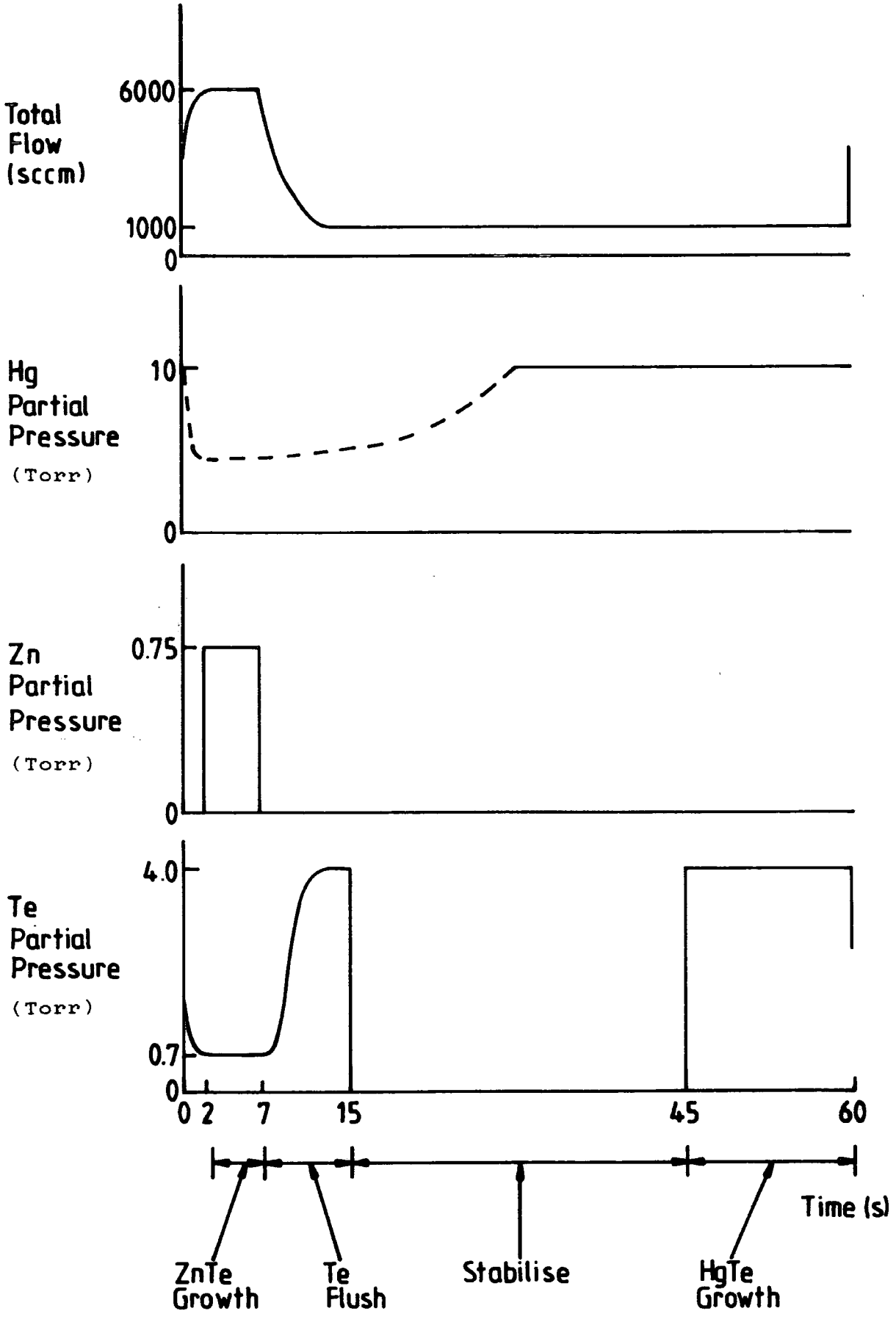

Fig. 2.6 Growth cycle for HgTe:ZnTe superlattices.

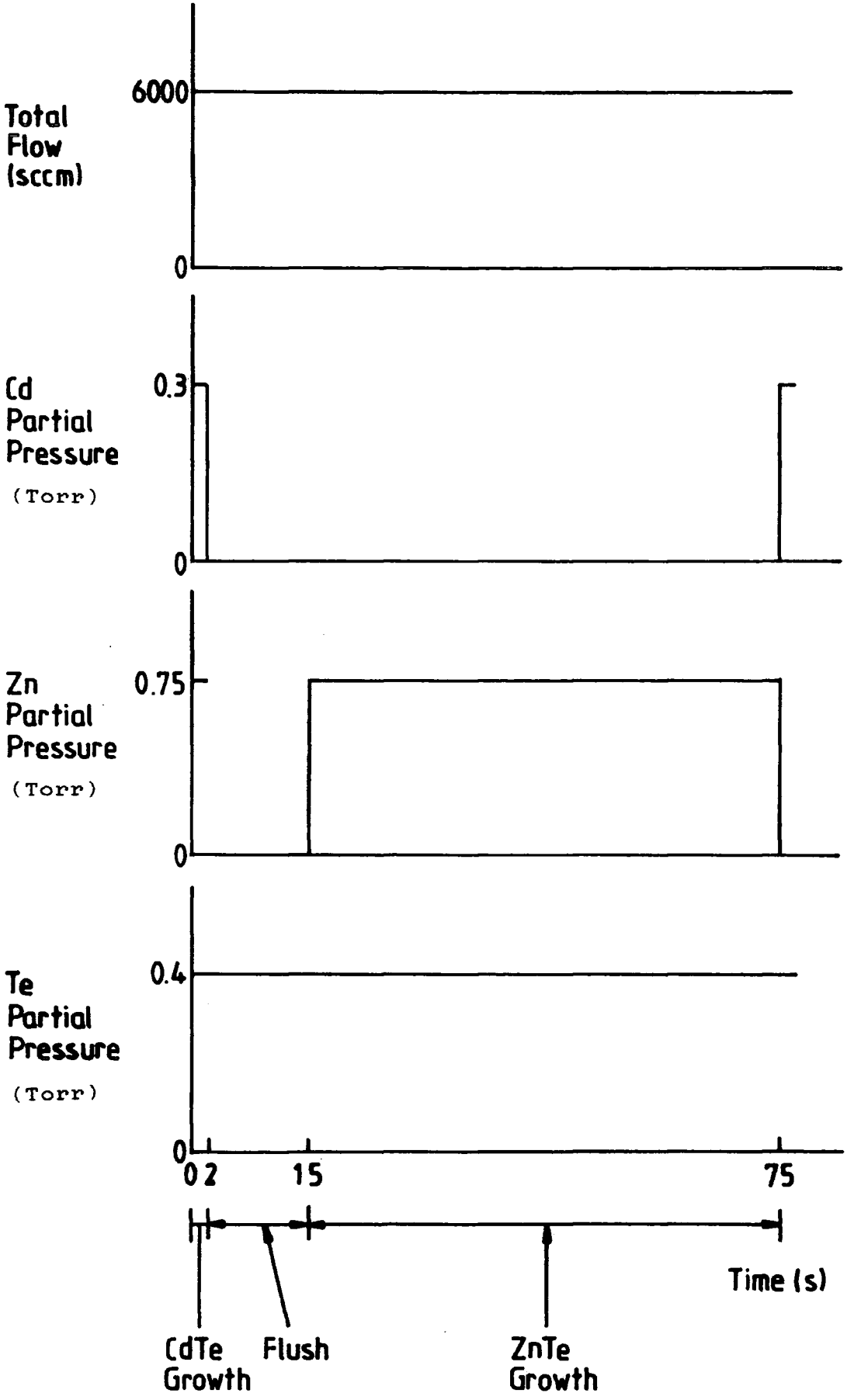

Fig. 2.7 Growth cycle for CdTe:ZnTe superlattices.

(iii) The high flow rate used during the ZnTe part of the cycle was effectively preventing the Hg vapour pressure from reaching saturation, and insufficient time had been allowed for the low flow rate to become re-established and for the Hg vapour pressure to be restored.

A timing diagram representing the process that was eventually adopted as a result of these trials is shown in Fig. 2.6. This shows the variation in the partial pressures of DET, DMZ and DET or DIPT together with the total flow over one complete cycle of the growth. At the completion of the ZnTe phase, the DMZ was switched out while the dilution flow was ramped down to give a total flow of 1000 sccm. Thus the remaining DMZ was either flushed out or reacted with the DET or DIPT which was still flowing through the reactor. After about 8 seconds the tellurium precursor was also switched out. After a further period of 30 seconds to allow the Hg vapour pressure to become re-established, the tellurium was admitted into the reactor again to commence the HgTe growth phase. On completion of the HgTe part of the cycle, the dilution flow was increased again to give a total flow of 6000 sccm, effectively terminating HgTe growth, and after a further 2 seconds the DMZ was switched back into the reactor and the growth cycle repeated. This procedure resulted in controllable growth of HgTe-ZnTe superlattices, although the rather long growth cycle increased intermixing in superlattices grown at 395°C.

One further point to emerge from these studies was that growth rates measured for relatively thick layers ($> 0.5\mu$m) were significantly different from those calculated from measured layer thicknesses and nominal growth times in superlattices. In the case of ZnTe, growth rates appeared to be considerably greater for the superlattices than for thick layers (60 $\text{Å}s^{-1}$ compared with 5 $\text{Å}s^{-1}$). Conversely, in the case of HgTe, the growth rate was very much lower for thin layers in the superlattice than for thick ones (5 $\text{Å}s^{-1}$ instead of 50 $\text{Å}s^{-1}$). In view of the difficulties encountered in growing HgTe described above, it seems likely that the actual ZnTe growth times were longer than intended, while the HgTe growth times were reduced by the presence of residual DMZ in the reactor. The graphite substrate holder may have contributed to the latter effect by adsorbing and subsequently desorbing DMZ during the ZnTe and HgTe growth phases respectively.

2.8 Growth of CdTe:ZnTe Superlattices

It was possible to use a much simpler process for the growth of CdTe:ZnTe superlattices than for the HgTe:ZnTe superlattices refered to above because the conditions required for the growth of the constituent binaries were more closely matched. The timing diagram for one growth cycle is shown in Fig. 2.7. A high flow condition was maintained throughout the cycle with the tellurium precursor flowing continuously. The DMC and DMZ were switched in as shown. Although the conditions for the growth of the two constituent binaries were similar it was found that, for CdTe:ZnTe thickness ratios in the region of 1:1, the ZnTe growth time needed to be $\sim$ 30 times longer than the CdTe growth time. In addition, it was found that a flushing period was required prior to the ZnTe growth in order to give reproducible ZnTe thicknesses. It is likely that the presence of residual DMC in the reactor can suppress the ZnTe reaction and that this effect is very significant for the growth of very thin ZnTe layers as required for a superlattice.

2.9 Summary and Conclusions

The MOVPE growth system, the preparation of substrates for epitaxial growth, the growth of the binary compounds HgTe, CdTe and ZnTe together with the IMP growth of $Hg_{1-x}Cd_xTe$ and the growth of HgTe:ZnTe and CdTe:ZnTe superlattices have been described. A feature of $Hg_{1-x}Cd_xTe$ and the superlattice systems is the dominance of the growth reaction for one of the binary constituents. In the case of $Hg_{1-x}Cd_xTe$ and CdTe:ZnTe superlattices the CdTe reaction dominates while the ZnTe reaction tends to suppress HgTe growth in the HgTe:ZnTe system. The IMP process for the growth of $Hg_{1-x}Cd_xTe$ was developed to overcome problems of non-uniformity in the direct growth of the alloy caused by such effects and one group[15] have investigated the use of a rotating substrate holder for the growth of the (Cd,Zn)Te alloy for the same reason. In this work it has been found that in order to obtain good control over the extremely thin individual binary layers in superlattices, flushing is necessary between the different phases of the growth cycle. Accepting this requirement, it may be that superlattices are preferable to the equivalent alloys simply because they are easier to grow by MOVPE.

REFERENCES

1. M.A. Herman and M. Pessa, J. Appl. Phys. **57** (1985) 2671.
2. G. Destefanis, Proc. NATO Advanced Research Workshop on The Future of Small Bandgap Semiconductors, Liege 5th to 9th September 1988. to be published.
3. A.Y. Cho and J.R. Arthur, Progress in Solid State Chemistry **10** (1975) 157.
4. K.A. Harris, S. Hwang, D.K. Blanks, J.W. Cook, Jr., J.F. Schetzina, N. Otsuka, J.P. Baukus and A.T. Hunter, Appl. Phys. Letters **48** (1986) 396.
5. J. Tunnicliffe, S.J.C. Irvine, O.D. Dosser and J.B. Mullin, J. Crystal Growth **68** (1984) 245.
6. P.D. Brown, K. Durose, G.J. Russell and J. Woods. J. Crystal Growth to be published.
7. J.V. Gormley,
8. M. Lunn, to be published
9. M.H. Patterson and R.H. Williams, J. Phys. D: Appl. Phys. **11** (1978) L83.
10. T.D. McLean, T.M. Kerr, D.I. Westwood, J.D. Grange and I.J. Murgatroyd, Inst. Phys. Conf. Ser. **74** chapter 3.
11. J.E. Hails, G.J. Russell, P.D. Brown, A.W. Brinkman and J. Woods, J. Crystal Growth **86** (1988) 516.
12. R.W. Bernstein and J.K. Grepstad, J. Vac. Sci. Technol. **A7** (1989) 581.
13. CRC Handbook of Chemistry and Physics 59th Edition (1978) Ed. R.C. Weast
14. J.B. Mullin, J. Giess, S.J.C. Irvine, J.S. Gough and A. Royle, Mat. Res. Soc. Symp. Proc. **90** (1987) 367.
15. W.L. Ahlgren, S.M. Johnson, W.J. Hamilton, A. Szilagyi, G.S. Tompa, P.D. Reinert, C.K. Ziegler and W.J. Lick, Mat. Res. Soc. Symp. Proc. (1990) to be published.

3. Experimental Techniques for the Assessment of Epitaxial Layers

3.1 Introduction

In this chapter, the experimental techniques used to characterise epitaxial layers are described. The technique due to van der Pauw[1] for measuring the resistivity and Hall coefficient of thin films independently of their geometry is described in section 3.2, prior to a description of the apparatus used to perform these measurements as a function of temperature. As the main aim of the work reported in this thesis was to investigate narrow-gap semiconductor materials, it was of considerable importance to perform infra-red transmission measurements in order to characterise the optical absorption in these materials. The essential details of this technique are given in section 3.3. Both scanning electron and transmission electron microscopy were used during the course of this work as part of the structural characterisation of epitaxial layers and superlattices. The use of these two techniques is outlined in section 3.4. For crystalline materials the periodicity of the crystal lattice means that, under suitable conditions, the interaction of radiation with the material can produce a diffraction pattern. A diffraction pattern is essentially a Fourier transform of the real lattice, and as such, is a complete description of it. Two complimentary diffraction techniques used during the course of this work were Reflection High Energy Electron Diffraction (RHEED) and Double Crystal X-ray diffraction (DCXRD), both of which are described in section 3.5.

3.2 Measurement of Resistivity and the Hall Coefficient

Van der Pauw[1] has shown that the resistivity and Hall coefficient of a thin layer of known thickness but arbitary shape may be measured by means of four ohmic contacts, arbitrarily labelled A,B,C,D, of negligible size positioned anywhere on the periphery of the sample (Fig.3.1). For the resistivity measurement, four resistances $R_{AB,CD}$, $R_{BC,DA}$, $R_{CD,AB}$ and $R_{DA,BC}$ are defined, where the first and second pair of subscripts refer to current and voltage terminals respectively. The resistivity, ρ, of the sample is given by any adjacent pair of resistances (Table 3.1) according to the following formula given here for $R_{AB,CD}$ and $R_{BC,DA}$:

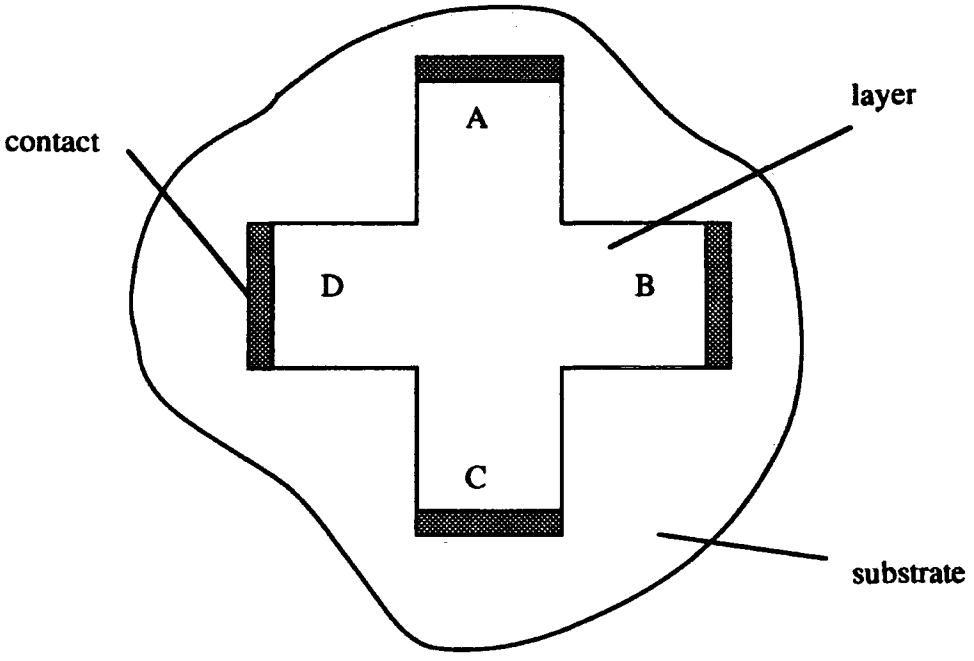

Fig. 3.1 Sample Geometry for van der Pauw Measurements

Resistance	Current Terminals	Voltage Terminals	Pairings for Resistivity
$R_{AB,CD}$	A B	C D	
$R_{BC,DA}$	B C	D A	
$R_{CD,AB}$	C D	A B	
$R_{DA,BC}$	D A	B C	
$R_{DB,AC}$	D B	A C	Hall
$R_{AC,BD}$	A C	B D	Configurations

Table 3.1 Definition of the six van der Pauw resistances

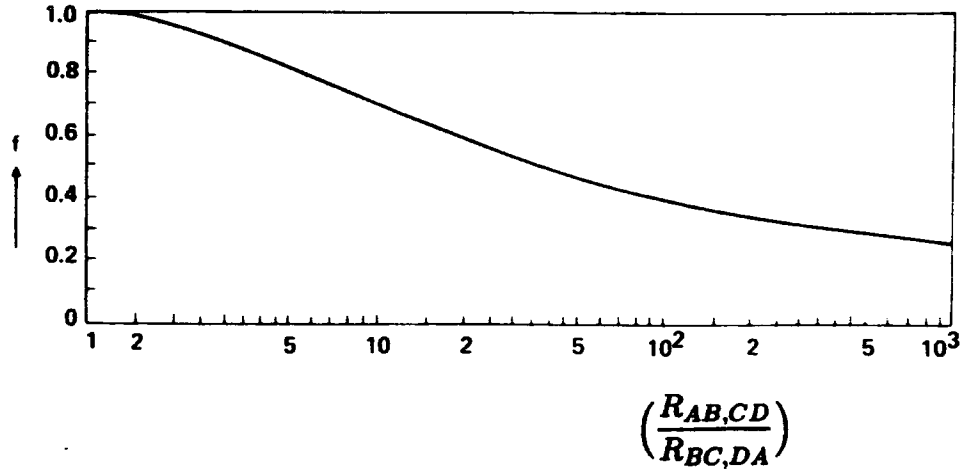

Fig.3.2 The function f plotted as a function of $\frac{R_{AB,CD}}{R_{BC,DA}}$.

$$\rho = \frac{\pi d}{ln2}.\frac{(R_{AB,CD} + R_{BC,DA})}{2}.f\left(\frac{R_{AB,CD}}{R_{BC,DA}}\right) \tag{3.1}$$

where d is the layer thickness and the function f satisfies the relation:

$$\frac{R_{AB,CD} - R_{BC,DA}}{R_{AB,CD} + R_{BC,DA}} = \frac{f}{ln2}.arcosh\left(\frac{exp(\frac{ln2}{f})}{2}\right) \tag{3.2}$$

The function f is solely a function of the ratio of two adjacent resistances and is close to 1 if the resistances are similar as shown in Fig.3.2

The Hall coefficient R_H may be determined from the change in resistances $R_{AC,BD}$ or $R_{DB,AC}$ with a change in the magnetic field perpendicular to the plane of the sample ΔB using the following equation :

$$R_H = \frac{d}{\Delta B}.\Delta R_{AC,BD} \tag{3.3}$$

Samples used in this work typically had linear dimensions of 5-10 mm and contacts were relatively large. Accordingly, to reduce the effect of the finite contact size, layers were etched into the form of a cross (Fig3.1) using a solution of 2% bromine in methanol with 'Lacomit' varnish as a mask. For the typical sample and contact geometry illustrated in Fig.3.1, the geometrical error in the calculated resistivity due to the contacts is 0.1%[2] . In this work, such errors have been ignored. This etching procedure also eliminated any conducting path over the back of the sample. Suitable etch times were estimated on the basis of work done on test pieces of known thickness where the minimum time for complete clearence to the substrate was determined by a series of short etches and EDX observations. Typically, etch times in the region of 5 minutes were found to be satisfactory.

Electrical contacts to the samples were made by fusing indium onto the surface of the layers using a small low temperature soldering iron. Good electrical measurements were only obtained from $Hg_{1-x}Cd_xTe$ samples where etching of the layer to produce a van der Pauw cross, contacting and measurement had been performed immediately after growth and where care had been taken to avoid any contamination.

Low Field Hall Apparatus

In order to provide for routine determination of the low field Hall coefficient and resistivity of epitaxial layers at temperatures from close to that of liquid nitrogen up to ~100 °C , a suitable apparatus was designed and constructed. This implemented the procedure outlined in Fig.3.3 to measure the van der Pauw resistances defined in the previous section. Essentially the method entails making current-voltage measurements on the sample in each of the required configurations. The gradient of a least squares fit to the data gives the van der Pauw resistance for that configuration. This method of determining the resistances eliminated the effect of offset potentials in the system and provided some averaging. The current scans were performed in both forward and reverse directions to provide further averaging. The elimination of offset potentials and averaging was especially important in the case of the Hall coefficient measurements due to the small resistance change being measured. A further advantage of this technique is that it was possible to plot the raw current-voltage data to ensure that the contacts to the sample were ohmic.

An outline of the apparatus is shown in Fig.3.4 It is based around a cold finger cryostat in which the sample is mounted so as to lie at the centre of the pole pieces of the electromagnet. Both the cryostat and the magnet were fabricated in this department. The programmable current source and relay unit were both designed and constructed for this project and together with the digital voltmeter (DVM) provide the means of performing current-voltage scans in any of the six possible configurations. The DVM is also used to measure the voltage across a copper/constantan thermocouple which is used to monitor the temperature of the copper block close to the sample. A constant current source is used to drive the magnet which is switched on or off and between forward and reverse fields by a dedicated switching circuit. Initially, an Acorn Master microcomputer was used to control the system and analyse the resulting data. Later this was replaced by an Acorn Archimedes microcomputer which ran virtually identical software. The chamber in which the coldfinger lies is evacuated to $< 10^{-4}$ Torr by an oil diffusion pump backed by a rotary pump to provide thermal insulation and to prevent the condensation of water vapour onto the sample.

Fig.3.5 shows the measurement cicuit in detail. Three double pole double throw relays interchange the sample current and voltage terminals to give the six van der Pauw configurations. Another two such relays allow for the connection of the DVM

```
FOR  each temperature
     measure temperature
     FOR  each required VDP resistivity configuration
          FOR  each current direction

               scan current
               measure voltage

          NEXT
     NEXT
     FOR  each magnetic field direction
          FOR  each required VDP Hall Configuration
               FOR  each current direction

                    scan current
                    measure voltage

               NEXT
          NEXT
     NEXT
     measure temperature
     store data
NEXT
```

Fig. 3.3(a) Van der Pauw Measurement Procedure

```
FOR  each temperature
     FOR  each VDP resistivity configuration
          FOR  each current direction

               least squares fit to give resistance

          NEXT
          configuration resistance := average
     NEXT
     FOR  each adjacent pair of resistances

          calculate sample resistivity

     NEXT
     FOR  each VDP Hall configuration
          FOR  each current direction
               FOR  each field direction

                    least squares fit to give resistance

               NEXT
               calculate Hall coefficient
          NEXT
     NEXT
NEXT
```

Fig.3.3(b) Van der Pauw Analysis Procedure

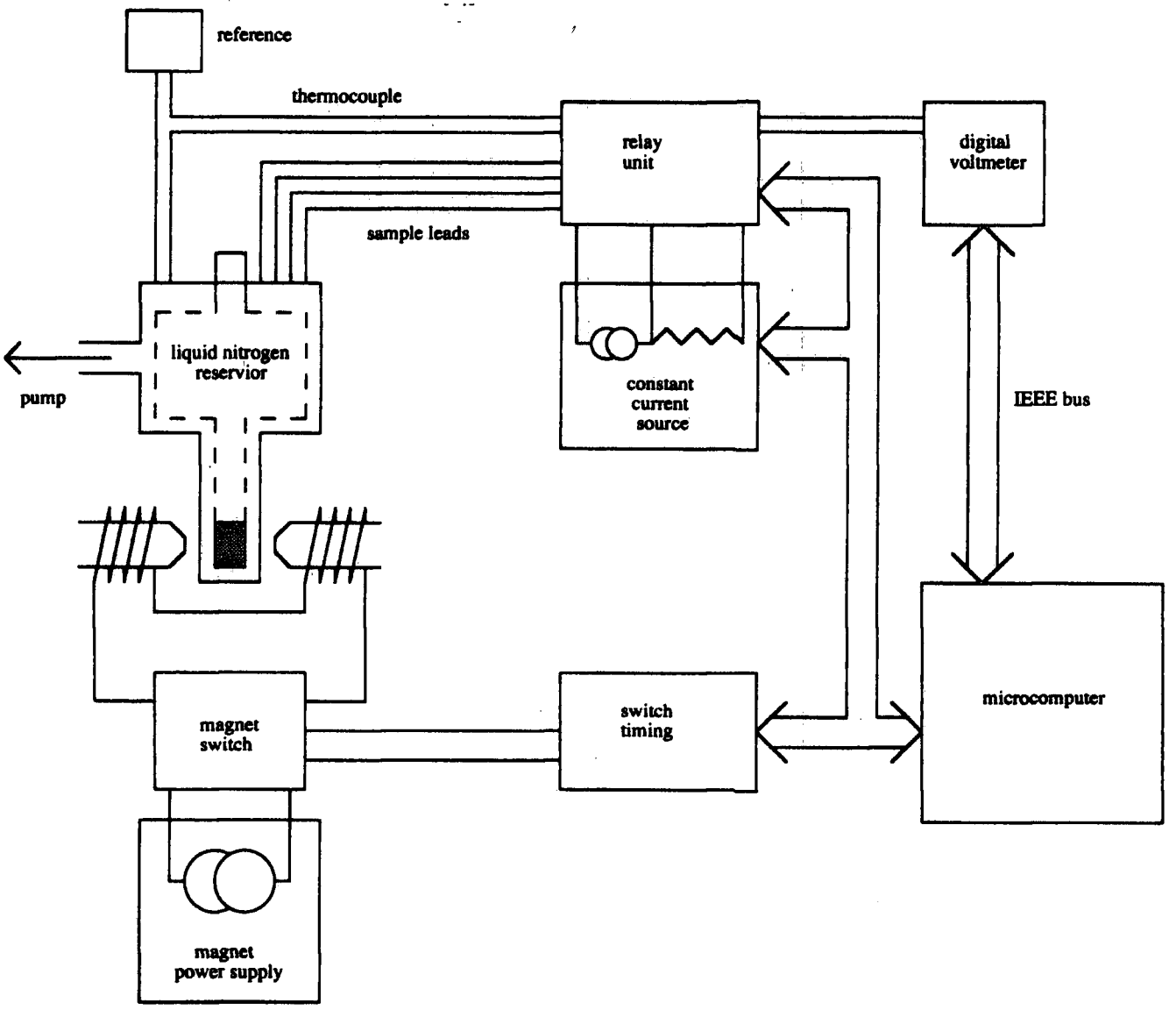

Fig. 3.4 Hall Rig.

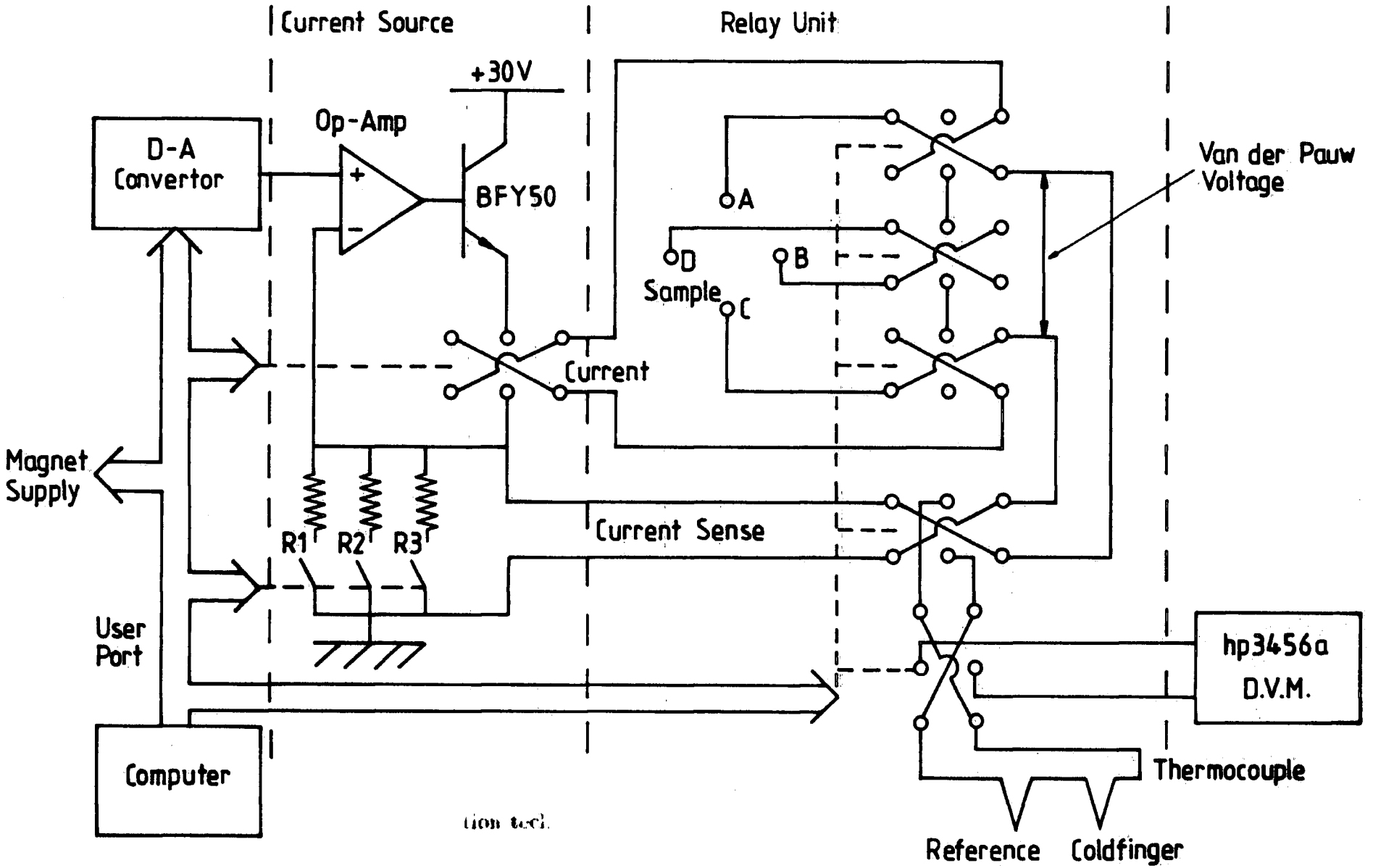

Fig.3.5 Measurement Circuit

to the sample, thermocouple or current sense resistor. The Hewlett Packard hp3456a DVM used has an input impedance $> 10^{10}$ Ω and so loading effects are negligible. Sample currents from 1 μA to 10 mA are provided in three ranges by the constant current source. This is based around an operational amplifier comparator circuit which compares the output from a 12 bit digital to analogue converter with the voltage across one of the three current sense resistors (R1, R2, R3). The operational amplifier has an input impedance > 1.5 TΩ again preventing circuit loading.

Power for the electromagnet is provided by a constant current source rated at 2 A and 200 V. For the work reported here, the magnet current was limited to 1.56 A to avoid overheating of the magnet coils. This current gave a magnetic flux density of 0.16T at the centre of the pole gap. The variation of the field with distance about the centre of pole gap is shown in Fig.3.6 The maximum uncertainty in the position of the sample is represented by a cylindrical volume of radius 10 mm and length 4 mm centered between the pole pieces. This corresponds to an uncertainty in the field of ± 2.5 %. Current switching and field reversal was performed by the circuit shown in Fig.3.7 The magnet stores considerable energy when energised due to the large inductance of the coil. On switch off the protection diode allows the coil current to continue and so dissipate this energy safely without the generation of a large, destructive back e.m.f. In order for this protection to work, it is important that the correct sequence of events is followed during magnet switching. The reversing relay must not switch while power is being supplied to the magnet, and further, it must not switch until any stored energy has been dissipated. In Fig.3.8 the state diagram required for this control is presented. It was not considered safe to use the computer directly to perform this switching as programming errors or system faults could result in illegal switching operations. Therefore a dedicated synchronous circuit was constructed to implement the state diagram with its timing provided by an independent, slow clock. Changes of state can only occur by routes defined in the state diagram at a speed determined by the clock regardless of any input from the computer.

In order to measure the Hall coefficient and resistivity over a range of temperatures, the following procedure was adopted. Firstly, the liquid nitrogen reservoir was filled and the coldfinger allowed to settle at its minimum of $\sim$87K. All six van der Pauw resistances were then measured as described above using the full range of the current source. This yielded four values for the resistivity and two for the Hall coefficient.

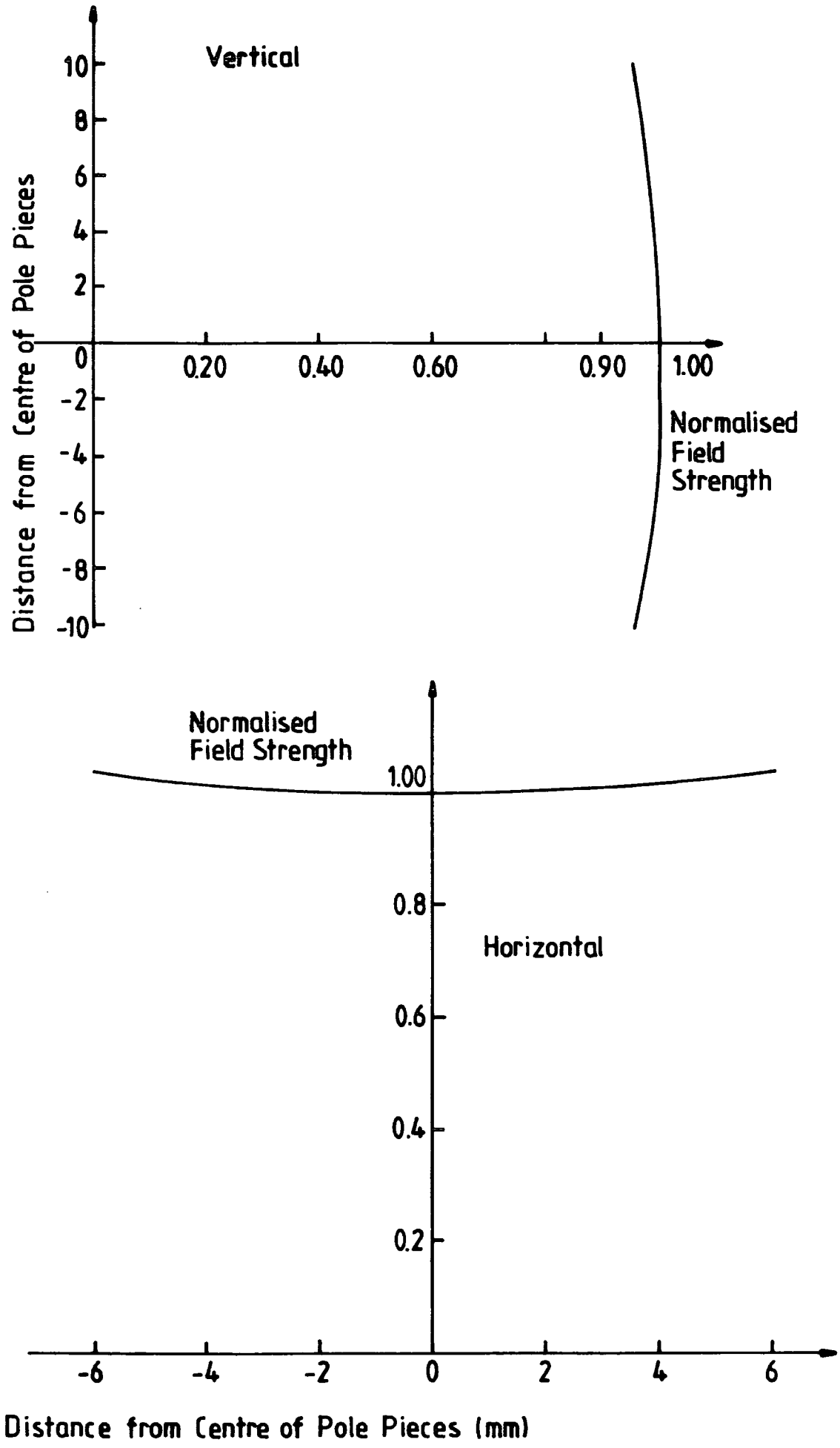

Fig. 3.6 Magnetic Field Variation in Pole Gap.

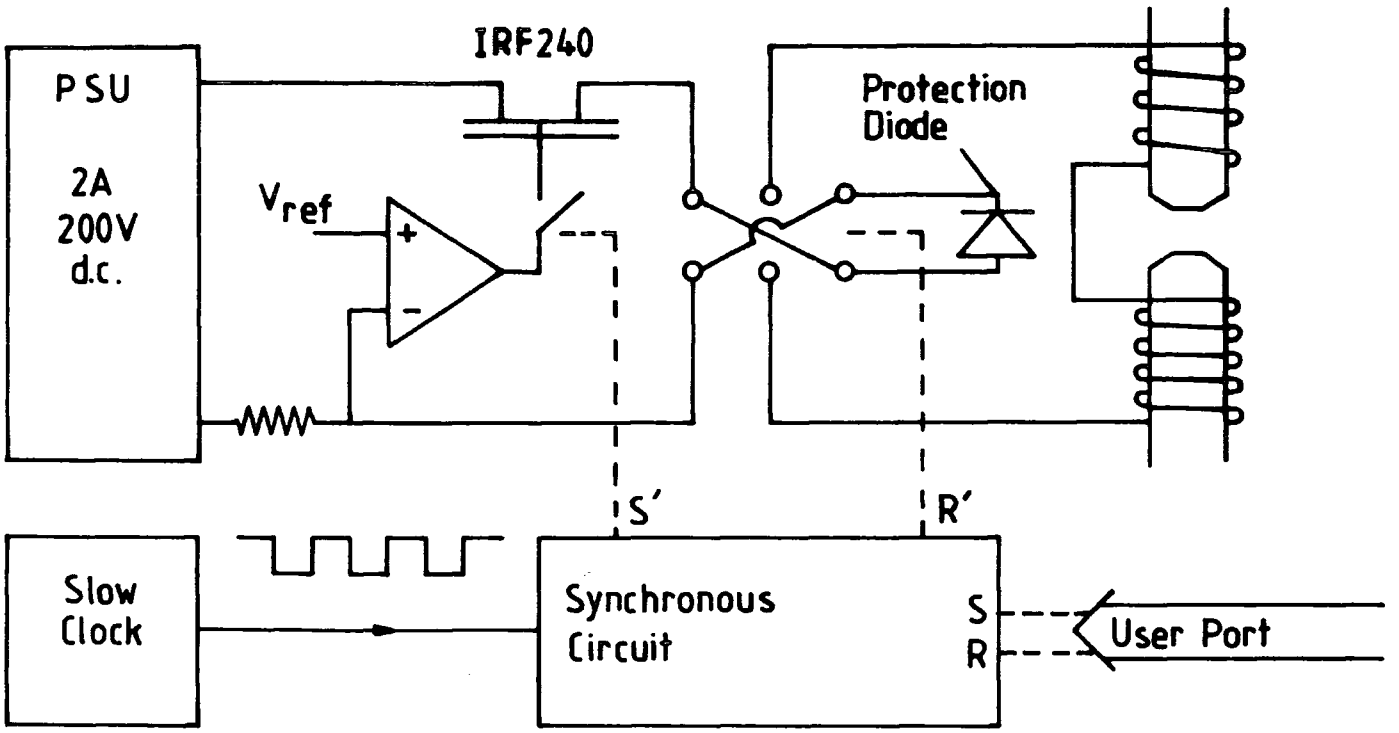

Fig.3.7 Magnet Supply and Switching

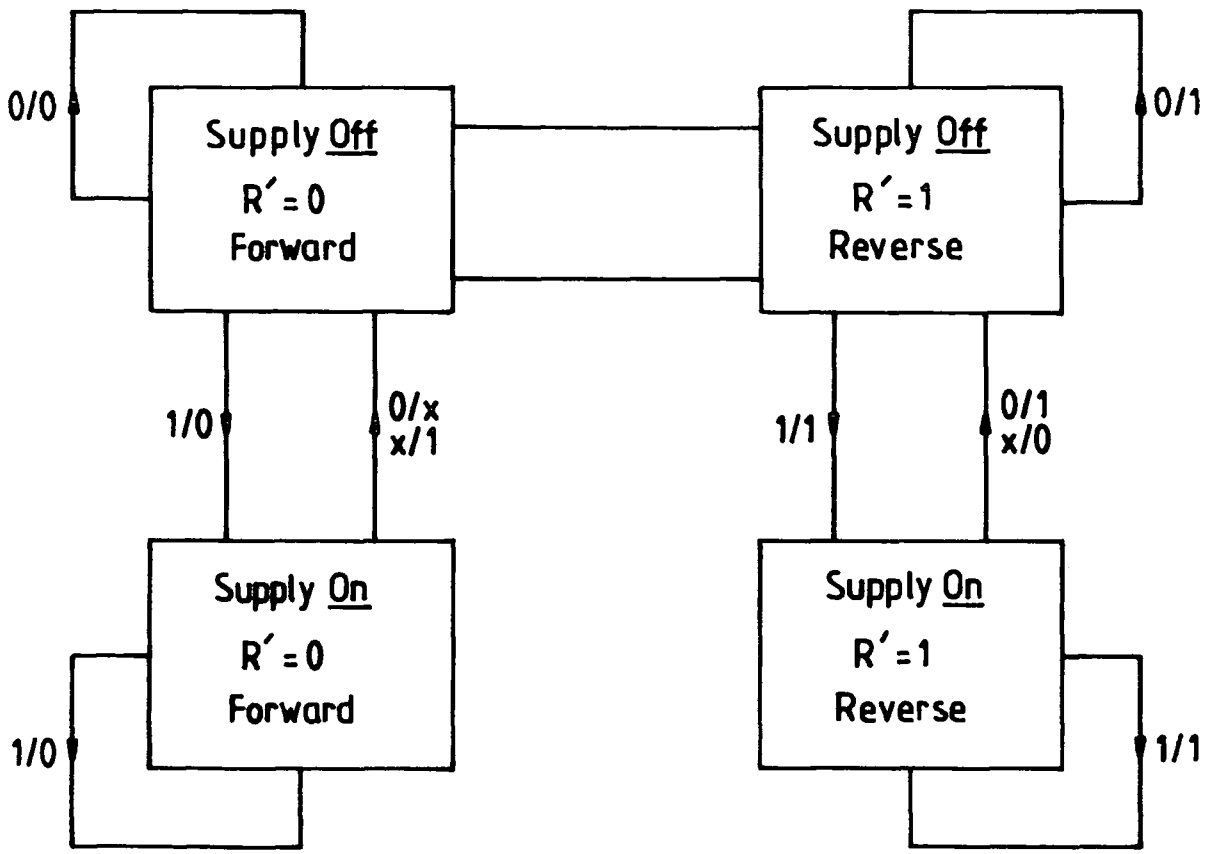

Fig.3.8 State Diagram for Magnet Switching

The scatter in these results together with the linearity of the raw current-voltage data gave an indication of the reliability of the results. If this was satisfactory then two adjacent resistivity, one Hall configuration and one current scale were selected for the temperature scan. The liquid nitrogen was then pumped out of the reservoir and the coldfinger allowed to warm up. At selected temperatures, the computer would perform the reduced set of measurements and store the data for later analysis. The maximum warming rate was 1.6 °C min^{-1} which compares with a time of ~55 sec to perform the set of measurements if four current points are taken in each direction. An average of the temperature immediately before and after the measurements was used in plotting the data. Data could be taken above room temperature by either heating the copper block to the required temperature using a heating coil or by filling the reservoir with hot water and making measurements as the sample cooled. In the latter case the cooling rate at 90 °C was 0.2 °C min^{-1}.

3.3 Infra-red Transmission Spectroscopy

Infra-red transmittance spectra over the wavelength range 2.5μm to 18μm were obtained* for several layers using a Pye Unicam PU9516 infra-red spectrophotometer at the Royal Signals and Radar Establishment, Great Malvern, U.K. The substrates used were transparent over this wavelength range and so it was not necessary to remove them for the measurements. It was, however, important to etch the backs of the wafers to remove any residual deposits which might have contributed to absorption at these wavelengths. This was done using a solution of 2% bromine in methanol with the layer protected by a coat of 'Lacomit' varnish. The analysis of the resulting transmittance data is described in chapter five.

3.4 Electron Microscopy

Scanning Electron Microscopy

Routine assessment of the surface morphology of layers was performed using the secondary electron (SE) mode of a Cambridge Instruments S600 scanning electron microscope (SEM). By viewing cleaved edges of samples it was also possible to obtain an estimate for layer thickness, as there was generally some atomic number contrast

* J.E. Hails, R.S.R.E. Malvern, U.K.

between the substrate and the epitaxial layer. This microscope was also fitted with a facility for the compositional analysis of materials by the energy dispersive analysis of the X-rays (EDAX) generated by the interaction of the electron beam with the sample (Link Systems 860 series 2). Although this analysis was only semi-quantitative it nonetheless proved extremely useful for ensuring that layers were of approximately the required composition before proceeding with further studies. A Cambridge Instruments S180 SEM was also used to assess some of the layers. This instrument was capable of significantly higher resolution than the S600 ($\sim$ 300 Å as opposed to $\sim$ 600 Å) although it was not fitted with an EDAX facility.

Transmission Electron Microscopy

Cross sectional transmission electron microscopy (TEM) was used** to assess the microstructural defect content of some of the epitaxial layers, and also to detect the presence of a multilayer structure in layers intended to be superlattices. This technique offers extremely high resolution ($\sim$ 10 Å) and is sensitive to the strain field in the crystal under observation, thus allowing direct observation of structural defects such as dislocations. A major disadvantage of this technique is that the samples require thinning to electron transparency ($<\sim$ 100Å) before observations can be made. This process is difficult and time consuming and so TEM studies cannot be performed routinely.

3.5 Diffraction Studies

Reflection High Energy Electron Diffraction (RHEED)

The RHEED technique has been comprehensively described by Russell[3] . In essence, this technique involves the diffraction of high energy electrons from the surface of a specimen onto a viewing screen or photographic plate. For the work reported here a modified JEOL JEM120 TEM operating at 80 kV was used. A feature of high energy electron diffraction is that the electron wavelength, λ, is small compared to typical interplanar spacings (in this case $\lambda = 0.04$ Å). Accordingly, the condition for diffraction:

$$k - k' = g \tag{3.4}$$

where k and k' are the incident and diffracted beam wavevectors respectively and

** P.D. Brown, Applied Physics, SEAS, University of Durham.

g is a reciprocal lattice vector, is satisfied when k and k' are almost parallel. Thus, in RHEED, diffraction occurs at grazing incidence. This is illustrated in Fig.3.9(a). The electron beam penetration depth is extremely small and highly dependent on the surface morphology at a microscopic level, and so RHEED is highly surface sensitive, a feature which may be used to advantage in the characterisation of epitaxial layers. As no sample preparation is required, and as the diffraction pattern may be viewed directly on a flouresent screen, RHEED is an excellent method for routine layer characterisation.

Double Crystal X-Ray Diffraction (DCXRD)

In contrast to RHEED, DCXRD[4] uses X-ray radiation with wavelengths close to those of interplanar spacings and the penetration depth of the incident X-ray beam is much greater than that of an electron beam. The technique is shown schematically in Fig.3.9(b). The X-ray beam is first diffracted by a reference crystal of extremely high quality before being diffracted by the specimen and then detected. The use of a reference crystal in this way allows the diffraction spectrum from the specimen to be observed with extremely high angular resolution (seconds of arc) and this allows a detailed study of the structure of the specimen to be made. Dislocations and other structural defects are equivalent to localised variations in orientation and lattice parameter of the layer and so tend to broaden the diffraction peaks. The Full Width Half Maximum (FWHM) of a diffraction peak may therefore be taken as a measure of the quality of the epitaxial layer.

The X-ray diffraction studies performed*** during the course of the work reported in this thesis were made with a Bede Scientific double crystal X-ray diffractometer using Cu K_α radiation ($\lambda = 1.54$ Å) and a GaAs reference crystal.

*** A. Turnbull, Solid State Physics Group, Department of Physics, University of Durham.

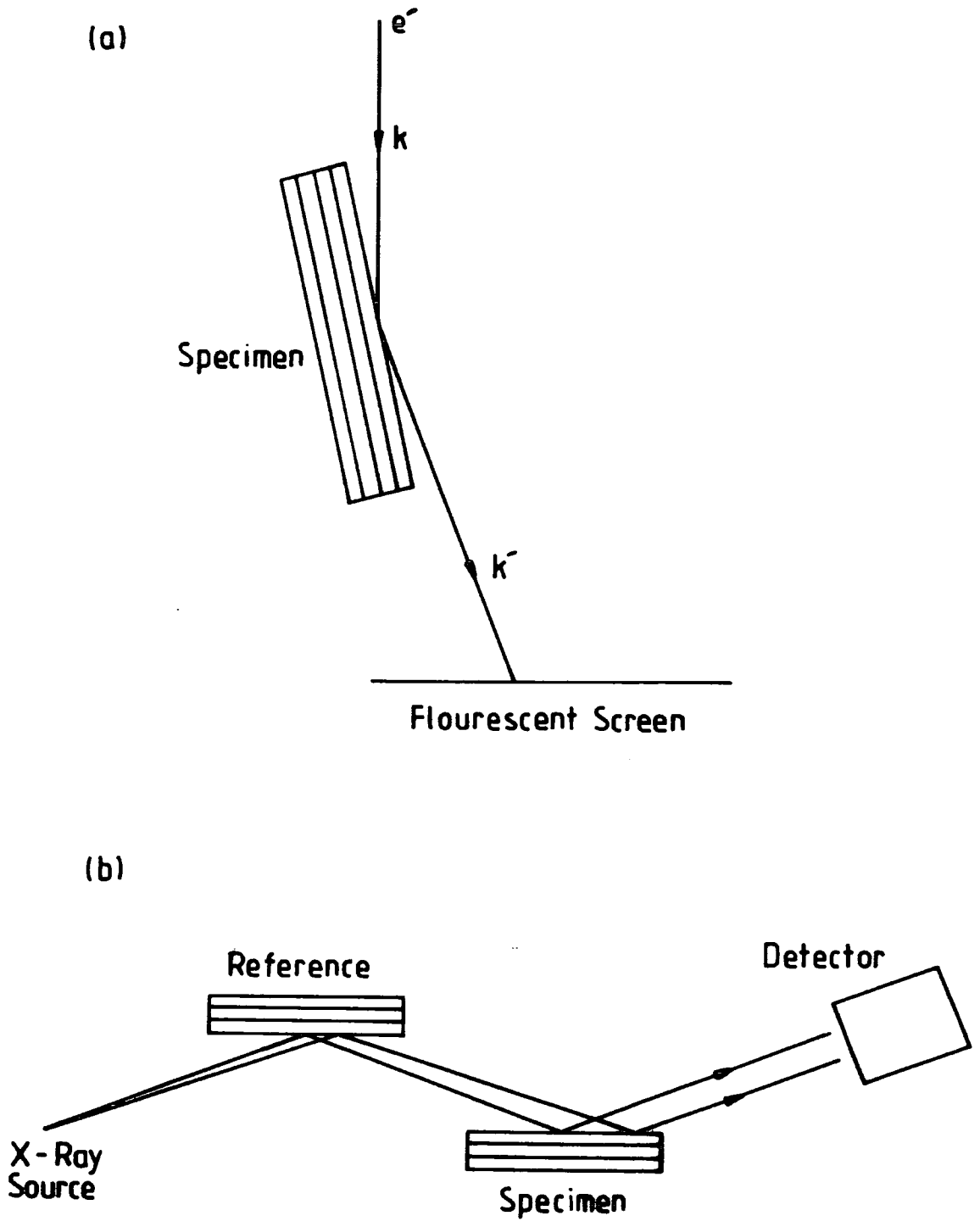

Fig.3.9**Diffraction techniques** (a) Reflection High Energy Electron Diffraction. (b) Double Crystal X-ray Diffraction.

REFERENCES

1. L.J. van der Pauw, Philips Research Reports **13**, 1 (1958).
2. H.H. Weider in Nondestructive Evaluation of Semiconductor Materials and Devices Ed. J.N. Zemel NATO ASI series **B46** (1979)
3. G.J. Russell, Prog. Crystal Growth and Charact. **5** (1982) 291.
4. B.K. Tanner, J. Electrochem. Soc. **136** (1989) 3438.

4. Interpretation of Electrical Transport Data

4.1 Introduction

In this chapter the model used in chapter five to interpret the temperature dependence of transport data obtained from $Hg_{1-x}Cd_xTe$ samples is described. This analysis is dominated by two of the fundamental properties of $Hg_{1-x}Cd_xTe$. Firstly low x $Hg_{1-x}Cd_xTe$ is a narrow-gap semiconductor. This means that, at ordinary temperatures, intrinsic carriers may contribute significantly to conduction. Secondly, the ratio of electron to hole mobilities is very high (~ 100)[1] and so in p-type material even low concentrations of intrinsic electrons or electrons in a surface inversion layer can influence transport measurements significantly. The effects of inversion layers may be particularly significant in thin epitaxial films, such as those considered here, which may be dominated by such effects. Several workers[2-4] have successfully used multicarrier/multilayer models to interpret transport data from $Hg_{1-x}Cd_xTe$ samples and this approach has been adopted here.

In section 4.2 an overview of the statistics of carriers in semiconductors[5] is presented. The Hall effect for one carrier is described in section 4.3 on the basis of the relaxation time approximation[6] . This is extended in section 4.4 into a model for multicarrier/multilayer transport which forms the basis of the transport model, used in this work, for $Hg_{1-x}Cd_xTe$. It is shown that, at low fields, the effect of multilayer transport is essentially the same as multicarrier transport and that a two carrier model may be used regardless of the distribution of carriers in a layer provided suitable parameters are used. In section 4.5, the effect on carrier concentrations of inversion layers on p-type material is discussed. The ideas contained in these four sections are combined in section 4.6 to form the transport model for $Hg_{1-x}Cd_xTe$. Examples of the application of this model, made under the simplifying assumption of constant mobilities, to p-type, n-type and inverted p-type material are also given. This serves to illustrate the various limits of the transport model and the information which can be obtained from it.

4.2 Semiconductor Statistics

The probability $f(\epsilon)$ that an electronic state of energy ϵ is occupied by an electron is given by the Fermi-Dirac function:

$$f(\epsilon) = \frac{1}{1 + exp\left(\frac{\epsilon - \epsilon_F}{kT}\right)} \tag{4.1}$$

where ϵ_F is the Fermi energy, k is Boltzmann's constant and T is the absolute temperature. For a semiconductor the concentration of electrons in the conduction band, n_e or holes in the valence band n_h is given by the integral over all possible states of the corresponding density of states function $g_c(\epsilon)$ or $g_v(\epsilon)$ multiplied by the probability of each state being occupied by either an electron or a hole:

$$n_h = \int_{-\infty}^{\epsilon_v} g_v(\epsilon).(1 - f(\epsilon))d\epsilon \tag{4.2}$$

$$n_e = \int_{\epsilon_c}^{\infty} g_c(\epsilon).f(\epsilon)d\epsilon \tag{4.3}$$

where ϵ_c and ϵ_v are the energies of conduction and valence band edges respectively.

For a semiconductor with parabolic bands which can be described by electron and hole effective masses m_e^* and m_h^* this can be expressed, including spin, as:

$$n_h = 2.2\pi\left(\frac{2m_h^*}{h^2}\right)^{\frac{3}{2}}.\int_{-\infty}^{\epsilon_v} \frac{(\epsilon_v - \epsilon)^{\frac{1}{2}}}{1 + exp(\frac{\epsilon_F - \epsilon}{kT})}d\epsilon \tag{4.4}$$

$$n_e = 2.2\pi\left(\frac{2m_e^*}{h^2}\right)^{\frac{3}{2}}.\int_{\epsilon_c}^{\infty} \frac{(\epsilon - \epsilon_c)^{\frac{1}{2}}}{1 + exp(\frac{\epsilon - \epsilon_F}{kT})}d\epsilon \tag{4.5}$$

Under non-degenerate conditions, Maxwell-Boltzman statistics apply and the integrals simplify to exponentials:

$$n_h = 2\Big(\frac{2\pi m_h^* kT}{h^2}\Big)^{\frac{3}{2}} exp\Big(\frac{\epsilon_v - \epsilon_F}{kT}\Big) \tag{4.6}$$

$$n_e = 2\Big(\frac{2\pi m_e^* kT}{h^2}\Big)^{\frac{3}{2}} exp\Big(\frac{\epsilon_F - \epsilon_c}{kT}\Big) \tag{4.7}$$

The pre-exponential factors may be defined as effective densities of states:

$$N_v^* = 2\Big(\frac{2\pi m_h^* kT}{h^2}\Big)^{\frac{3}{2}} \tag{4.8}$$

$$N_c^* = 2\Big(\frac{2\pi m_e^* kT}{h^2}\Big)^{\frac{3}{2}} \tag{4.9}$$

It can be seen from (4.6) and (4.7) that at any given temperature the product $n_h.n_e$ is a constant for the material regardless of doping depending only on the effective densities of states and the energy gap. Moreover it may be written as the square of the intrinsic carrier concentration n_i:

$$n_h.n_e = n_i^2 = N_c^*.N_v^* exp\Big(\frac{\epsilon_v - \epsilon_c}{kT}\Big) \tag{4.10}$$

n_i is strongly dependent on temperature and may be of significant magnitude in a semiconductor with a small energy gap ($\epsilon_c - \epsilon_v$). In $Hg_{1-x}Cd_xTe$ this strong temperature dependence of n_i gives rise to temperature dependent carrier concentrations and so to a corresponding temperature dependence of the electrical transport.

Doped Material

For p-type material with a single acceptor level at an energy ϵ_a above the valence band the concentration of ionised acceptors, N_a^- is given by the product of the acceptor concentration, N_a, and the Fermi-Dirac function (4.1):

$$N_a^- = \frac{N_a}{1 + 4.exp\left(\frac{\epsilon_v - \epsilon_F + \epsilon_a}{kT}\right)} \tag{4.11}$$

where the pre-exponential factor of 4 accounts for the fourfold degeneracy of the valence band.

Charge neutrality requires that:

$$N_a^- = n_h - n_e \tag{4.12}$$

which for non-degenerate conditions may be rewritten using (4.10) as:

$$Na^- = n_h - \frac{n_i^2}{n_h} \tag{4.13}$$

Substituting equations (4.6) and (4.11) into (4.13)yields for the hole concentration:

$$n_h = \frac{N_a}{1 + \frac{n_h}{2N_v} 4exp\left(\frac{\epsilon_a}{kT}\right)} + \frac{n_i^2}{n_h} \tag{4.14}$$

This expression may be solved numerically to yield n_h.

The corresponding expression for donor doped material, where the conduction band degeneracy is 2, is:

$$n_e = \frac{N_d}{1 + \frac{n_e}{2N_c} 2exp\left(\frac{\epsilon_d}{kT}\right)} + \frac{n_i^2}{n_e} \tag{4.15}$$

It can be seen that the dopants will be essentially fully ionised when the ionisation energy, ϵ_a or ϵ_d is small compared to kT and the carrier concentration is small compared to the corresponding effective density of states. When both these conditions are satisfied then (4.14) and (4.15) simplify to:

$$n_h \simeq \frac{N_a + \sqrt{N_a^2 + 4n_i^2}}{2} \tag{4.16}$$

and:

$$n_e \simeq \frac{N_d + \sqrt{N_d^2 + 4n_i^2}}{2} \tag{4.17}$$

4.3 The Hall Effect for One Carrier

The principle of the Hall effect is illustrated in Fig. 4.1 for the case of a homogeneous semiconductor where conduction is due solely to holes. Holes move with a velocity v_x in the x direction due to the applied electric field $\mathcal{E}_x$ causing a current, I_x, to flow in the external circuit. Due to the magnetic field, B_z in the z direction, a Lorentz force, F_B acts on the holes in the y direction. As no current can flow in the y direction, then an electric field, $\mathcal{E}_y$, must exist which acts to oppose F_B :

$$-q\underset{y}{\mathcal{E}} = F_B = qv_xB_z \tag{4.18}$$

where q is the magnitude of the electronic charge.

$\mathcal{E}_y$ gives rise to the Hall voltage V_H.

If the holes may be regarded as particles with a single effective mass, m_h^*, moving under the influence of the electric and magnetic fields existing in the sample with scattering being accounted for by the assumption of a relaxation time, τ, which is in general a function of energy, then the equations of motion may be solved to give the following result:

$$\frac{V_H d}{I} = \frac{\frac{(n_h q^2\omega/m_h^*)<\tau^2>}{1+\omega^2<\tau^2>}}{\left(\frac{(n_h q^2/m_h^*)<\tau>}{1+\omega^2<\tau^2>}\right)^2 + \left(\frac{(n_h q^2\omega/m_h^*)<\tau^2>}{1+\omega^2<\tau^2>}\right)^2} \tag{4.19}$$

where d is the layer thickness, and ω is the cyclotron frequency given by:

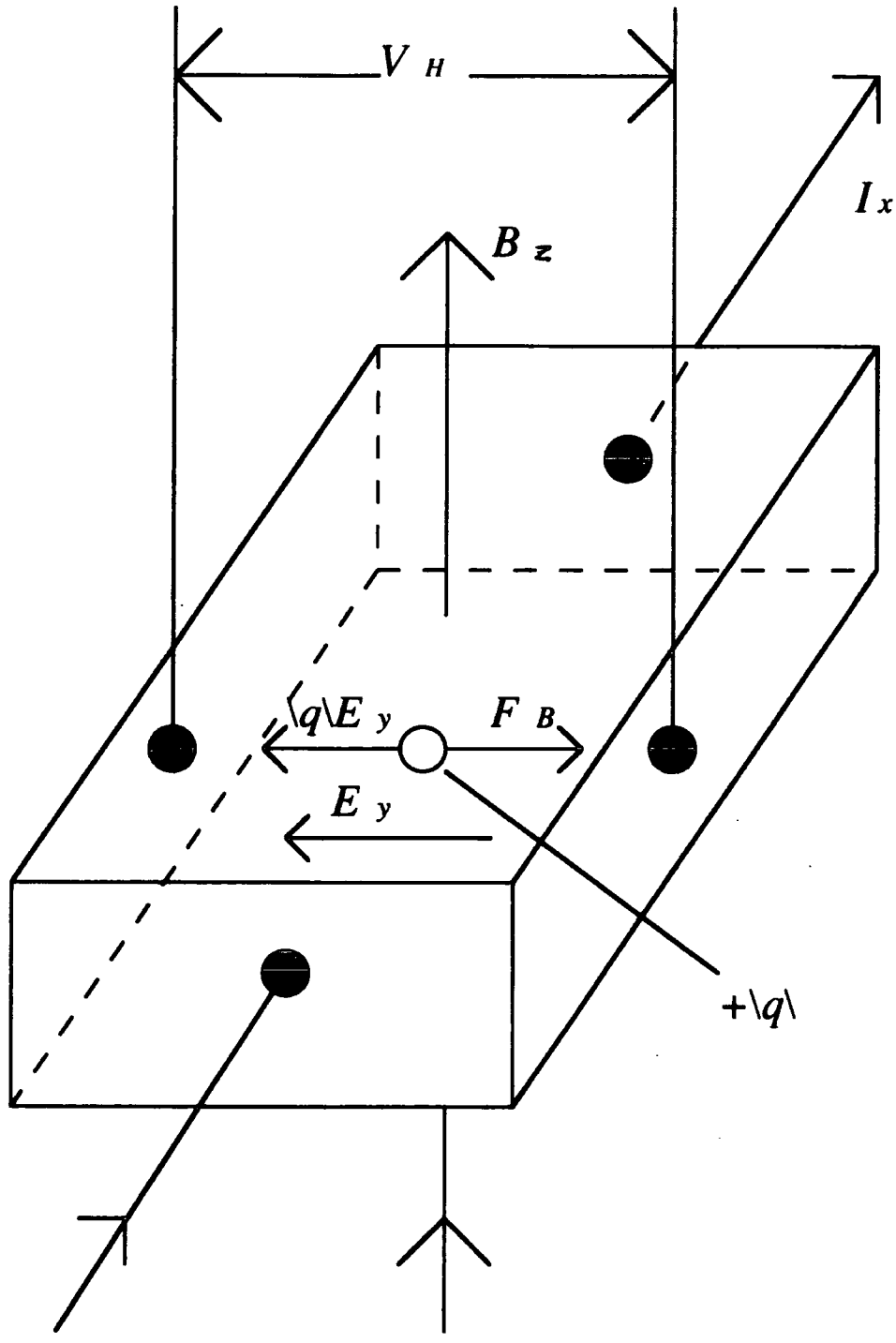

Fig. 4.1 The Hall effect for 1 carrier (holes).

$$\omega = \frac{qB}{m_h^*} \tag{4.20}$$

$< \tau^2 >$ and $< \tau >^2$ are the effective average square of the relaxation time and the square of the average relaxation time respectively. B is the magnitude of the magnetic field.

The mobility μ_h is related to the relaxation time by the following relationship:

$$\mu_h = \frac{q < \tau >}{m_h^*} \tag{4.21}$$

Using this expression together with (4.20), it can be seen that the $1 + \omega^2\tau^2$ terms in expression for the Hall voltage (4.19) are approximately equal to $1 + B^2\mu_h^2$. For the case of a low field-mobility product, this term is close to unity and (4.19) may be recast to give:

$$R_H = \frac{V_H d}{IB} = \frac{1}{qn_h} . \frac{< \tau^2 >}{< \tau >^2} = \frac{r_H}{qn_h} \tag{4.22}$$

where R_H is defined as the Hall coefficient and r_H as the Hall scattering factor. The mobility is related to the resistivity by:

$$\rho = \frac{1}{n_h q \mu_h} \tag{4.23}$$

and so the ratio of the Hall coefficient to the resistivity is:

$$\frac{R_H}{\rho} = \mu_h r_H \tag{4.24}$$

which is defined as the Hall mobility.

The Hall scattering factor is determined by the energy dependence of the scattering mechanism in the sample under consideration and is of the order of unity. It may be shown[6] that for ionised impurity scattering, $r_H = 1.93$ while for lattice scattering

it equals 1.18. If the scattering mechanism is independent of energy then r_H will be identically equal to 1. For the transport data reported in chapter five, evidence was only found for the latter two scattering mechanisms. On this basis the multicarrier/multilayer model in section (4.4) was developed assuming $r_H = 1$.

4.4 The Multicarrier/Multilayer Model for Electrical Transport

In order to model the Hall coefficient and resistivity observed in semiconductor samples exhibiting multicarrier/multilayer conduction it is first necessary to consider the Hall voltage, V_H and resistivity, ρ observed in a homogeneous sample containing several different kinds of carrier[6] :

$$\frac{V_H d}{I} = \frac{\Sigma D_j}{(\Sigma A_j)^2 + (\Sigma D_j)^2} \tag{4.25}$$

where:

$$A_j = \frac{n_j q_j \mu_j}{1 + B^2 \mu_j^2} \quad , \quad D_j = \frac{n_j q_j \mu_j^2 B}{1 + B^2 \mu_j^2}.$$

and

$$\rho = \frac{1}{\Sigma n_j |q_j| \mu_j} \tag{4.26}$$

n_j, q_j and μ_j are the concentration, charge and mobility of the jth carrier and B, I and d are the magnetic field, current and sample thickness. For a field mobility product much less than unity, the $1 + B^2\mu^2$ denominators of A_j and D_j are close to unity and $(\Sigma D_j)^2$ is much smaller than $(\Sigma A_j)^2$. For mobilities in $Hg_{1-x}Cd_xTe$ and the magnetic field of 0.16 T used for the work reported in this thesis, this condition is satisfied. Using this low-field approximation and assuming conduction is by electrons and holes, represented by subscripts e and h, each with a single mobility allows simplification of equations (4.25) and (4.26) yielding:

$$R_H = \frac{V_H d}{IB} = \frac{n_h q \mu_h^2 - n_e q \mu_e^2}{(n_h q \mu_h + n_e q \mu_e)^2} \tag{4.27}$$

$$\rho = \frac{1}{n_h q \mu_h + n_e q \mu_e} \tag{4.28}$$

It can be seen that when one carrier dominates, these expressions simplify to those expected from the single carrier model developed in the previous section ((4.22) , (4.23)).

Equation (4.27) may be rewritten as:

$$R_H = \frac{n_h - b^2 n_e}{q(n_h + b n_e)} \tag{4.29}$$

where b is the electron to hole mobility ratio, $\frac{\mu_e}{\mu_h}$. In other words, for two carrier conduction, the Hall coefficient is dependent only on the ratio of the carrier mobilities, not their actual values.

For the case of two different kinds of carrier distributed through a layer of total thickness d in two sub-layers, represented by subscripts 1 and 2, of thickness d_1 and d_2, Petritz[7] gives the following expression for the observed values of R_H and the conductivity, σ, in terms of the Hall coefficient and conductivity, σ, that the sub-layers would exhibit individually:

$$R_H = \frac{d(R_{H1}\sigma_1^2 d_1 + R_{H2}\sigma_2^2 d_2)}{(\sigma_1 d_1 + \sigma_2 d_2)^2} \tag{4.30}$$

$$\rho = \frac{d}{\sigma_1 d_1 + \sigma_2 d_2} \tag{4.31}$$

Substituting:

$$R_{H1,2} = \frac{1}{q_{1,2} n_{1,2}} \quad , \quad \sigma_{1,2} = n_{1,2} q \mu_{1,2} \tag{4.32}$$

and rearranging gives:

$$R_H = \frac{n_1 \frac{d_1}{d} q_1 \mu_1^2 + n_2 \frac{d_2}{d} q_2 \mu_2^2}{(n_1 \frac{d_1}{d} q_1 \mu_h + n_2 \frac{d_2}{d} q_2 \mu_2)^2} \tag{4.33}$$

$$\rho = \frac{1}{n_1 \frac{d_1}{d} q \mu_1 + n_2 \frac{d_2}{d} q \mu_2} \tag{4.34}$$

Comparison with equations (4.27) and (4.28) shows that the effect of a concentration n' of carriers in a sub-layer of thickness d' is identical to an effective concentration n^* distributed uniformly throughout the total thickness of the layer where:

$$n^* = \frac{d'}{d} n' \tag{4.35}$$

Thus the Hall coefficient and resistivity are dependent solely on the total number and mobility of each kind of carrier in the layer together with the total thickness. A consequence of this is that low-field transport data of samples exhibiting layered conduction contain no information on the thicknesses of the sub-layers.

To summarise the two carrier expressions (4.27) and (4.28) may be used to model the Hall and resistivity data from samples exhibiting both mixed and layered conduction if a single electron mobility and a single hole mobility are assumed by appropriate choice of effective carrier concentrations.

4.5 Inversion Layers on p-type $Hg_{1-x}Cd_xTe$

An electron energy diagram representing an inverted p-type $Hg_{1-x}Cd_xTe$ surface is given in Fig. 4.2. It is assumed that a thin oxide layer exists at the surface and that this contains a fixed sheet charge density Q_s. This sheet of charge in the oxide then induces an equal but opposite charge at the surface of the semiconductor which produces band bending, Ψ, as shown. The charge in the semiconductor is composed of a depletion charge with areal density Q_d, and a sheet charge, N_s, due to the generation of electrons caused by the band bending at the surface. These charges are related by[8] :

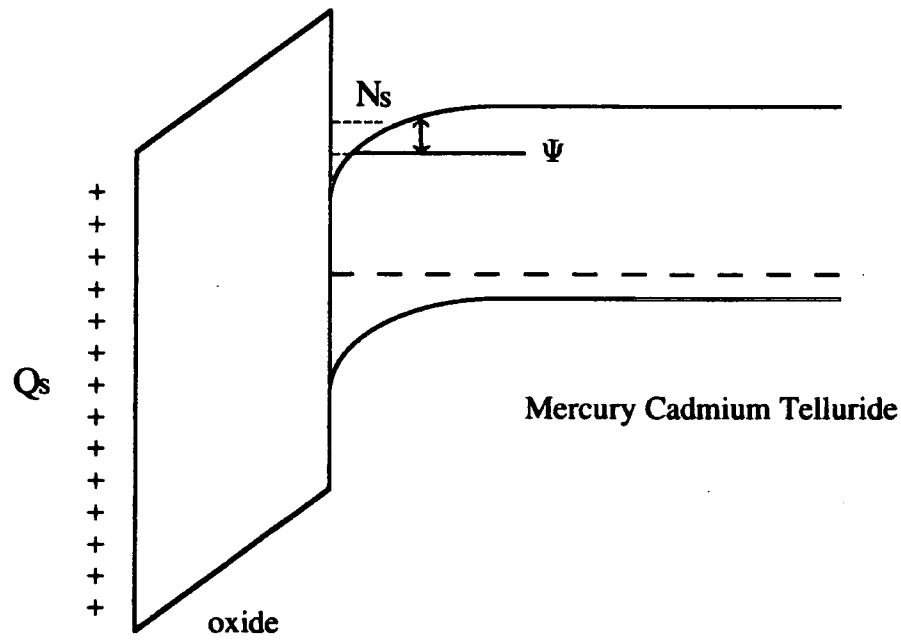

Fig. 4.2 Inversion Layer at the Surface of p-type Mercury Cadmium Telluride.

$$-Q_s = Q_d + N_s \tag{4.36}$$

Once the charge in the oxide is sufficient to generate inversion electrons, further increase in Q_d is prevented by the screening effect of the electron charge[8] and so N_s may be taken as a constant if the oxide charge is assumed to be fixed.

The electron concentration generated at the surface by the band bending gives rise to electronic conduction in inversion layers on p-type material and so leads to anomalous transport data. Such effects may be accounted for in the multicarrier/multilayer model described in the previous section by the assumption of an effective inversion layer concentration, n_s, given by:

$$n_s = \frac{N_s}{d} \tag{4.37}$$

where d is the total layer thickness.

Support for the assumption of an oxidised surface layer as an explanation for anomalous transport data for $Hg_{1-x}Cd_xTe$ is given by Mullin and Royle[9] who obtained anomalous Hall data from initially p-type $Hg_{1-x}Cd_xTe$ by oxidising samples in air, and by Nasir et al.[10] who were able to alter the inversion layer electron concentration by changing the oxide charge by illuminating samples with photons having energies greater than the oxide energy gap (3.4 eV).

4.6 Transport Model for $Hg_{1-x}Cd_xTe$

As described in section 4.4, the principal requirement for calculation of the Hall coefficient and resistivity of a layer is the average or effective concentration of each kind of carrier together with their corresponding mobilities. For a given doping concentration and temperature, the electron and hole concentrations may be calculated using equations (4.14) or (4.15) together with (4.10). It is important to note that in using these expressions for material where conduction takes place in sublayers of differing doping, the actual dopant or carrier concentration must be used rather than the effective concentrations used in the expressions for R_H and ρ. The large ratio of the electron to hole mobilities in $Hg_{1-x}Cd_xTe$ means that in p-type layers intrinsic electrons are important

even for material with a large acceptor concentration and conversely that intrinsic holes are of little importance in n-type material. In section 4.2 it was shown that the intrinsic carrier concentration n_i relates the electron and hole concentrations. In this work n_i was determined as a function of composition x and temperature using the semi-empirical expression of Hansen and Schmit[11] :

$$n_i = (5.585 - 3.820x + 1.753 \times 10^{-3}T - 1.364 \times 10^{-3}xT)E_g^{\frac{3}{4}} \times [10^{14}T^{\frac{3}{2}}exp(\frac{-Eg}{2kT})] \quad (4.38)$$

This is essentially the expression (4.10) for n_i for parabolic bands modified by a prefactor which takes account of band non-parabolicity. It was based on a fit to values of n_i calculated theoretically and agrees well with values determined experimentally by the authors. Taking non-parabolicity into account in this way allows the use of the statistics developed in section 4.2. The energy gap E_g used in this relation was determined as a function of x and T from the expression of Hansen et al[12] :

$$E_g = -0.302 + 1.93x - 0.810x^2 + 0.832x^3 + 5.35 \times 10^{-4}(1 - 2x)T \quad (4.39)$$

as used by Hansen and Schmit[11] in their calculation of n_i. This expression for the energy gap has been widely used[13] and has been tested for x values of < 0.6 and temperatures up to 300 K. Outside of this range it provides a first approximation. It is also used in this thesis to determine composition from optical transmission measurements and so provides for consistent treatment of both the optical and electrical data.

The procedure adopted to model R_H and ρ as a function of temperature using the two carrier model described in section 4.4 was as follows:

1.) Develop a model for the layer consisting of appropriate p-type and n-type sub-layers of particular type, mobility, thickness and doping concentration.

2.) Determine any effective inversion layer electron concentration.

3.) For each temperature

a.) For each sub-layer calculate n_h and n_e.

b.) Calculate total effective hole and electron concentrations.

c.) Calculate R_H and ρ.

In calculating the hole concentrations, equation (4.14) was used assuming the hole effective mass to be 0.55 times the free electron mass and the acceptor ionisation energy to be 10 meV as used by Lacklison and Capper[3] . Electron concentrations were determined using (4.17) as freeze-out of electrons is not generally observed in $Hg_{1-x}Cd_xTe$ at the temperatures used here[2] .

Examples of the application of the two carrier model to $x = 0.3$ $Hg_{1-x}Cd_xTe$ are shown in Figs. 4.3 to 4.6. These plots were made under the simplifying assumptions of constant mobilities equal to 100 $cm^2V^{-1}s^{-1}$ for holes and 10000 $cm^2V^{-1}s^{-1}$ for electrons and with dopant ionisation energies set to zero.

P-type Material

Fig. 4.3 shows the predicted behaviour of acceptor doped material with no inversion layer. In curve A, a $Hg_{1-x}Cd_xTe$ layer with a uniform acceptor concentration of 1×10^{17} cm^{-3} is represented, while in curve B a $Hg_{1-x}Cd_xTe$ layer of the same composition and total thickness but arbitrarily divided into two sub-layers of equal thickness having acceptor concentrations of 2.3×10^{17} cm^{-3} and 1×10^{15} cm^{-3} is depicted. At low temperatures, R_H is positve and of the same magnitude for both A and B since the effective hole concentration is the same in both cases. It should be noted that the acceptor concentration in the higher doped region of B is more than twice that of A. Although the ionisation energy has been set to zero, ionisation is still limited due to the finite density of valence band states according to (4.14) . In case A, 84% of acceptors are ionised while in case B this is reduced to 73% . As the temperature inceases, acceptor ionisation increases causing R_H to fall slowly. At the same time intrinsic electrons are generated according to (4.10). It can be seen that electron generation in the low doped

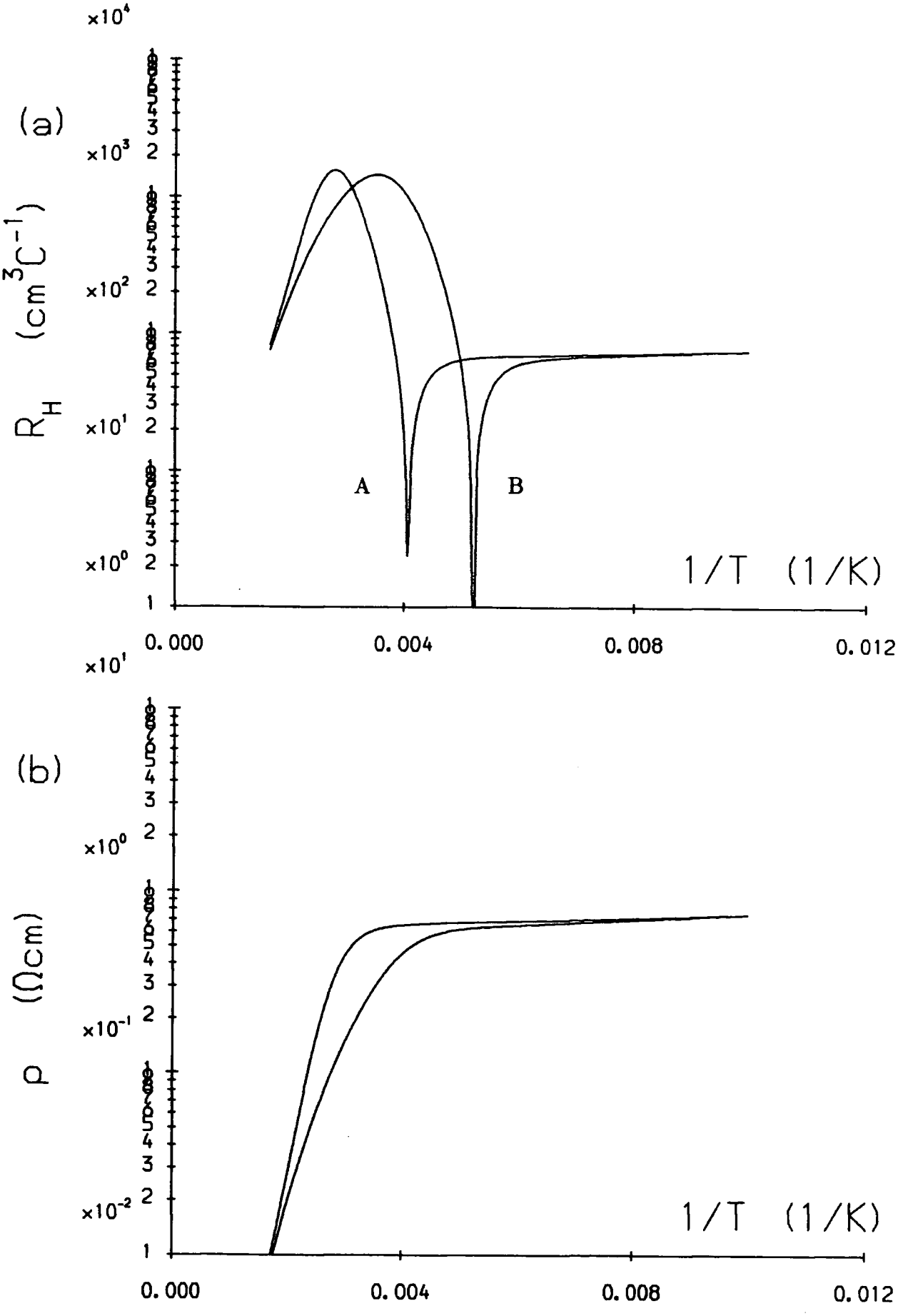

Fig. 4.3. Hall coefficient, R_H, and resistivity, ρ, for p-type $x = 0.3$ $Hg_{1-x}Cd_xTe$ with (A) a uniform acceptor concentration, (N_a), of 1×10^{17} cm^{-3} and (B) 2 equal sub-layers with $N_a = 2.3 \times 10^{17}$ cm^{-3} and $N_a = 1 \times 10^{15}$ cm^{-3}. The hole and electron mobilities are 100 cm^{2}V^{-1}s^{-1} and 10000 cm^{2}V^{-1}s^{-1} respectively.

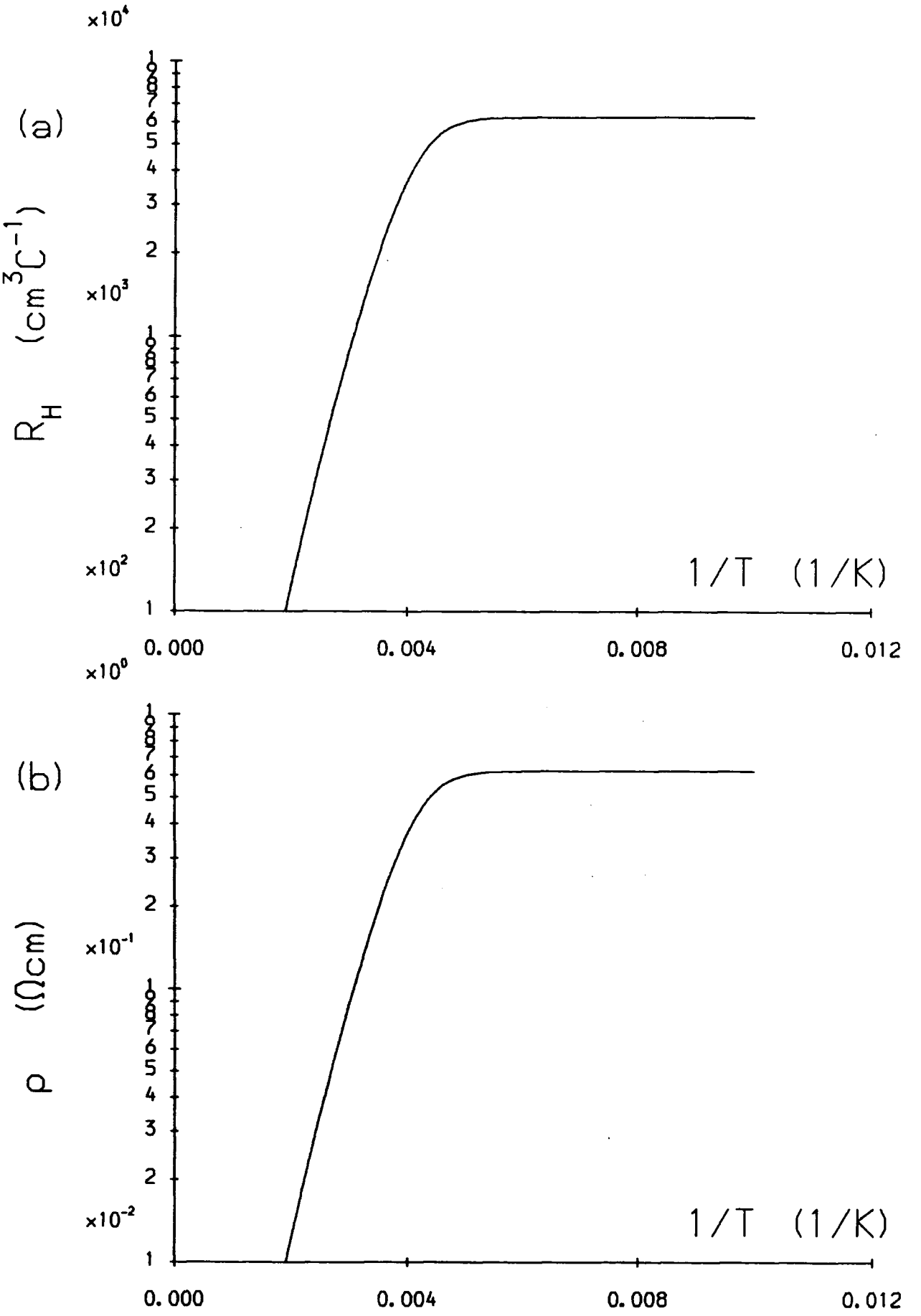

Fig. 4.4. Hall coefficient, R_H, and resistivity, ρ, for n-type $x = 0.3$ $Hg_{1-x}Cd_xTe$ with a uniform donor concentration, of 1×10^{15} cm^{-3}. The electron mobility is 10000 $cm^2V^{-1}s^{-1}$.

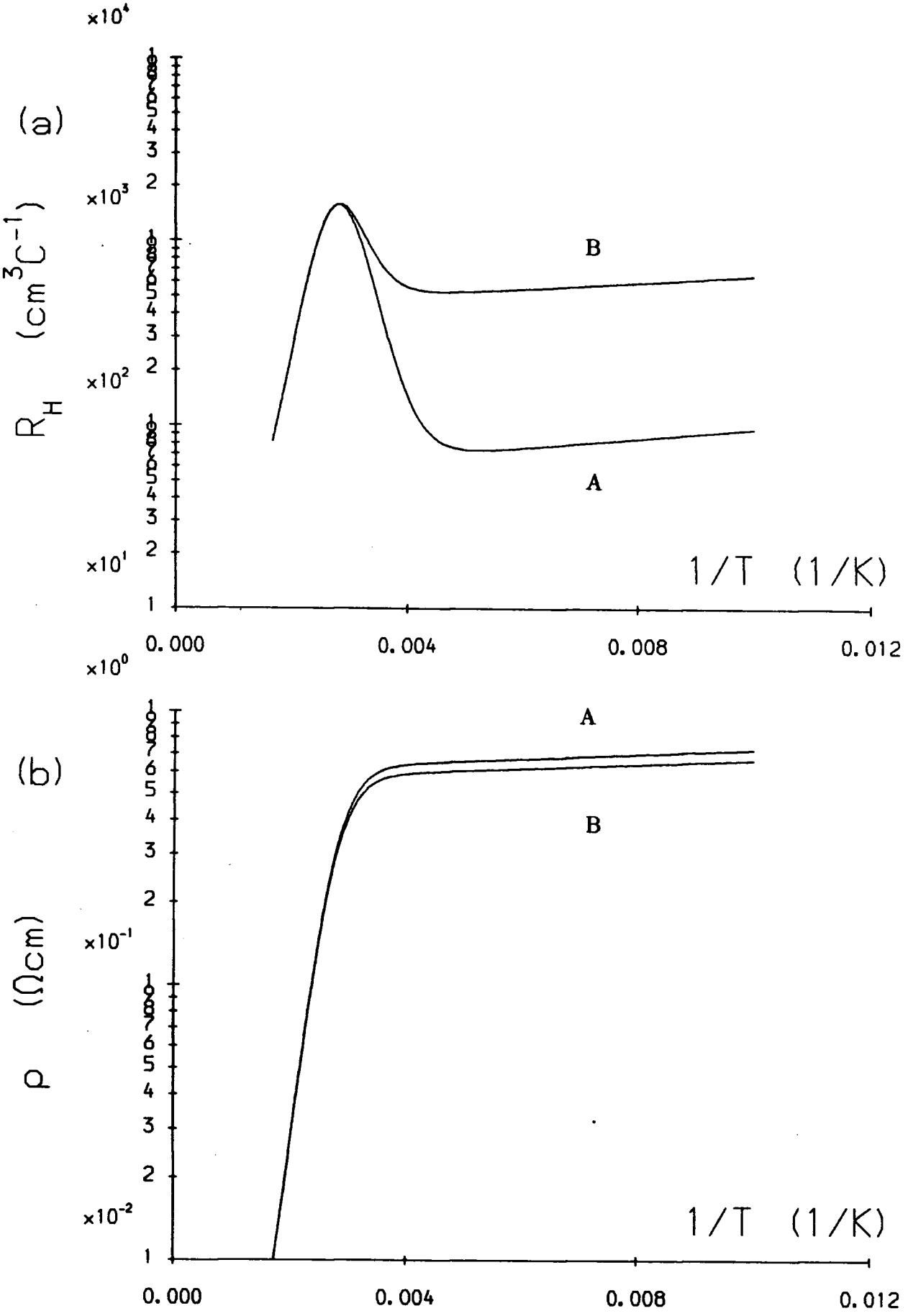

Fig. 4.5. Hall coefficient, R_H, and resistivity, ρ, for weakly inverted p-type $x = 0.3$ $Hg_{1-x}Cd_xTe$ with a uniform acceptor concentration of 1×10^{17} cm^{-3} and effective inversion layer concentrations of (A) 2×10^{13} cm^{-3} and (B) 1×10^{14} cm^{-3}. The hole and electron mobilities are 100 $cm^2V^{-1}s^{-1}$ and 10000 $cm^2V^{-1}s^{-1}$ respectively.

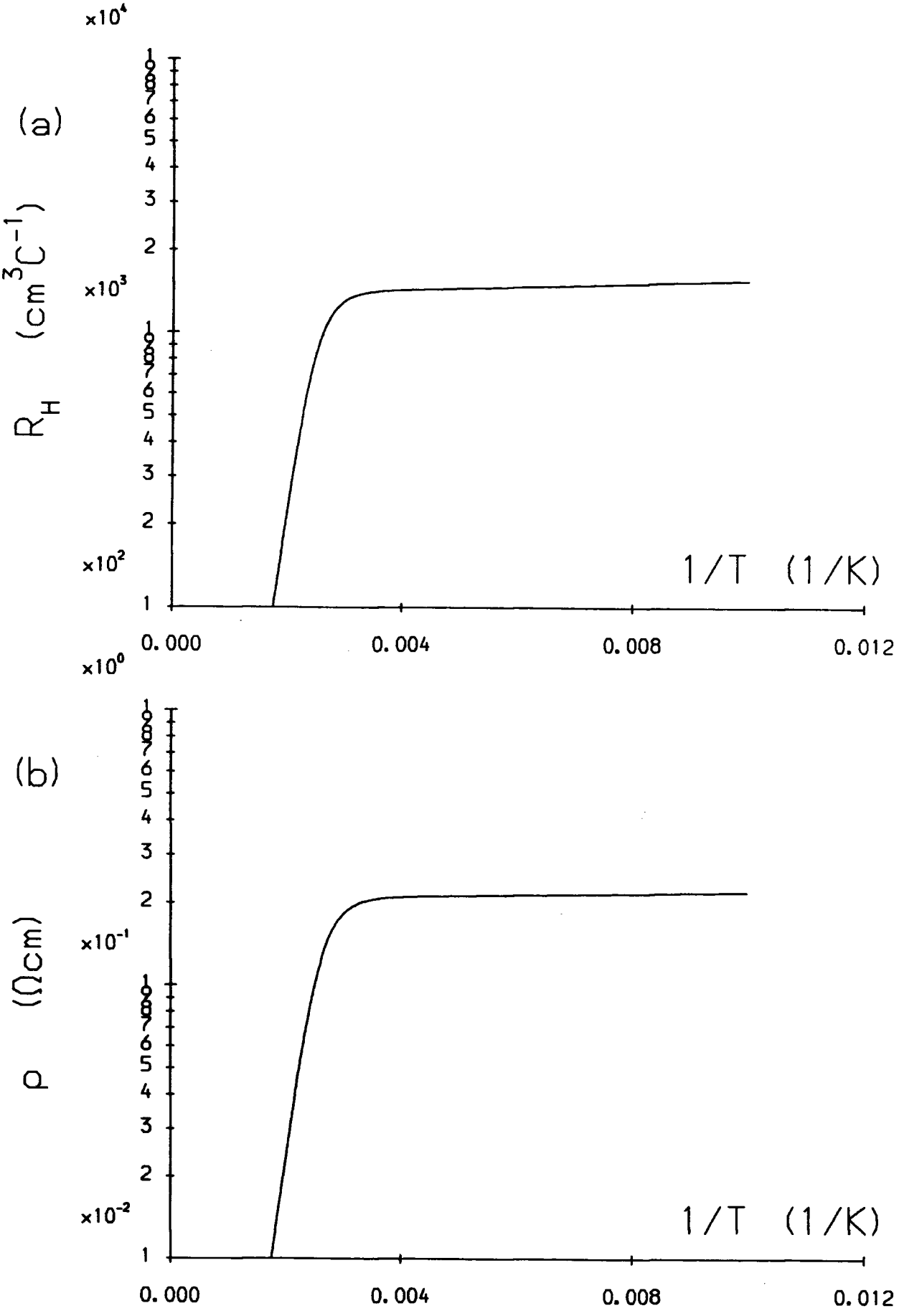

Fig. 4.6. Hall coefficient, R_H, and resistivity, ρ, for strongly inverted p-type $x = 0.3$ $Hg_{1-x}Cd_xTe$ with a uniform acceptor concentration of 1×10^{17} cm^{-3} and an effective inversion layer concentration of 2×10^{15} cm^{-3}. The hole and electron mobilities are 100 $cm^2V^{-1}s^{-1}$ and 10000 $cm^2V^{-1}s^{-1}$ respectively.

region of B will be 100 times greater than in A and accordingly the effective electron concentration will be increased by a factor of 50. As the temperature increases further, more electrons are generated and eventually the Hall coefficient crosses zero to become negative as the material becomes dominated by electrons. It can be seen from the two carrier Hall expression (4.27) that the crossover will occur when:

$$n_h \mu_h^2 = n_e \mu_e^2 \tag{4.40}$$

The sign of R_H is dependent on the square of the electron to hole mobility ratio and is therefore extremely sensitive to small concentrations of electrons. For case A, the crossover occurs at 245 K while for case B it is at the lower temperature of 193 K as expected from the preceding discussion. At the crossover temperatures, the resistivity, which depends on the mobilities rather than the square of the mobilities, is little changed from its low temperature value and is virtually solely dependent on conduction by holes. As the temperature increases beyond the crossover the magnitude of R_H increases reaching a maximum before falling as the material becomes intrinsic with R_H corresponding to the intrinsic electron concentration. In the intrinsic region, the resistivity, now controlled by intrinsic electrons, falls as sharply as R_H. By differentiating the two carrier Hall expression with respect to n_e and setting equal to zero, the condition for the maximum in $|R_H|$ is determined to be:

$$n_h \mu_h = n_e \mu_e \tag{4.41}$$

and the value of $|R_H|$ is given by:

$$|R_H| = \frac{1}{4qn_e} \tag{4.42}$$

Substituting for n_e in this expression using (4.41) yields:

$$|R_H| = \frac{1}{4} . \frac{\mu_e}{\mu_h} . \frac{1}{qn_h} \tag{4.43}$$

It can be seen that the ratio of the magnitude of the peak height to the value of R_H at low temperatures, $(\frac{1}{qn_h})$, is related to the ratio of the electron and hole mobilities.

N-type Material

Plots of $|R_H|$ and ρ for $x = 0.3$ $Hg_{1-x}Cd_xTe$ with a donor concentration of 1×10^{15} cm^{-3} are shown in Fig. 4.4. At low temperatures the material is extrinsic and R_H is negative and determined by the donor concentration as all donors are ionised at this dopant concentration. As the sample is heated intrinsic electrons become significant and $|R_H|$ falls and follows the curve expected for intrinsic $Hg_{1-x}Cd_xTe$ of this composition as found above for p-type material.

Weakly Inverted P-type Material

For the case of a p-type $Hg_{1-x}Cd_xTe$ layer where surface inversion gives rise to an effective electron concentration of n_s where:

$$\mu_e^2 n_s > \mu_h^2 N_a^- \tag{4.44}$$

R_H will always be negative even at low temperatures where intrinsic electrons are not important. It can be seen though from the previous discussion of the differential of R_H with respect to n_e that if the further condition of:

$$\mu_e n_s < \mu_h N_a^- \tag{4.45}$$

applies at low temperature then a peak in $|R_H|$ will occur when this condition no longer holds as more carriers are generated by heating the sample. This is illustrated in Fig. 4.5 for two different values of n_s both of which satisfy (4.44) and (4.45). In this light inversion regime, the resistivity is almost unaffected by the inversion layer electrons and is given to a good approximation by:

$$\rho = \frac{1}{n_h q \mu_h} \tag{4.46}$$

Strongly Inverted P-type Material

For layers where:

$$\mu_e n_s > \mu_h N_a^- \tag{4.47}$$

at low temperature, no peak will occur in $|R_H|$ and the transport data will take the form of n-type material. This is illustrated in Fig. 4.6 for the case of a layer with acceptor doping of 1×10^{17} cm^{-3} and an effective inversion layer concentration of 2×10^{15} cm^{-3}. In this case inspection of the two carrier equations ((4.27) and (4.28)) shows that, if both electrons and holes contribute to conduction, neither the Hall coefficient nor the resistivity are simply related to the concentration and mobility of either kind of carrier.

REFERENCES

1. P.W. Kruse in Semiconductors and Semimetals **18** Ed. R.K. Willardson and A.C. Beer. (Academic Press, 1981) ch. 1.
2. L.F. Lou and W.H. Frye, J. Appl. Phys. **56** (1984) 2253.
3. D.E. Lacklison and P. Capper, Semicond. Sci. Technol. **2** (1987) 136.
4. M.C. Chen, J. Appl. Phys. **65** (1989) 1571.
5. R.A. Smith, Semiconductors, 2nd ed. (Cambridge University Press, 1978) ch. 4.
6. R.A. Smith, Semiconductors, 2nd ed. (Cambridge University Press, 1978) ch. 5.
7. R.L. Petritz, Phys. Rev. 11 (6) (1958) 1254.
8. S.M. Sze, Physics of Semiconductor Devices, 2nd ed. (Wiley, 1981) ch. 7.
9. J.B. Mullin and A. Royle, J. Phys. D: Appl. Phys. **17** (1984) L69.
10. F. Nasir, J. Singleton and R.J. Nicholas, Semicond. Sci. Technol. **3** (1988) 654.
11. G.L. Hansen and J.L. Schmit. J. Appl. Phys. **54** (1983) 1639.
12. G.L. Hansen, J.L. Schmit and T.N. Casselman. J. Appl. Phys. **53** (1982) 7099.
13. J.C. Brice in Properties of Cadmium Mercury Telluride, EMIS Datareviews Series No. 3 (1987) Ed. J.C. Brice and P. Capper.

5. Properties of Mercury Cadmium Telluride

5.1 Introduction

In this chapter the results of the optical and electrical characterisation of Durham grown $Hg_{1-x}Cd_xTe$ epitaxial layers are presented. As a precursor to this the structural properties of the $Hg_{1-x}Cd_xTe$ layers and their substrates are described in section 5.2. In section 5.3, the optical transmission spectra obtained from these layers are given along with their analysis to yield the layer thickness and optical absorption coefficient as a function of photon energy. The variation of the optical absorption coefficient with energy is then be used to determine the energy gap and composition of the samples. A discussion of mercury vacancies which control conduction in Durham grown $Hg_{1-x}Cd_xTe$ in the as grown state and a description of the low temperature annealing of one sample to reduce the concentration of these defects is presented in section 5.4. The electrical data obtained from the Durham grown samples together with that from one sample grown by the General Electric Company plc. are described in section 5.5. This information is interpreted using the multicarrier/multilayer model developed in chapter 4 to yield information on the doping concentrations and carrier mobilities in the samples. The results obtained from the optical and electrical characterisation are discussed in section 5.5 and conclusions are drawn.

The salient growth parameters for all of the $Hg_{1-x}Cd_xTe$ layers considered during the course of this work and an outline of the characterisation work performed on them are presented in Appendix I.

5.2 Substrates and Structural Properties

The room temperature lattice parameter, a_0, of $Hg_{1-x}Cd_xTe$ increases monotonically from 6.462 Å to 6.481 Å as x varies from 0 to 1[1] . The $x = 0.3$ $Hg_{1-x}Cd_xTe$ typically considered here has a lattice parameter of 6.468Å. From lattice matching considerations, CdTe and InSb ($a_0 = 6.479$Å)[2] provide suitable substrates for epitaxial growth. The mismatch between either of these materials and $x = 0.3$ MCT is approximately 0.2% . InSb would be the preferred choice as it is commercially available in the form of high quality polished wafers if it were not for its high conductivity and small energy gap of 0.165 eV[2] . These two factors would prevent in-plane transport or I.R. Transmission measurements from being made on $Hg_{1-x}Cd_xTe$ layers grown on

InSb. The small energy gap also prevents InSb from being used as a substrate for $Hg_{1-x}Cd_xTe$ based devices operating in the infra-red region of the spectrum as it is strongly absorbing itself at these wavelengths. Highly lattice mismatched substrates such as GaAs ($a_0 = 5.653$Å)[2] were ruled out for this work due to the requirement for the development of a process for buffer layer growth[3] . In view of the above discussion all Durham grown $Hg_{1-x}Cd_xTe$ layers described in this work were deposited onto semi-insulating CdTe substrates cut from boules prepared in this laboratory by a vapour phase technique[4] .

The quality of bulk grown CdTe is generally poor. Transmission Electron Microscopy (TEM) and etching studies performed on Durham material[5] have shown it to be composed of subgrains typically 150μm in size and to contain tellurium precipitates. Additionally twinning occurs frequently on {111} planes[6] . Fig. 5.1 shows a double crystal X-ray diffraction (DCXRD) rocking curve about the (333) reflection obtained* from a 0.8 mm^2 area of {111} oriented CdTe substrate material. Several broad peaks can be seen probably corresponding to subgrains of slightly different orientation. The total width of this spectrum is 350 seconds of arc or approximately 0.1° which is a measure of the misorientation of the subgrains. By comparison a perfect single crystal of CdTe would be expected to exhibit a rocking curve width of ~10 seconds of arc[7] . Large rocking curve widths are however often found for bulk-grown CdTe[7] .

The structure of MCT layers grown epitaxially on {111} oriented substrates is dependent on which of the two polar {111} substrate faces is used[8] i.e. whether the substrate surface is the {111}A Cd face or the $\{\bar{1}\bar{1}\bar{1}\}$B Te face[9] . Growth on the $\{\bar{1}\bar{1}\bar{1}\}$B plane yields layers of excellent morphology exhibiting a low density of facets but which are twinned. In this case, the twinning takes the form of islands of twinned material in an untwinned matrix. MCT layers grown on the {111}A plane are of poor morphology with a highly faulted defect structure[10] . In this case both a twin and matrix structure and lamella twins lying parallel to the substrate are observed.

For growth on {100} planes, no twinning occurs in the MCT itself[11] . However {100} planes intersect the {111} twinning planes of CdTe and so twins propagate through from the substrate into the epitaxial layer. The morphology of {100} oriented layers is poorer than found for layers grown on the$\{\bar{1}\bar{1}\bar{1}\}$B plane with a high density

* A. Turnbull, Solid State Physics Group, Department of Physics, University of Durham.

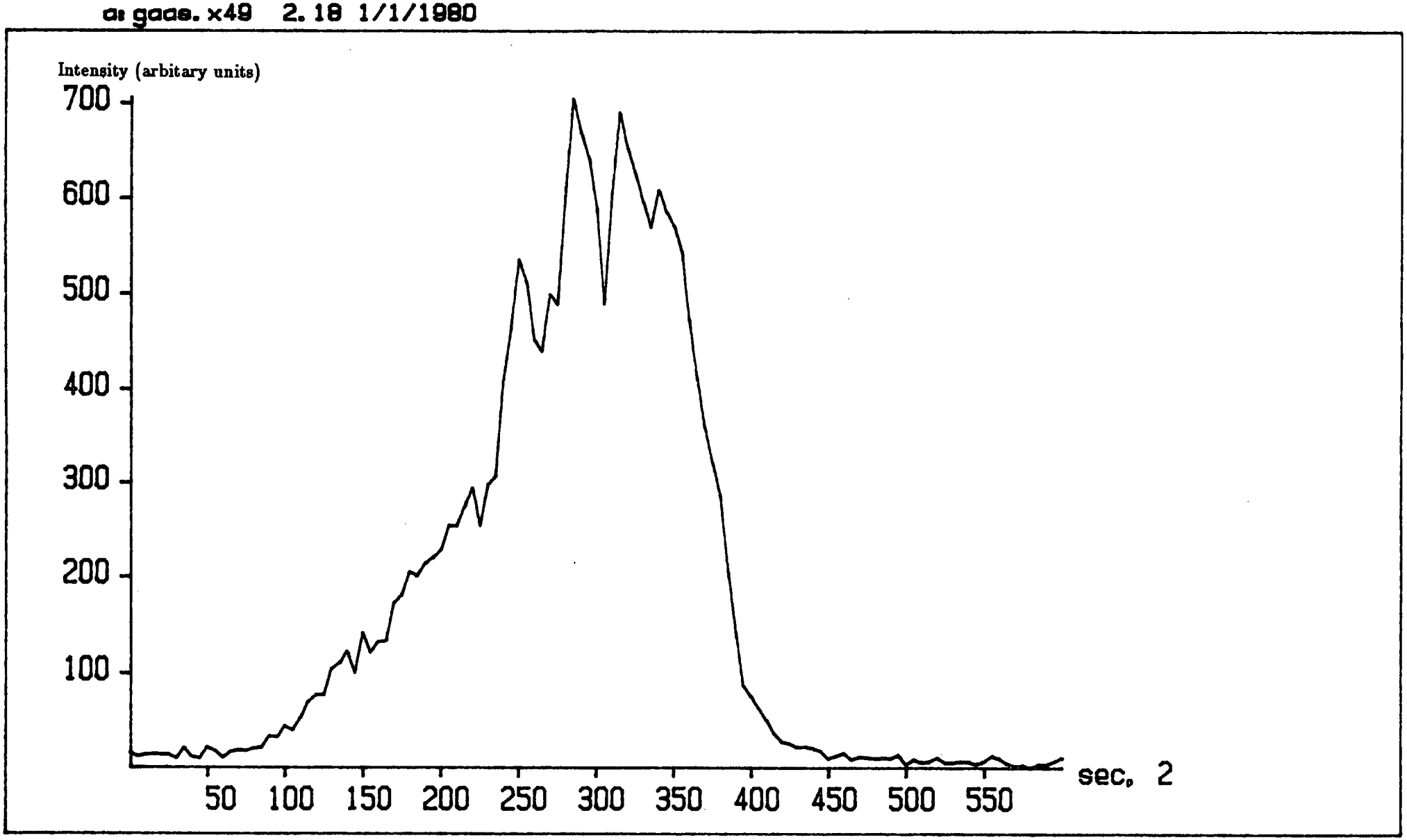

Fig. 5.1 DCXRD rocking curve about the (333) reflection from {111}B orientated CdTe substrate material.

of pyramidal surface facets. It is believed that growth rates are enhanced on the low energy {111} planes and that this leads to the development of facets during growth on the {100}. This is supported by the observation that the facet sides lie parallel to {111} directions.

As the presence of twins in MCT layers grown on either {100} or $\{\bar{1}\bar{1}\bar{1}\}$B oriented CdTe is unavoidable, it was decided to grow layers of MCT for optical and electrical characterisation on $\{\bar{1}\bar{1}\bar{1}\}$B CdTe as this produced the best morphology. Morphology was considered important as the presence of facets has been shown to be detrimental to the fabrication and subsequent performance of infra-red photodiodes fabricated from $Hg_{1-x}Cd_xTe$[12] . A further advantage of {111} oriented material was that twin bands were often visible at the outside of CdTe boules permitting easy identification of suitable grains and subsequent initial alignment prior to cutting. Determination of the A and B faces of {111} CdTe and substrate preparation prior to growth are described in chapter 2.

5.3 Optical Properties

Transmittance Spectra

The 300K infra-red transmittance spectra obtained from four of the Durham grown $Hg_{1-x}Cd_xTe$ samples considered in this thesis are shown in Figs. 5.2(a) to 5.5(a). These spectra were taken with the samples in their as grown state. For samples MCT37, MCT77 and MCT78 two spectra are shown. These correspond to two different regions of the sample and so provide a measure of the compositional uniformity of the sample.

The spectra exhibit a region of low transmission corresponding to photon energies greater than the fundamental gap of the $Hg_{1-x}Cd_xTe$ where strong absorption occurs. As the incident light energy falls in the region of the energy gap, there is a rise in transmittance as absorption in the semiconductor falls. At lower photon energies, the transmittance reaches a maximum where there is negligible absorption in the semiconductor and the only losses are due to reflection and scattering at the air/sample interface caused by the refractive index change and surface roughness. Interference fringes are also observed in this region due to the thin film nature of the $Hg_{1-x}Cd_xTe$. The spacing of these fringes is dependent on the thickness and refractive index of the layer.

In principle therefore, these spectra contain information on the variation of the

optical absorption coefficient with energy, the thickness and the refractive index of the samples being considered.

It can be seen that for MCT77 and MCT78 the two spectra obtained overlap indicating that the composition of these samples is highly uniform across the sample area. For MCT37, however, there is a considerable difference between the two traces indicating significant compositional non-uniformity. In the analysis of the transmission data for this sample, presented in the following sections, the two spectra have been used to determine the optical properties of both regions of this sample.

Interpretation of the Transmittance Spectra

Following the analysis of Finkman and Nemirovsky[13] , the optical absorption coefficient, α, may be determined from the transmittance, T_r, and the layer thickness, d, using the following expression:

$$T_r = \frac{(1-R)^2.e^{-\alpha d}}{1-R^2.e^{-2\alpha d}} \tag{5.1}$$

where R may be determined from the refractive index, n, according to:

$$R = \left(\frac{n-1}{n+1}\right)^2 \tag{5.2}$$

In the limit of no absorption (5.1) reduces to:

$$T_{max} = \frac{(1-R)^2}{1-R^2} \tag{5.3}$$

For the case of no scattering, T_{max} may be used to find R and hence n.

With n known, the film thickness, d, can be found from:

$$d = \frac{1}{2.n.\Delta K} \tag{5.4}$$

where ΔK is the interference fringe spacing measured in units of wavenumber. This value of d together with R determined from either the refractive index or the maximum transmission may be used in (5.1) to find α as a function of energy if the approximation of a constant refractive index is made.

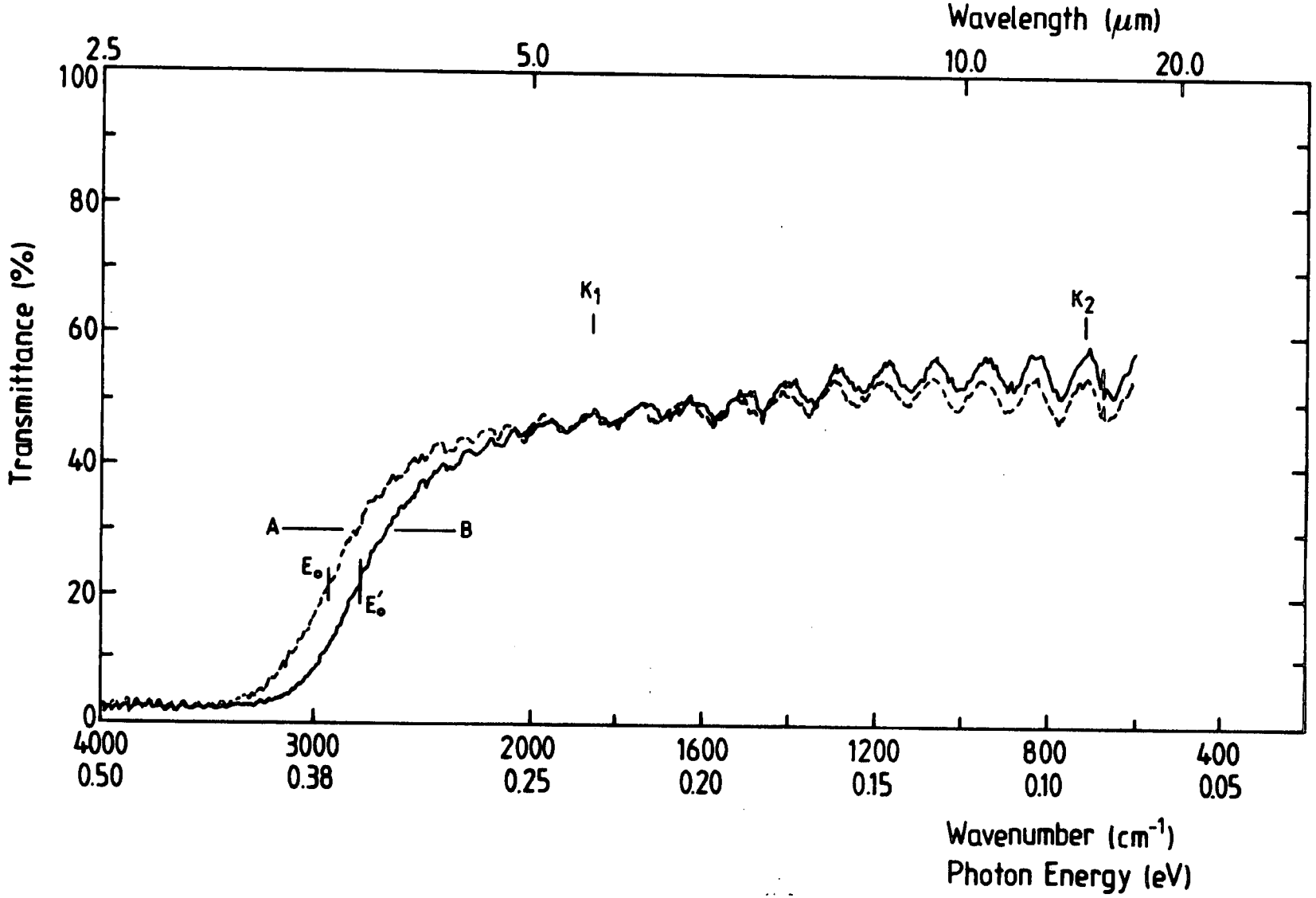

Fig. 5.2(a) Infra-red transmission spectrum obtained from MCT37.

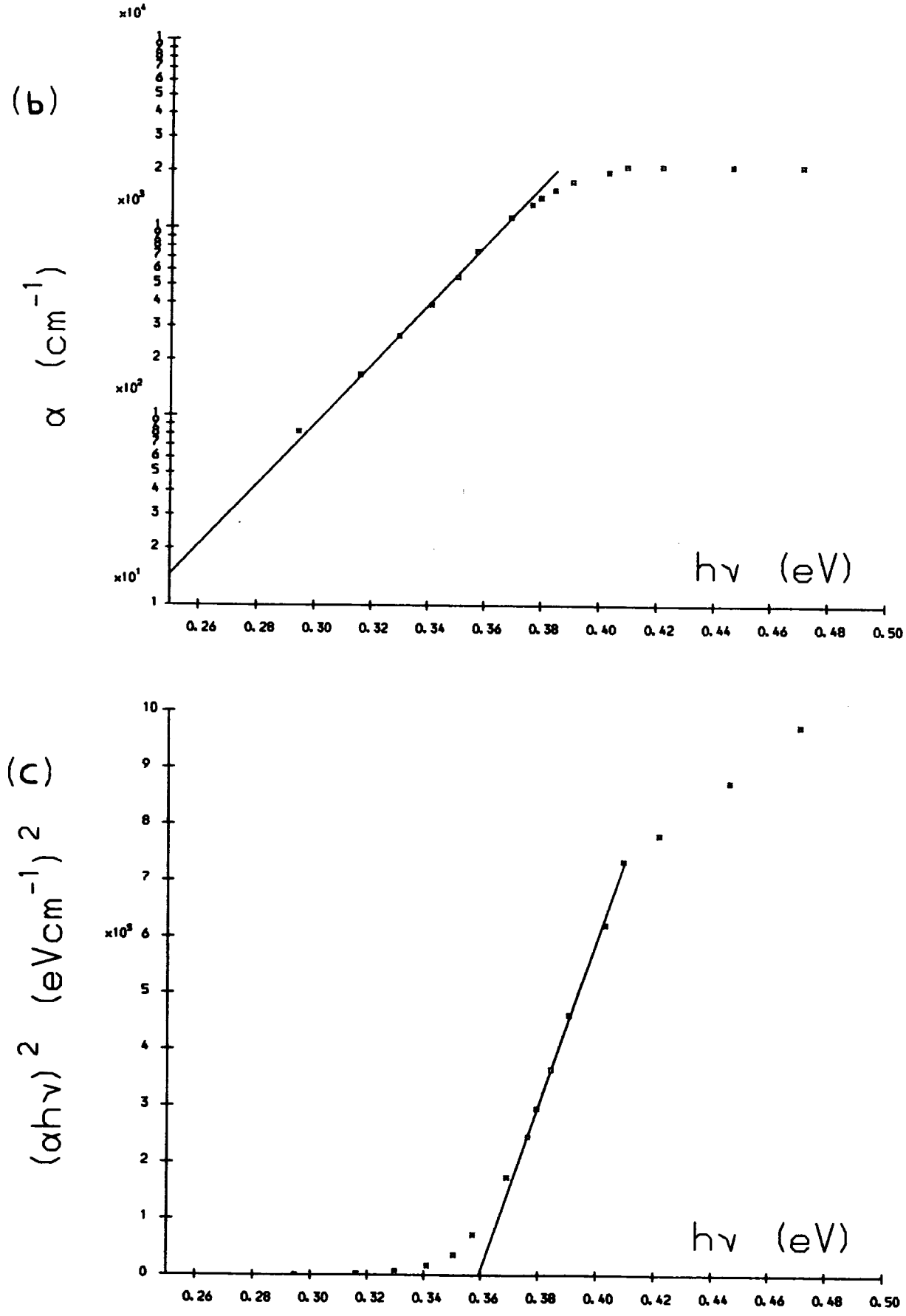

Fig. 5.2(b) Absorption coefficient (α) versus photon energy ($h\nu$) and (c) $(\alpha h\nu)^2$ versus ($h\nu$) for MCT37.

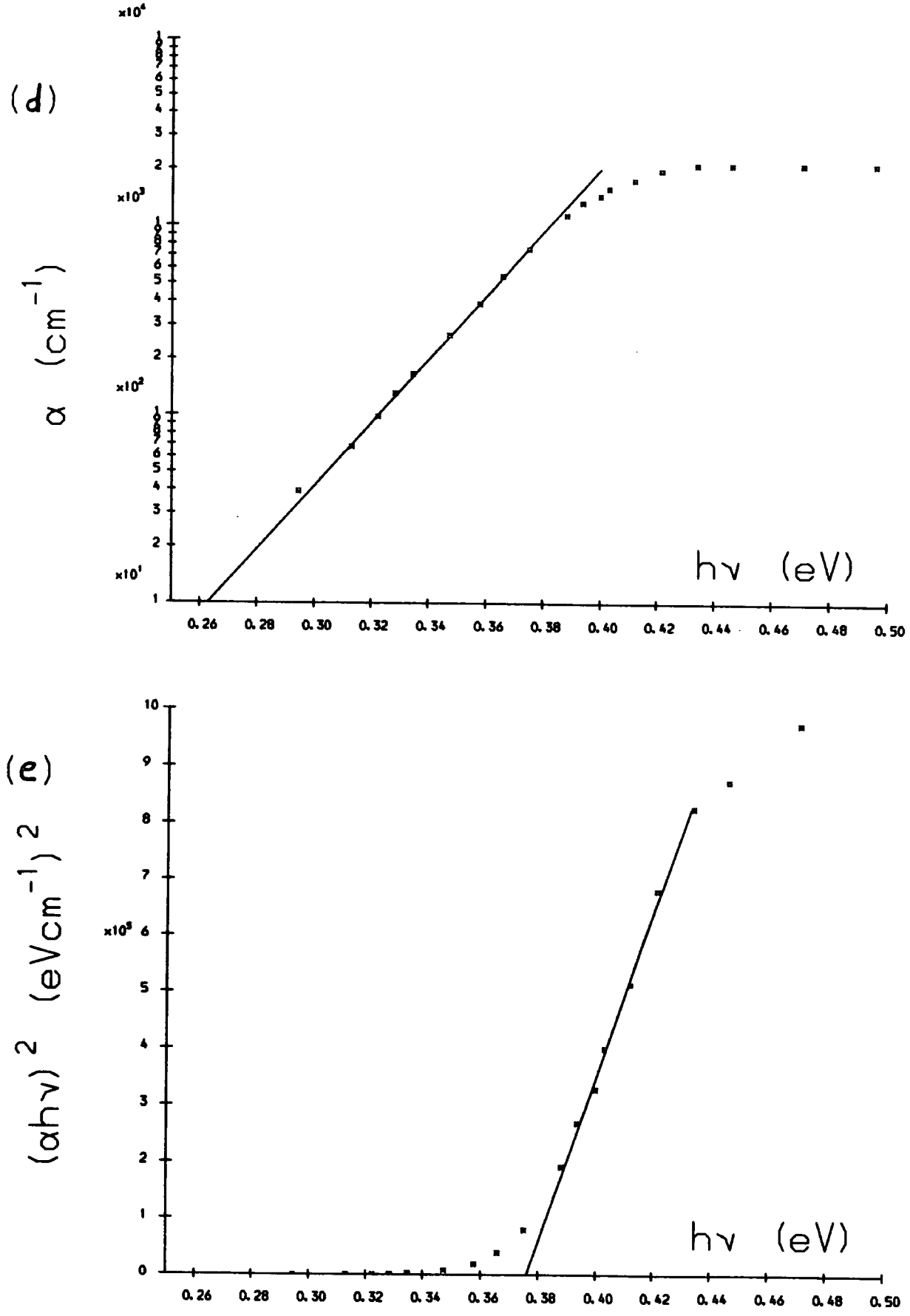

Fig. 5.2(d) Absorption coefficient (α) versus photon energy ($h\nu$) and (e) $(\alpha h\nu)^2$ versus ($h\nu$) for a second region of MCT37.

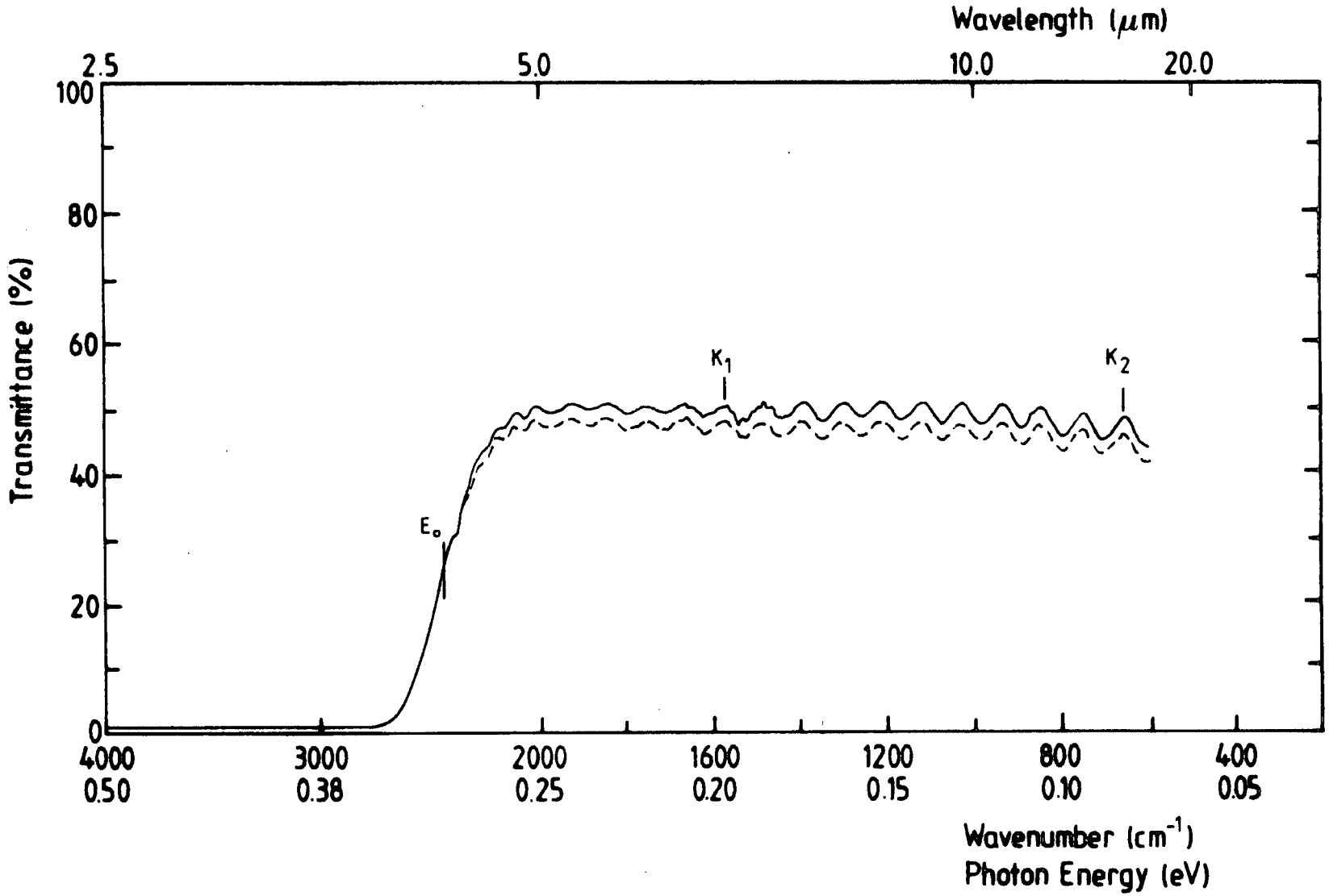

Fig. 5.3(a) Infra-red transmission spectrum obtained from MCT77.

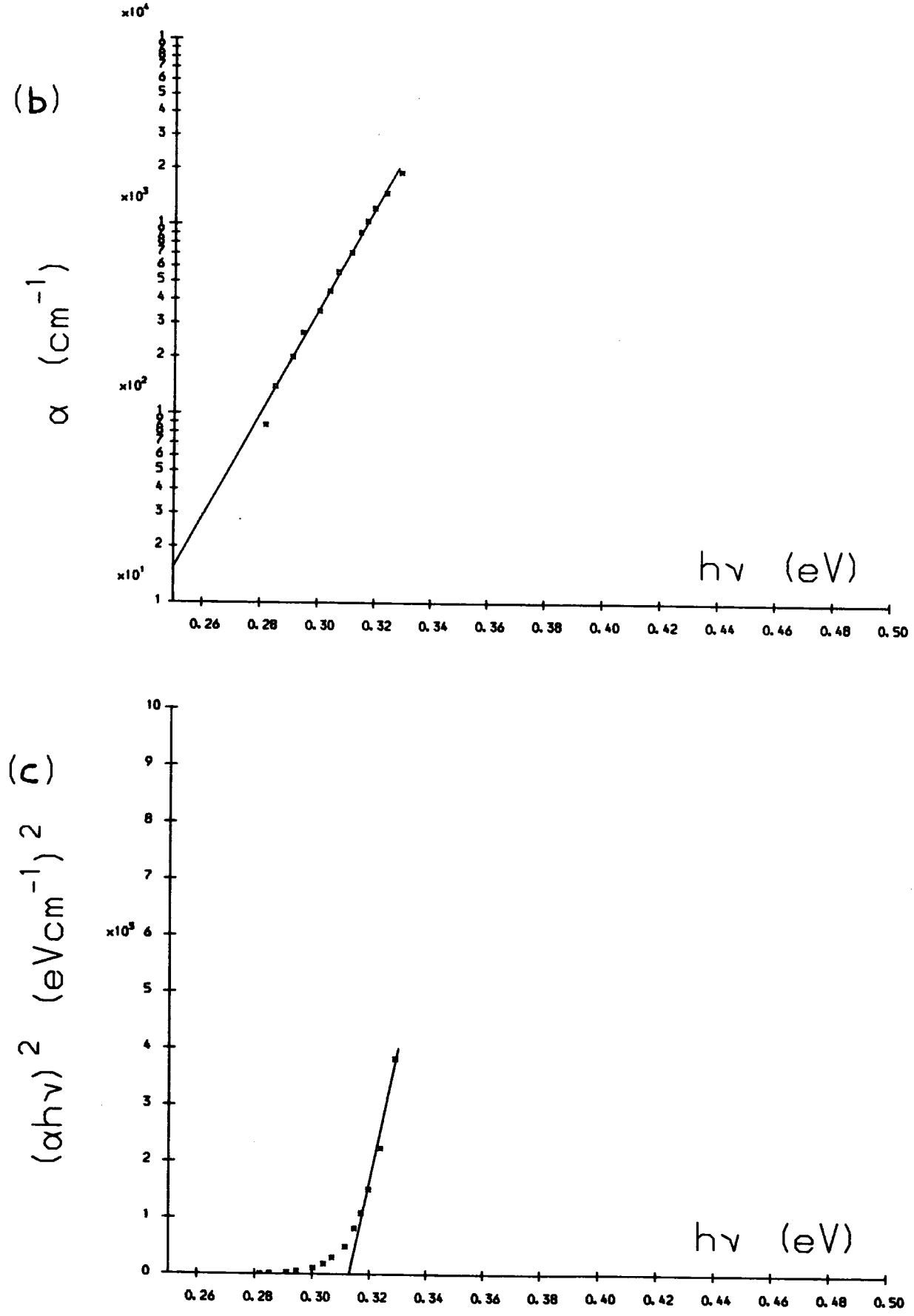

Fig. 5.3(b) Absorption coefficient (α) versus photon energy ($h\nu$) and (c) $(\alpha h\nu)^2$ versus ($h\nu$) for MCT77.

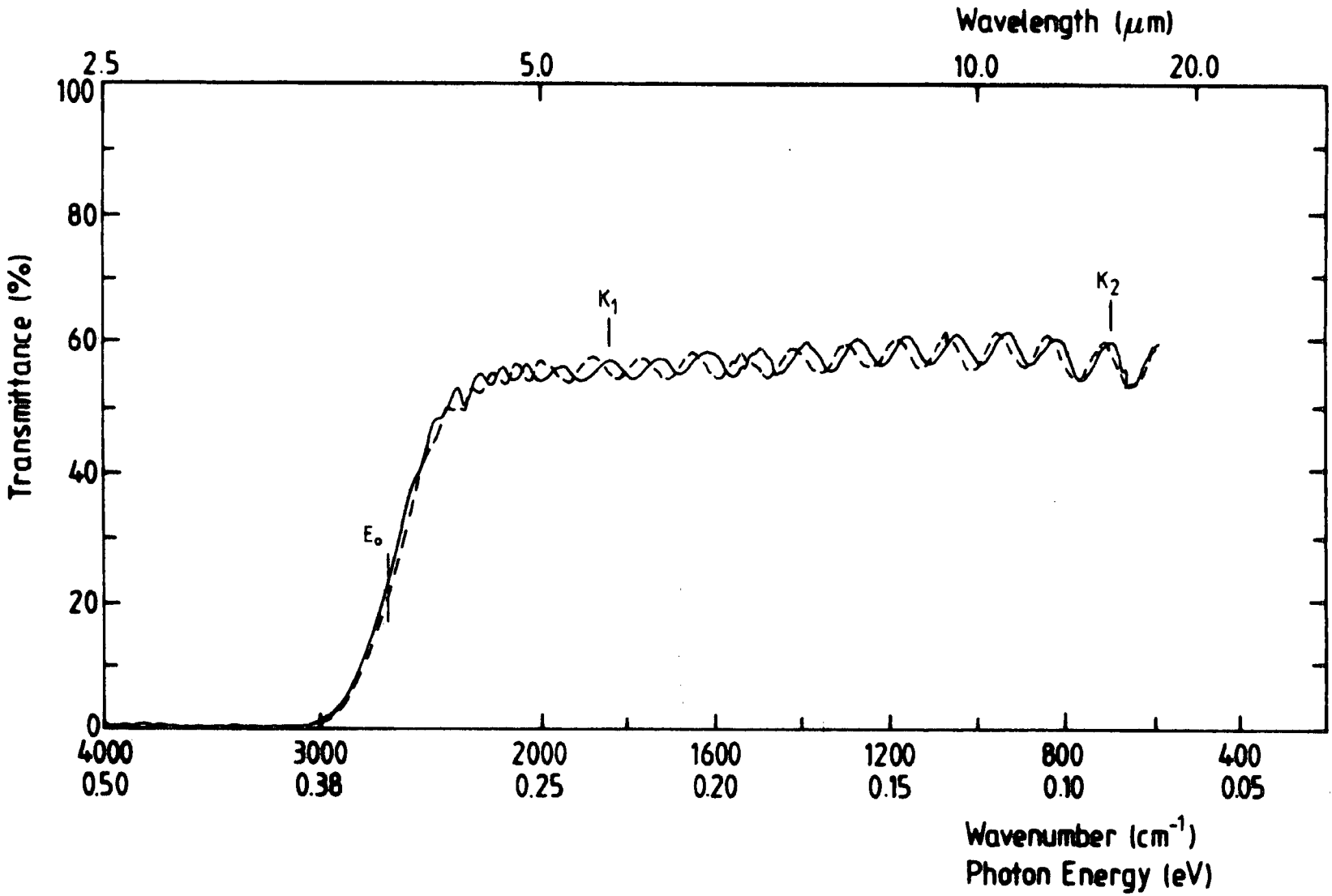

Fig. 5.4(a) Infra-red transmission spectrum obtained from MCT78.

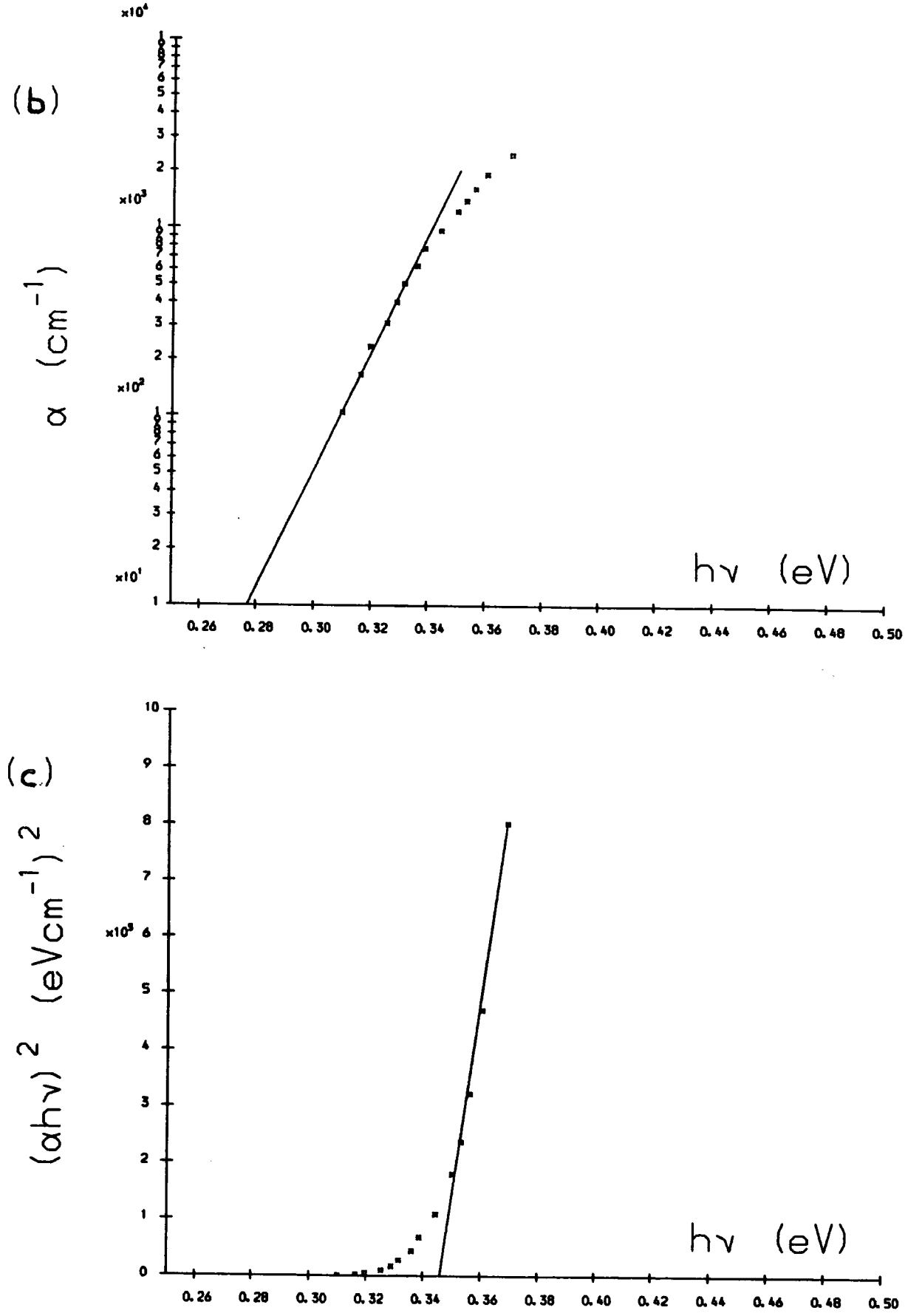

Fig. 5.4(b) Absorption coefficient (α) versus photon energy ($h\nu$) and (c) $(\alpha h\nu)^2$ versus ($h\nu$) for MCT78.

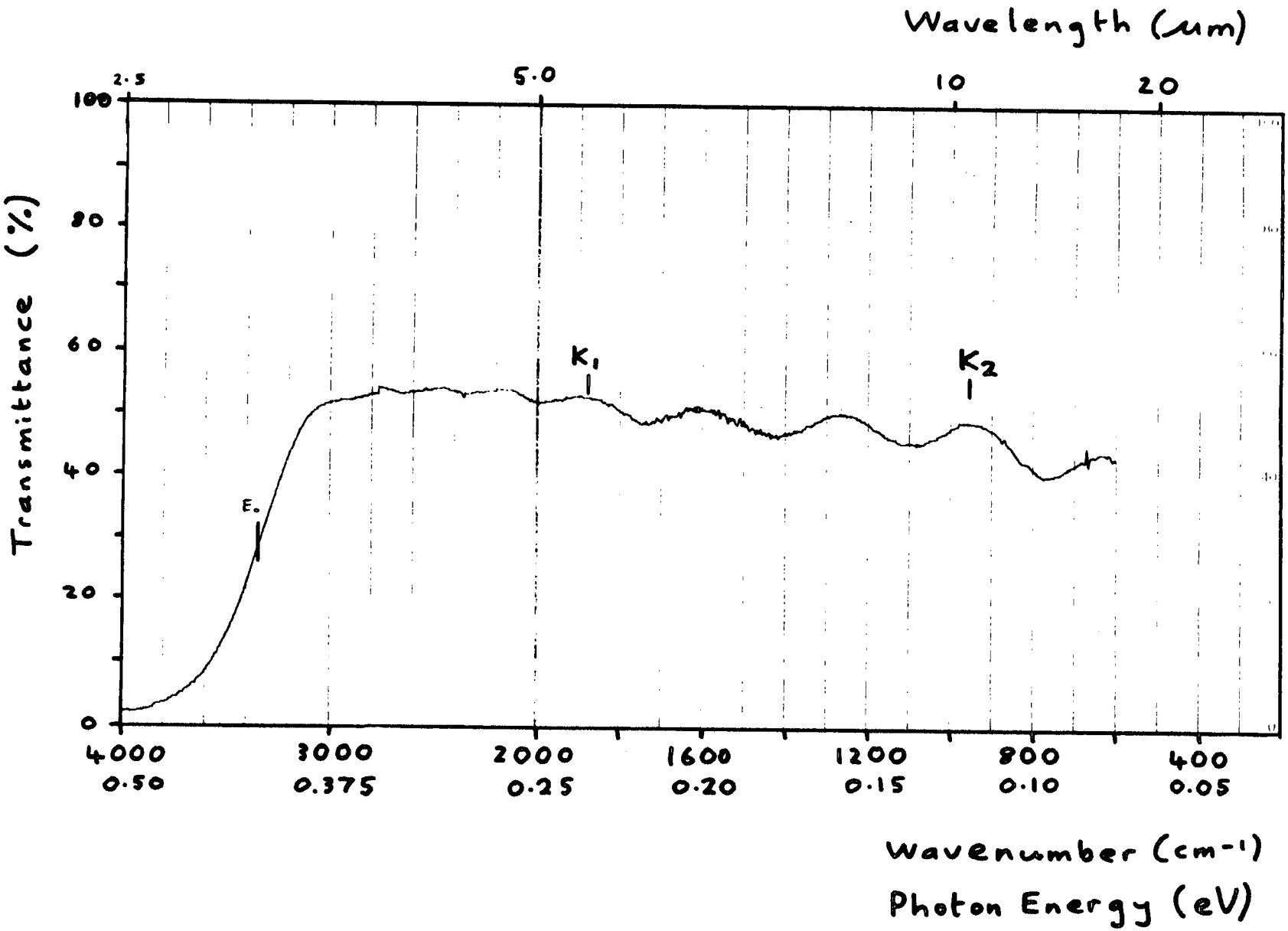

Fig. 5.5(a) Infra-red transmission spectrum obtained from MCT86.

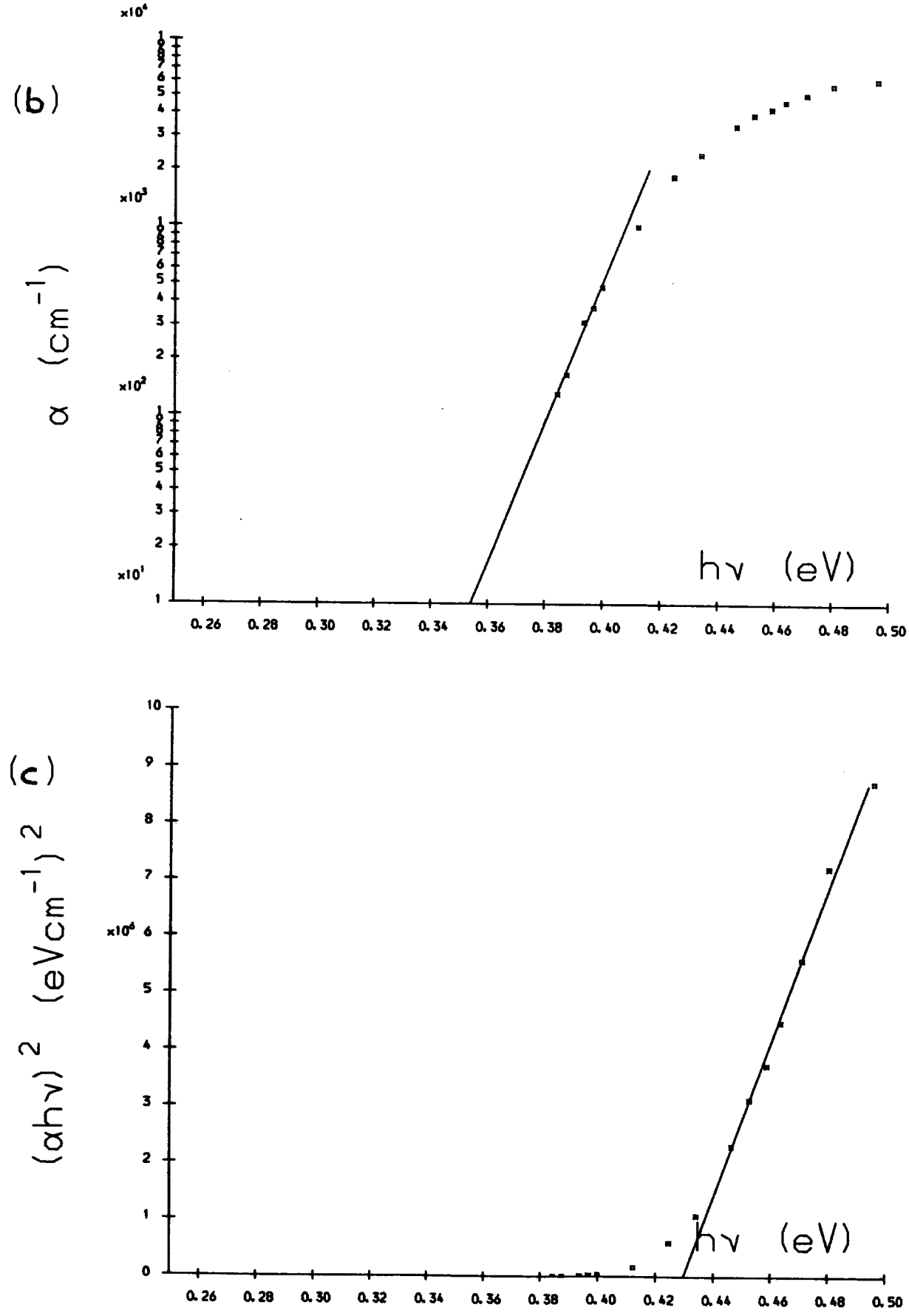

Fig. 5.5(b) Absorption coefficient (α) versus photon energy ($h\nu$) and (c) $(\alpha h\nu)^2$ versus ($h\nu$) for MCT86.

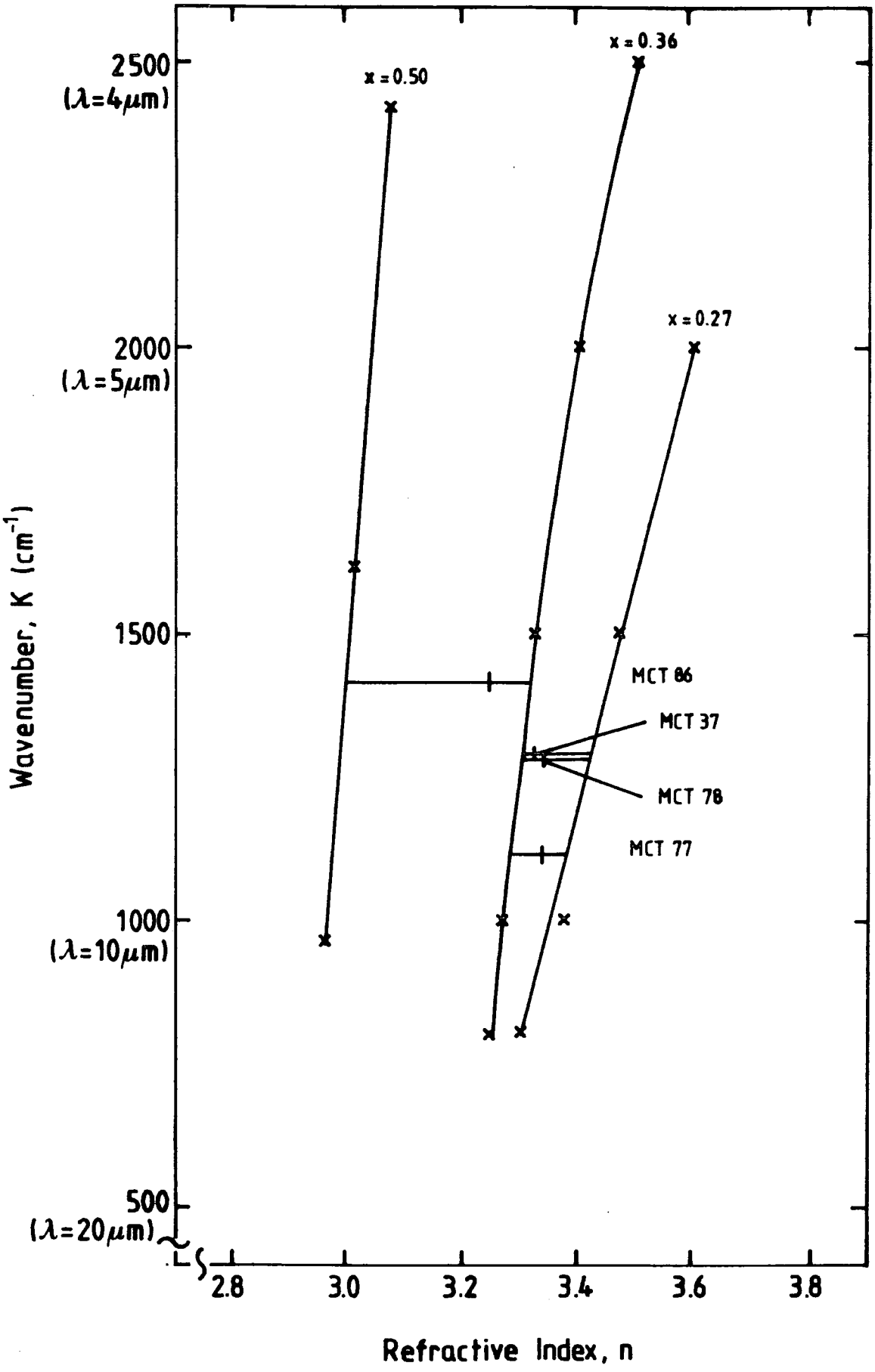

Fig. 5.6 Refractive index as a function of wavenumber and composition for $Hg_{1-x}Cd_xTe$. After Brice[1] . The vertical bars give the refractive indices of the samples considered in this thesis.

	MCT37	MCT77	MCT78	MCT86
E_0 (eV)	0.363 : 0.344	0.301	0.329	0.416
x from E_0	0.35 : 0.34	0.31	0.33	0.39
K_1 (cm^{-1})	1860	1570	1845	1880
K_2 (cm^{-1})	720	660	710	950
ΔK (cm^{-1})	114	91	113	310
n	3.32	3.34	3.34	3.24
d (μm)	13.2	16.5	13.2	5.0
T_{max}	0.46	0.50	0.54	0.54
β	38.8 : 36.6	62.7	70.9	85.7
E_g ($\alpha = 1000$) (eV)	0.382 : 0.366	0.317	0.342	0.408
E_{100} ($\alpha = 100$) (eV)	0.322 : 0.303	0.280	0.304	0.381
E_g (parabolic) (eV)	0.376 : 0.359	0.313	0.346	0.430
x from E_g	0.36 : 0.35	0.32	0.34	0.40

Table 5.1 Summary of optical properties and composition

Inspection of the transmittance spectra shows that the maximum transmittance varies from sample to sample and for different parts of the same sample. This cannot be accounted for by refractive index changes and is assumed to be due to the additional effect of scattering from the sample surface. Thus T_{max} cannot be used to determine n for the samples considered here. In view of this, a value for the refractive index was determined from previously published data and this value was then used for the calculation of d and hence α as described below.

Brice[1] has tabulated values of refractive index for MCT as a function of composition and photon energy. Data covering the range of x and wavenumber of interest here are plotted in Fig. 5.6. In order to determine n, an estimate was first made of the energy gap of the layer by taking the energy corresponding to half maximum transmittance. This is marked E_0 on the transmittance spectra. The empirical expression of Hansen, Schmit and Casselman, relating energy gap and composition, was then used to find a value for x. A series of fringes marked by K_1 and K_2 were selected and used to determine an average value of the fringe spacing ΔK. A linear interpolation of the data of Fig. 5.6 using the estimated value of x and the average of K_1 and K_2 then gave an estimate for n. This value of n was then used to find d. The optical absorption coefficient could then be calculated using this value of d together with R as determined from T_{max} (5.3). In this way, allowance was made for scattering losses which would otherwise have affected the determination of α particularly in the low absorption region.

The Exponential Band Tail

The optical absorption coefficient as calculated from the transmittance data is plotted as a function of photon energy in Figs. 5.2(b) to 5.5(b) and Fig.5.2(d) which gives the result of this calculation for the second spectrum obtained from MCT37. It can be seen that for values up to $\sim$ 1000 cm^{-1}, α has an exponential dependence on energy. This is attributed to band tailing and is generally observed in $Hg_{1-x}Cd_xTe$. The data may be fitted to the empirical expression of Urbach[14] :

$$\alpha = \alpha_0 exp\Big(\frac{\sigma}{T}(h\nu - \epsilon)\Big) \tag{5.5}$$

where α_0, σ and ϵ are constants and T and $h\nu$ are the temperature and photon energy respectively. At constant temperature, this may be expressed as:

$$\alpha = \alpha_0 exp\Big(\beta(h\nu - \epsilon)\Big) \tag{5.6}$$

here β is the gradient of a plot of $ln(\alpha)$ against $h\nu$.

A least squares fit to the exponential portion of the curves yields the gradients, β, which lie in the range 36-86 eV^{-1} (Table 5.1). Finkman and Nemirovsky[13] derived an empirical expression for the variation of α with x, wavenumber and temperature for $Hg_{1-x}Cd_xTe$ from the results of transmittance measurements made on bulk grown material. They found a gradient of 120 eV^{-1} independent of x for $0.205 < x < 0.220$ at 300K. Their material was n-type with a donor concentration of $\sim 10^{15}$ cm^{-3}. Mroczkowski et al[15] found that β increased from 105 eV^{-1} to 148 eV^{-1} as their $x = 0.3$ material was annealed in mercury vapour and the carrier concentration changed from 2×10^{16} p-type to 6×10^{14} n-type. They attributed the band tailing to defects associated with mercury vacancies. Finkman and Schacham[16] found B to be 111 eV^{-1} at 300 K for $x = 0.29$ $Hg_{1-x}Cd_xTe$ and also suggested that this was a limiting upper value for β due to the intrinsic properties of $Hg_{1-x}Cd_xTe$ rather than any defects or inhomogeneities. Whatever the cause of this band tailing, for values less than $\sim$ 100 eV^{-1} the gradient, β, may be taken as a measure of the quality of the sample as it is inversely related to the depth to which extra defect states penetrate into the forbidden gap. It can be seen from Table 5.1 that the magnitude of β for Durham grown material increased for each successive growth run considered with the last sample to be grown (the capped sample MCT86) having $\beta = 86$ eV^{-1}. This indicates steadily improving quality as the growth process was refined. The earliest sample considered (MCT37) was shown above to be laterally non-uniform and this explains the low value of β. The exact reason for the improvement in the later samples is not clear. The concentration of mercury vacancies in MCT77 and presumably MCT78 in its as grown state $Hg_{1-x}Cd_xTe$ is higher than in the capped sample MCT86 ($\sim 10^{19}$ instead of $\sim 10^{18}$ see section 5.4) which may explain some of the improvement. The fact that the later layers were grown at slightly lower temperatures (395°C instead of 410°C) suggests that incomplete interdiffusion of the constituent IMP layers was not a significant factor in the band tailing.

Energy Gap and Composition

For values greater than $\sim$ 1000 cm^{-1}, the absorption coefficient exhibits a parabolic dependance on photon energy, $h\nu$, of the form:

$$\alpha = C\sqrt{(h\nu - E_g)} \tag{5.7}$$

as expected for a semiconductor with a direct energy gap of E_g and parabolic bands[17] . Here C is a constant. The value of $\alpha \sim 1000$ cm^{-1} marking the onset of parabolic absorption is consistent with that found by Chu et al[18] who performed transmission measurements on $Hg_{1-x}Cd_xTe$ samples which had been thinned to allow measurements to be made up to $\alpha \sim 10000$ cm^{-1}. Figs. 5.1(c) to 5.4(c) and 5.2(e) show plots of $(\alpha h\nu)^2$ against $h\nu$. Extrapolation of the high absorption straight line portions of these curves to $(\alpha h\nu)^2 = 0$ gives a value for the parabolic energy gap of the material.

Parameters obtained from the optical data on the four samples considered are presented in Table 5.1. The energy gap as determined from the above consideration of the parabolic absorption is close to that obtained from the $\alpha = 1000$ cm^{-1} point as assumed by Hansen Schmit and Casselman[19] . Furthermore both energies are also close to the energy of the half maximum transmission point which was used previously to determine the composition and hence refractive index for the determination of layer thickness. In view of the weak dependence of n on composition (Fig. 5.6), this approximation in the determination of d is justified. The photon energy corresponding to $\alpha = 100$ cm^{-1} can be taken as the onset of optical absorption. For the samples considered here, this energy lies approximately 40 meV below the parabolic energy gap. This is a measure of the depth to which the exponential band tail penetrates the forbidden gap. The composition of the samples was determined from the energy corresponding to the $\alpha = 1000$ cm^{-1} point on the absorption spectra using the empirical expression on Finkman and Nemirovsky[13] who measured the optical absorption in $Hg_{1-x}Cd_xTe$ samples of known composition.

5.4 Mercury Vacancies in $Hg_{1-x}Cd_xTe$

The Hg-Te bond is weak[20] and furthermore, the presence of Cd in the $Hg_{1-x}Cd_xTe$ lattice has the effect of making it weaker[21] . Accordingly, the vapour pressure of mercury above $Hg_{1-x}Cd_xTe$ is relatively high and so mercury may be easily lost leading to the presence of Hg vacancies in this material. These mercury vacancies are assumed act as doubly ionised acceptors[22] and are often used as such in work on $Hg_{1-x}Cd_xTe$.

During growth, the Hg vacancy concentration, V_{Hg}, is determined by the growth temperature and the mercury vapour pressure, P_{Hg}, in the growth system. In the case of growth by MOVPE as described in chapter 2, the growth temperature is determined by the susceptor temperature and P_{Hg} by the temperature of the mercury boat. Yang et al.[23] give the following mass action laws for $Hg_{1-x}Cd_xTe$ relating the electron concentration, n_e, the hole concentration n_h, V_{Hg} and P_{Hg}:

$$V_{Hg}n_h^2P_{Hg} = K_v \tag{5.8}$$

$$n_en_h = K_i \tag{5.9}$$

where K_v and K_i are constants for any particular temperature. From the results of annealing experiments carried out as a function of mercury vapour pressure on bulk grown $x = 0.2$ $Hg_{1-x}Cd_xTe$ over the temperature range 430°C to 600 °C and subsequent electrical characterisation they determined K_v and K_i to be given by the following expressions:

$$K_i = 2.7 \times 10^{29}T^3exp\Big(\frac{-0.23\text{eV}}{kT}\Big)(\text{cm}^{-6}) \tag{5.10}$$

$$K_v = 7.3 \times 10^{58}T^3exp\Big(\frac{-2.07\text{eV}}{kT}\Big)(\text{cm}^{-9}\text{atm}) \tag{5.11}$$

They also give a high temperature charge neutrality condition:

$$n_e + 2.V_{Hg} = n_h \tag{5.12}$$

which assumes that there is a one to one correspondence between mercury vacancies and doubly ionised acceptors.

Substituting (5.8) and (5.9) into (5.12) yields the following expression relating V_{Hg} and P_{Hg}:

$$P_{Hg} = \frac{-2.V_{Hg}\sqrt{\frac{V_{Hg}}{K_v}} + \sqrt{\frac{4.V_{Hg}^3/K_v + 4.K_i V_{Hg}}{K_v}}}{\frac{2.K_i V_{Hg}}{K_v}} \tag{5.13}$$

Yang and coworkers assumed that the vacancy concentration existing in the sample during growth or annealing was frozen in on cool down, and gives rise to an effective acceptor concentration, Na:

$$Na = 2.V_{Hg} \tag{5.14}$$

where the factor of 2 accounts for the doubly ionised character assumed for mercury vacancies.

Assuming that this theory and the expressions for K_i and K_v hold at temperatures lower than those investigated by Yang et al. and that they provide a first approximation for material of composition other than $x = 0.2$ then it is possible to use (5.13) and (5.14) to predict the mercury vacancy concentration and, by implication, the acceptor concentration in the MOVPE grown $Hg_{1-x}Cd_xTe$ samples described in this chapter. Fig. 5.7 gives the results of such a calculation for growth temperatures in the region of 395°C. It can be seen that, for a mercury vapour pressure of 0.026 atm (20 Torr) which corresponds[24] to a mercury temperature of 205°C, as used in this work, the expected acceptor concentration is of the order of 10^{17} cm^{-3}.

One sample (MCT78) was annealed at a temperature much lower than that of the growth under almost saturated mercury vapour pressure in order to reduce the mercury vacancy concentration. This treatment has been shown[25] to reveal the presence of residual donors in $Hg_{1-x}Cd_xTe$ and so may be used as a means of converting the material to n-type. The as grown layer was placed into a quartz ampoule together with a small quantity of mercury as shown in Fig. 5.8. This was then evacuated and sealed under vacuum prior to being placed in a vertical two-zone furnace which had been set to give the temperature profile shown in the figure. The ampoule was sufficiently long to ensure that the sample and mercury charge remained cool during the sealing process. The mercury vapour pressure was determined by the temperature of the mercury which was at the coolest part of the ampoule to prevent unwanted condensation of the mercury. The mercury temperature was taken to be the average of the temperatures at the top

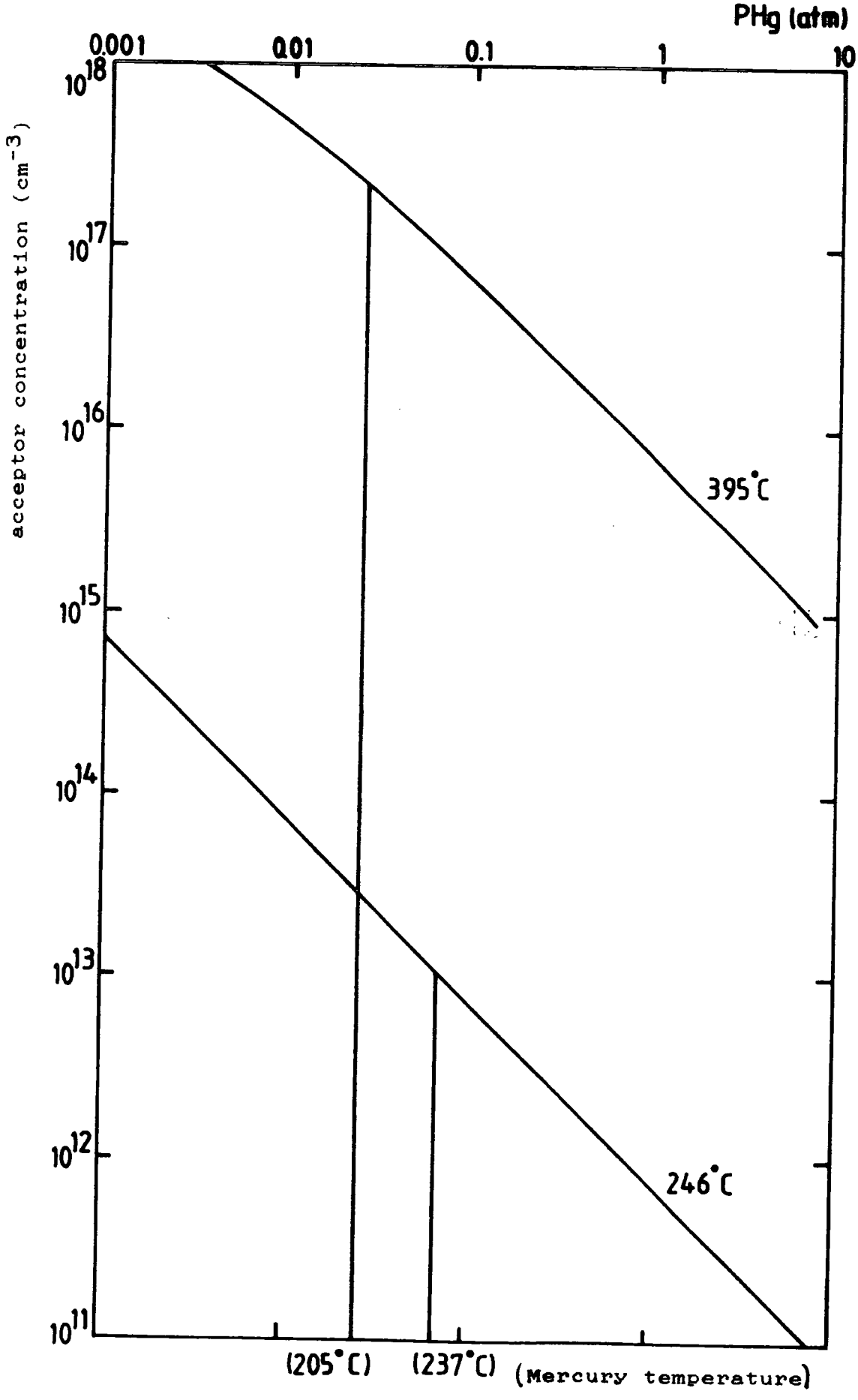

Fig. 5.7 Acceptor concentration due to mercury vacancies as a function of temperature and mercury vapour pressure for $x = 0.2$ $Hg_{1-x}Cd_xTe$. After Yang et al[24].

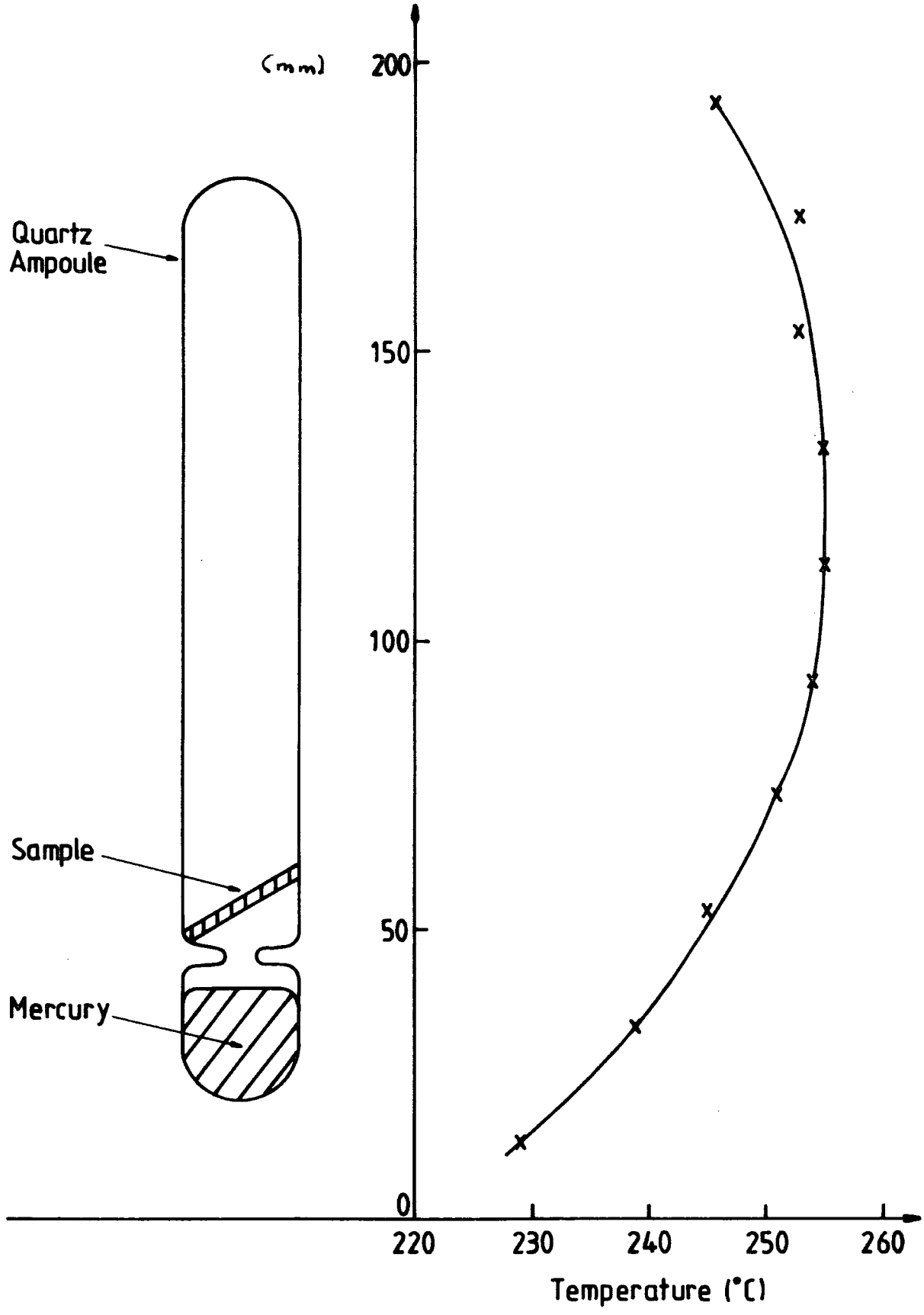

Fig. 5.8 Ampoule and furnace temperature profile used for annealing $Hg_{1-x}Cd_xTe$.

and bottom of the mercury charge and the sample temperature was likewise assumed to be the average temperature in the region occupied by the sample. Thus the mercury temperature was 237°C giving a mercury vapour pressure of 46 Torr[24] and the sample temperature was 246°C . Annealing was carried out for 2 days to ensure equilibrium after which the furnace was switched off and allowed to cool. From Fig. 5.7 it can be seen that such treatment may be expected to reduce the effective acceptor concentration in $Hg_{1-x}Cd_xTe$ to the region of 10^{13} cm^{-3}.

5.5 Electrical Transport

Plots of the Hall coefficient, R_H, and resistivity, ρ, versus inverse temperature, $1/T$, for the four $Hg_{1-x}Cd_xTe$ layers considered in the optical section above together with two further samples (MCT71 and GEC630) for which it was not possible to obtain IR transmission data are shown in Figs. 5.9 to 5.14. Sample GEC630 was grown (on a $\{\bar{1}\bar{1}\bar{1}\}$B oriented CdTe substrate) and contacted by the General Electric Company plc. who estimated the layer to be 10 μm thick with a composition of $x = 0.3$. MCT71 was grown at Durham and estimated to be 8 μm thick from cross sectional SEM measurements. Samples GEC630 and MCT37 were the first to be investigated and this work was performed using an early version of the Hall rig coldfinger which restricted the minimum measurement temperature to > 140K. The solid lines in the figures represent fits to the data made using the multicarrier/multilayer model for $Hg_{1-x}Cd_xTe$ described in chapter 4. In the case of samples MCT71, MCT77 and MCT78, account was also taken of the temperature dependence of mobilities and this is detailed for each sample in the following sections. A summary of the parameters relating to the electrical properties of these six layers is presented in Table 5.2.

P-type Material

The GEC sample (Fig. 5.9) exhibits a classical dependence of R_H on inverse temperature. R_H is positive at low temperatures, becomes negative at the crossover temperature of ~240 K then peaks before falling to approach the intrinsic line at the highest temperature of measurement (415 K). The energy gap and hence composition of this layer was determined from the slope of R_H in this intrinsic region using equation (4.10) Use of the multicarrier model assuming only a uniform acceptor concentration of 5×10^{16} cm^{-3} together with electron and hole mobilities of 3000 $cm^2V^{-1}s^{-1}$ and 65 $cm^2V^{-1}s^{-1}$

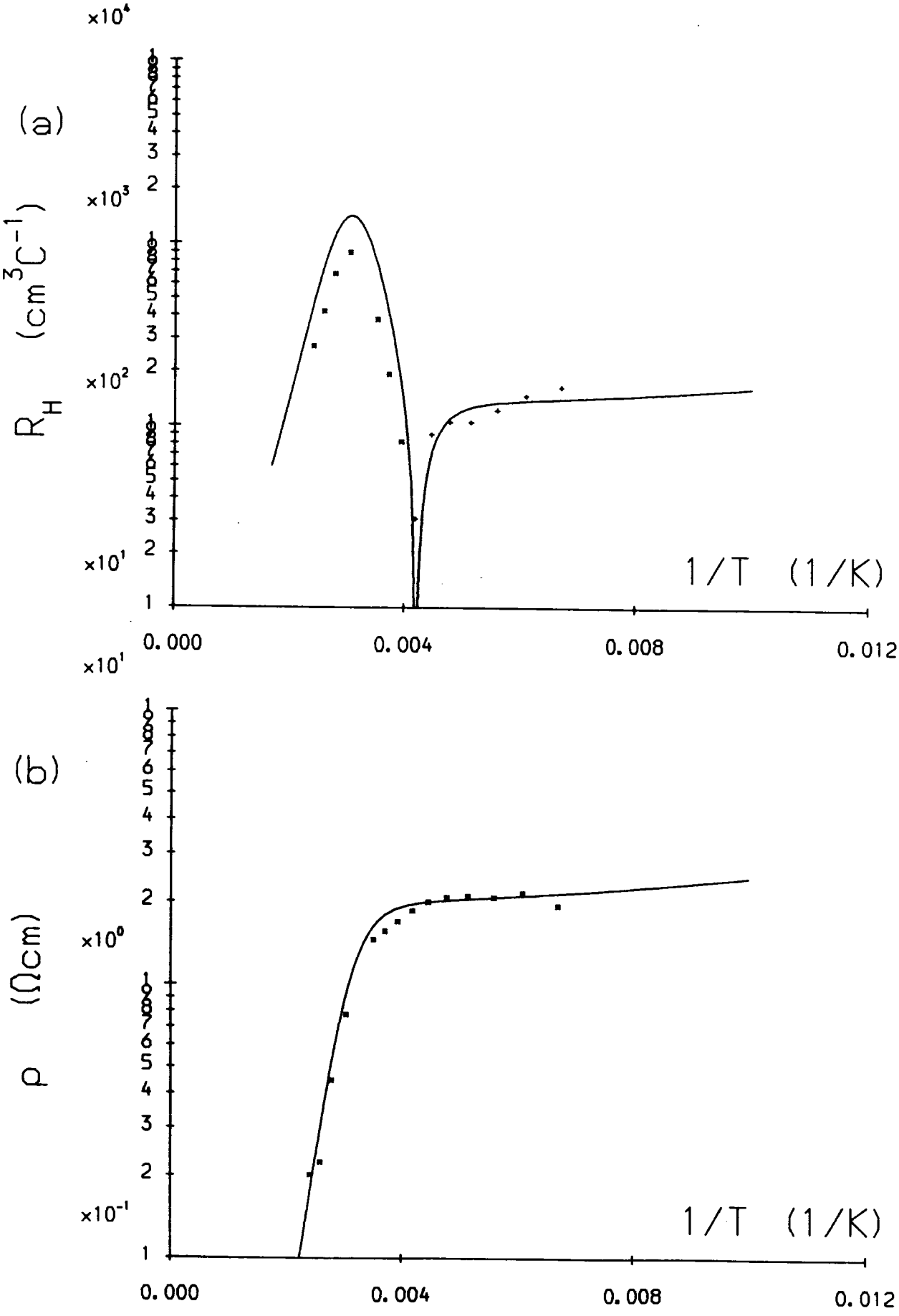

Fig. 5.9(a) Hall coefficient (R_H) versus inverse temperature ($1/T$) and (b) resistivity (ρ) versus ($1/T$) for GEC630.

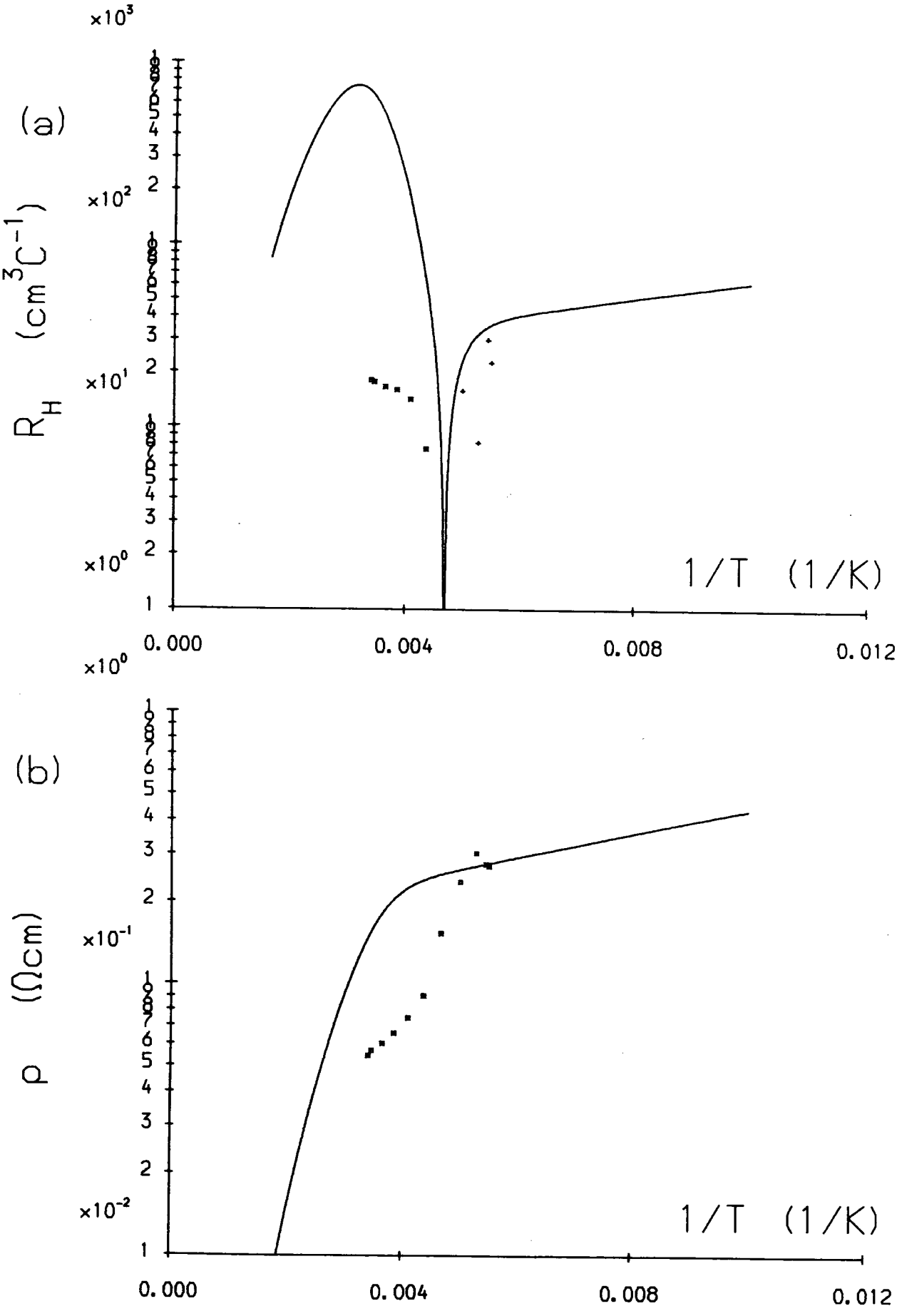

Fig. 5.10(a) Hall coefficient (R_H) versus inverse temperature ($1/T$) and (b) resistivity (ρ) versus ($1/T$) for MCT37.

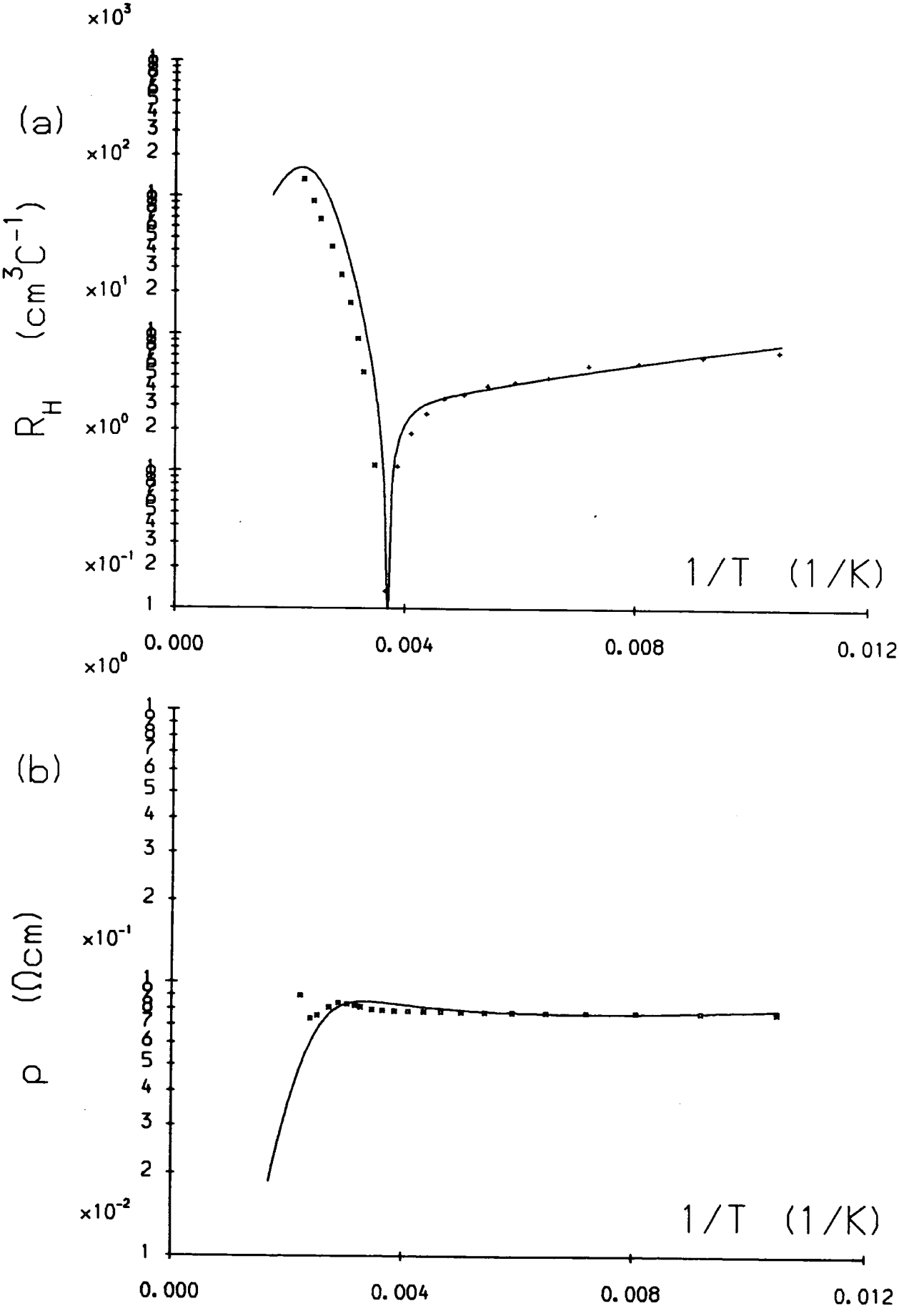

Fig. 5.11(a) Hall coefficient (R_H) versus inverse temperature ($1/T$) and (b) resistivity (ρ) versus ($1/T$) for MCT77.

independent of temperature gives an excellent fit to the data. The acceptor concentration was determined directly from the low temperature Hall coefficient using equation (4.22) while the hole mobility was taken to be the ratio of R_H to ρ at low temperature. The electron mobility was chosen to give a crossover temperature in agreement with experiment. An acceptor ionisation energy of 10 meV taken as a typical value from the literature[26] was also included although in this case the acceptors are virtually completely ionised even at the lowest temperature of measurement (150 K). The assumption of a hole mobility independent of temperature is justified by the near constant resistivity in the extrinsic region. It can be seen that the predicted magnitude of the negative going peak in R_H is larger than the maximum experimentally observed value. As described in section 4.5 the size of this peak relative to the low temperature value of R_H is related to the electron to hole mobility ratio. It may be that the mobility ratio is lower at this temperature than at the crossover temperture.

Data obtained from MCT37, an early Durham grown layer which infra-red transmission measurements showed to be non-uniform, yielding x values of 0.35 and 0.36, are shown in Fig 5.10. R_H is positive at low temperature and indicates a hole concentration of $\sim 2 \times 10^{17}$ cm^{-3}. The ratio of the low temperature values of R_H and ρ yields a value of 140 cm^{2}V^{-1}s^{-1} for the hole mobility. However, using these parameters together with the assumption of an electron to hole mobility ratio of 100 in the multicarrier model leads to the prediction of a sign change at 328 K instead of the experimental value of 214 K.

Given that the sample is of non-uniform composition, it is reasonable to assume that the electron concentration is controlled by the region of lowest x and that the acceptor concentration is also non-uniform. A variation in carrier concentration through a layer was shown in section 4.5 to provide a mechanism for the crossover occuring at a lower temperature than might be expected from the value of R_H in the extrinsic region.

Taking both of these effects into account by assuming a composition of $x = 0.3$ and acceptor concentrations of 5×10^{17} cm^{-3} in one half of the layer and 3×10^{15} cm^{-3} in the other together with the mobilities discussed above results in the fit shown. The sign change is correctly predicted although the fit is generally poor with the resistivity falling at temperatures significantly below those expected to produce intrinsic electrons and the absence of the expected large negative going peak in R_H. It is likely that the actual distribution of carriers and its temperature dependence is considerably more complex

than has been assumed in this simple model and that this accounts for the discrepancy between the experimental data and the theory.

Fig. 5.11 shows data obtained from MCT77, a later Durham grown layer which the optical data showed to be laterally uniform. The layer is clearly p-type with a much larger apparent acceptor density than either GEC630 or MCT37 as revealed by the lower value of R_H in the extrinsic region. In contrast to the GEC sample, this higher doping concentration together with a slighly larger energy gap ($x = 0.32$) prevented investigation of the intrinsic region even at the highest measurement temperature of 448 K which was obtained by heating the cryostat coldfinger electrically.

As in the case of MCT37, the crossover temperature cannot be explained on the basis of a uniform composition and acceptor concentration without the assumption of an unreasonably large electron mobility. In this case however, the optical data show the layer to be uniform. The data are therefore modelled by assuming the sample to consist of two p-type sub-layers of equal thickness with acceptor concentrations of $2 \times 10^{19}\text{cm}^{-3}$ and $1 \times 10^{16}\text{cm}^{-3}$ and using mobilities as discussed below.

In the low temperature hole dominated region R_H falls significantly with increasing temperature indicating hole generation. This may be explained using the previously assumed value of 10 meV for the acceptor ionisation energy by the fact that the highly doped sub-layer is in fact becoming degenerate. At 95 K, the lowest temperature of measurement, only 14% of the acceptors are ionised and the Fermi energy determined using equation (4.11) is slightly less than the acceptor level at $\sim$ 6 meV above the valence band. As the temperature increases, the valence band effective density of states increases according to equation (4.8) allowing more of the acceptors to ionise.

Inspection of the resistivity data shows that, although the hole concentration increases in the low temperature region, the resistivity is almost constant and in fact rises slightly at the highest temperature. The hole mobility (μ_h) was therefore modelled empirically by taking it to be the Hall mobility (μ_{h0} at 95 K (T_0)) and assuming a power law dependence on temperature (T) of the form:

$$\mu_h = \mu_{h0}\left(\frac{T}{T_0}\right)^A \tag{5.15}$$

The best fit was obtained for $A = -1.1$ with $\mu_{p0} = 100\ \text{cm}^2\text{V}^{-1}\text{s}^{-1}$. By comparison,

values of up to $\sim 1000\ cm^2V^{-1}s^{-1}$ are reported[27] in the literature for the hole mobilitiy in $Hg_{1-x}Cd_xTe$.

In the case of the electron mobility, the model is only affected over the restricted range of temperatures from near the crossover to the intrinsic region. Accordingly, a constant electron mobility of $6500\ cm^2V^{-1}s^{-1}$ was assumed. At the crossover temperature, the ratio of mobilities is therefore 200. As described in section 4.5 the ratio of the magnitude of the negative going peak in R_H to its value in the extrinsic region is representative of the mobility ratio. This value of electron mobility was the minimum sufficient to give a peak larger than the highest measured value of the Hall coefficient. Fitting of the cross over temperature was then achieved by selecting a suitable value for the acceptor concentration in the low-doped sub-layer as detailed above.

N-type Material

In section 5.4 the annealing of MCT78 at low temperature under conditions of almost saturated mercury vapour pressure was described. This was performed with the aim of anihilating mercury vacancies to reveal the background donor concentration usually found in $Hg_{1-x}Cd_xTe$. The anneal was performed with the sample at 246°C and with a mercury vapour pressure of 46 Torr. In Fig. 5.7 the expected variation of Na with mercury vapour pressure at this temperature is plotted. It can be seen that the anneal would be expected to yield material with an acceptor concentration of $\sim 10^{13}\ cm^{-3}$.

Transport data for MCT78 are presented in Fig. 5.12. The layer is clearly n-type as evidenced by the form of the data and the Hall mobility of $6700\ cm^2V^{-1}s^{-1}$ at 110 K and the Hall data may be fitted simply using the model for n-type material described in section 4.5. This value of electron mobility compares with a value of $1 \times 10^4\ cm^2V^{-1}s^{-1}$ at 77 K obtained by Lacklison and Capper[28] for bulk grown $x = 0.34$ $Hg_{1-x}Cd_xTe$. In order to obtain the fit shown, a donor concentration of $4.2 \times 10^{15}\ cm^{-3}$, obtained from R_H in the extrinsic region, was used together with an x value of 0.32. This x value gave the best fit to the intrinsic portion of the data and is slightly lower than the value of 0.34 obtained from the optical determination of the parabolic energy gap. The donor concentration is two orders of magnitude greater than the predicted acceptor concentration and accordingly should be a true measure of the residual donor concentration.

The simplification afforded by the effective presence of only one kind of carrier over

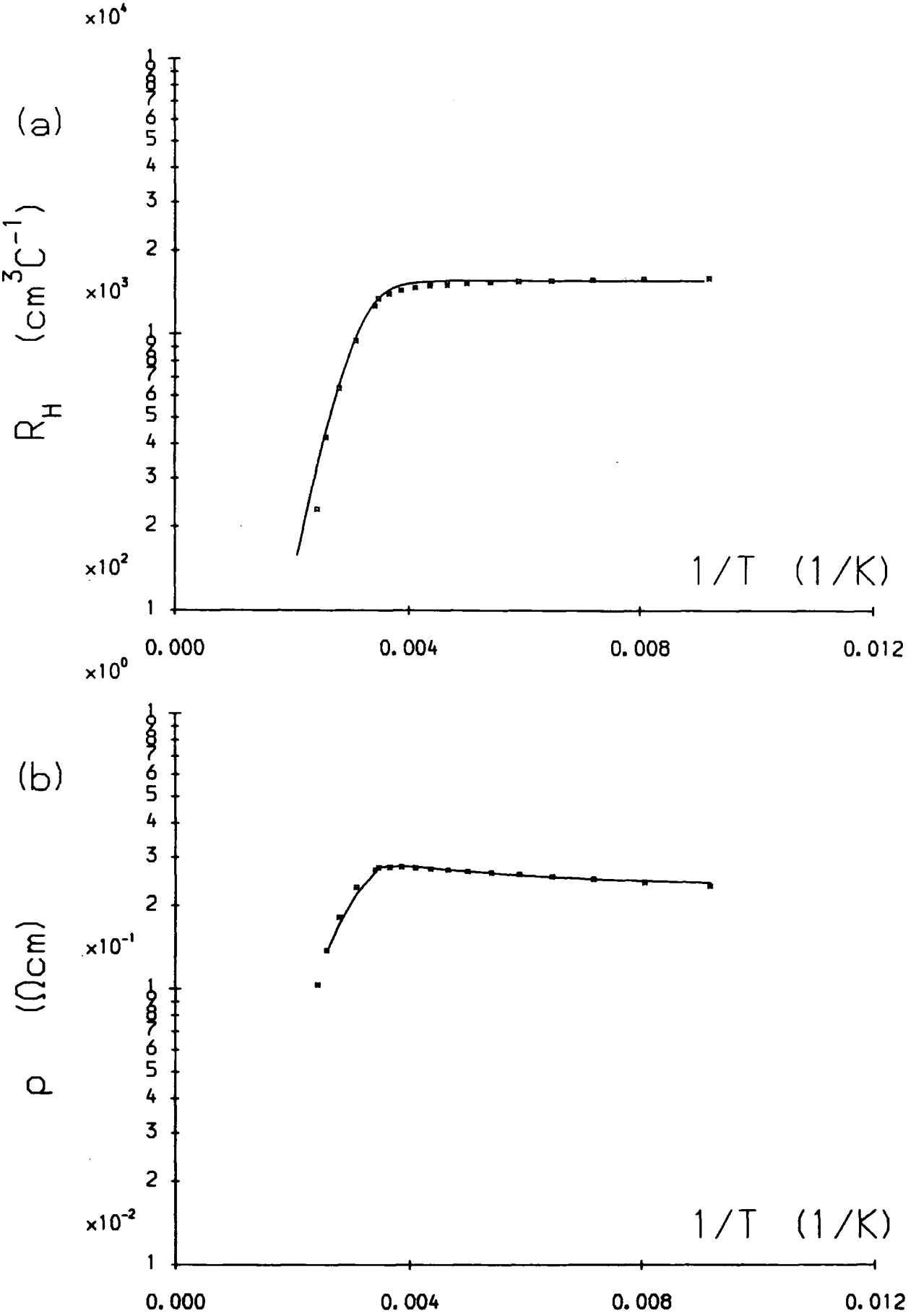

Fig. 5.12(a) Hall coefficient (R_H) versus inverse temperature ($1/T$) and (b) resistivity (ρ) versus ($1/T$) for MCT78.

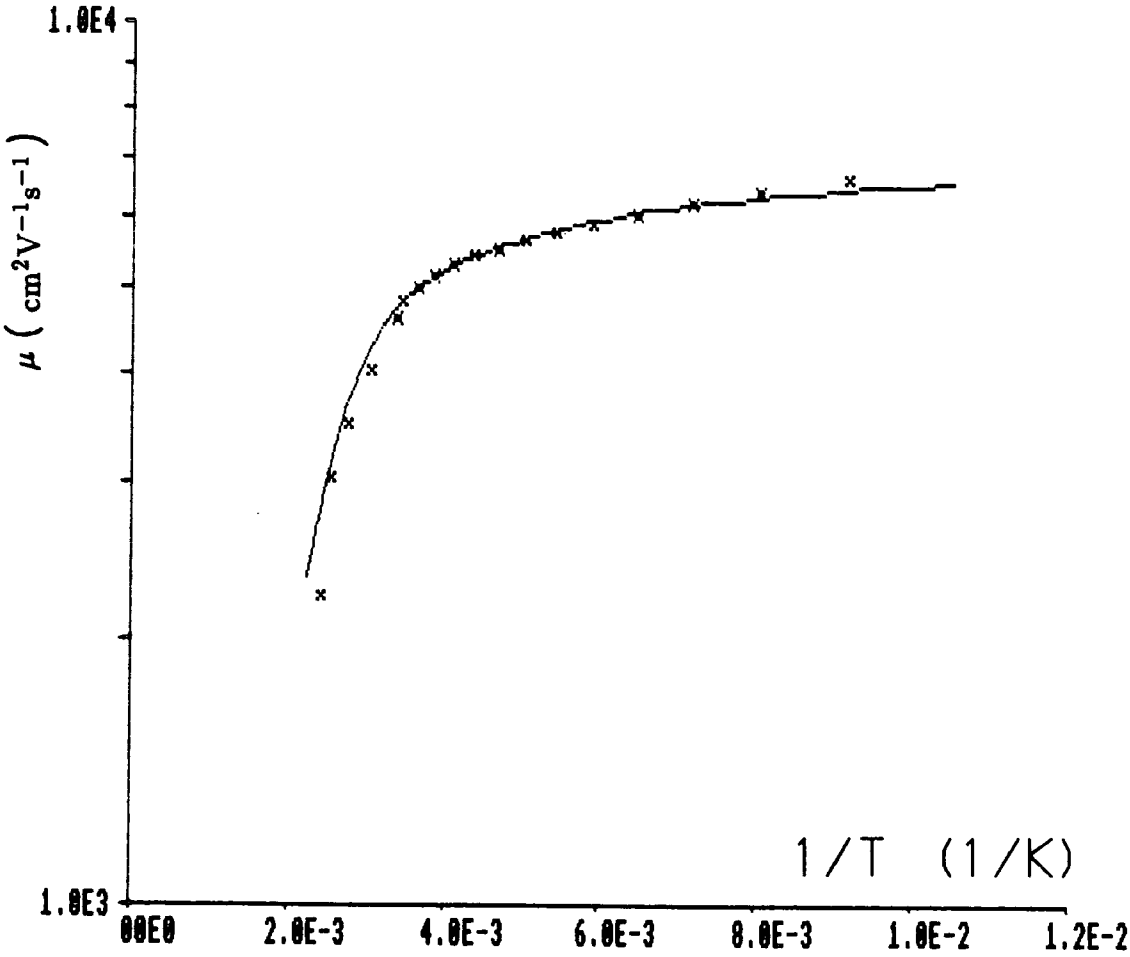

Fig. 5.12(c) Mobility (μ) versus inverse temperature ($1/T$) for MCT78.

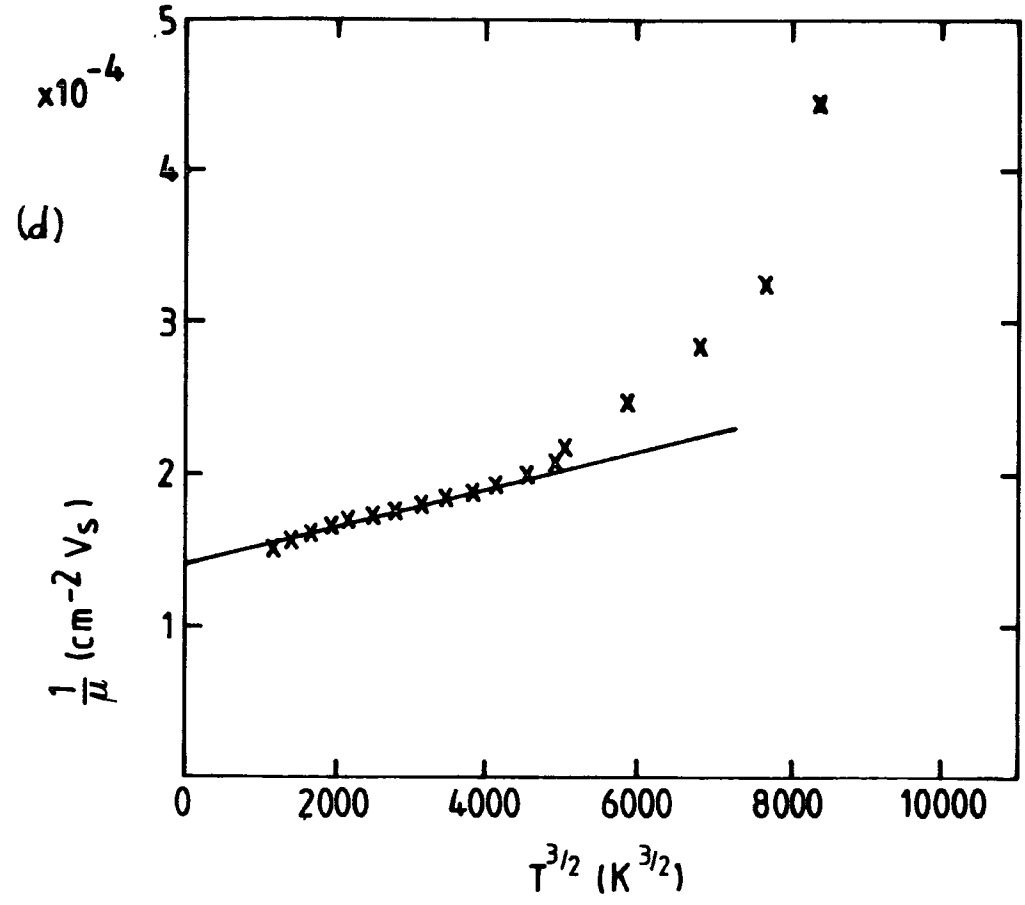

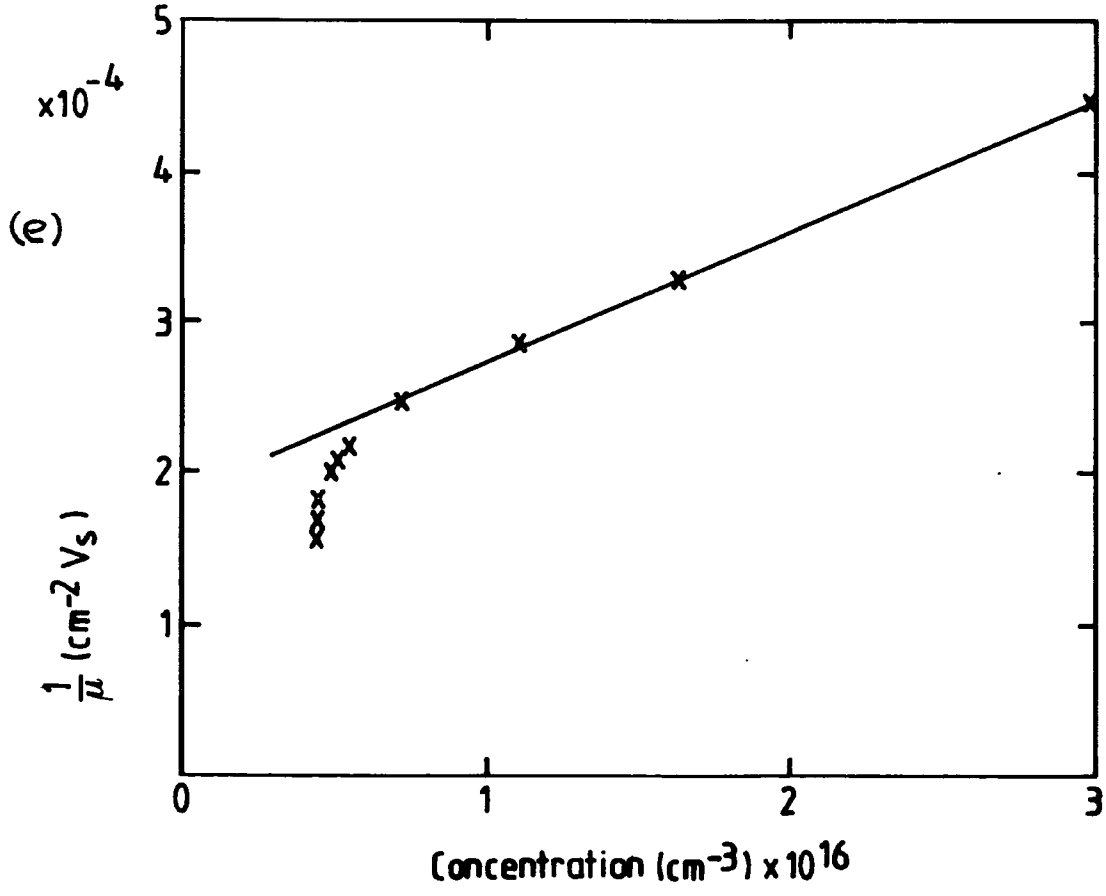

Fig. 5.12(d) $1/(\mu)$ versus $T^{\frac{3}{2}}$ and (e) $1/(\mu)$ versus carrier concetration for MCT78.

the entire temperature range of measurement allows some consideration of the temperature dependence of the electron mobility (Fig. 5.12(c)). It can be seen that the mobility falls gradually in the extrinsic region and then more rapidly as the material becomes intrinsic. In the extrinsic region, as the carrier concentration remains virtually constant, the fall in mobility may be associated solely with temperature while the sharper fall in the intrinsic region may be mainly associated with the increase in carrier concentration. The association of a scattering mechanism with carrier concentration has no physical interpretation and is introduced here simply as a method of fitting the temperature dependence of the mobility at high temperatures. The mobility may therefore be modelled empirically as the combination of three different scattering mechanisms:

(1) Temperature dependence $\mu_T = K_T.T^A$

(2) Concentration dependence $\mu_C = \frac{K_C}{n}$

(3) Temperature independent scattering μ_I

where μ_I is essentially a constant mobility term included as a fitting parameter. For this work the constant, A, was taken to be $\frac{-3}{2}$ as expected for lattice scattering[29] .

These three terms may be combined under the assumption that Mathiessen's rule applies to give the actual mobility:

$$\frac{1}{\mu} = \frac{1}{\mu_T} + \frac{1}{\mu_C} + \frac{1}{\mu_I} \tag{5.16}$$

Differentiating this expression with respect to temperature and electron concentration yields the following partial differentials:

$$\frac{\partial(\frac{1}{\mu})}{\partial T^{\frac{3}{2}}} = \frac{1}{K_T} \quad : \quad \frac{\partial(\frac{1}{\mu})}{\partial n} = \frac{1}{K_C} \tag{5.17}$$

Thus K_T and K_C may be determined from the gradients of plots of $\frac{1}{\mu}$ against $T^{\frac{3}{2}}$ and n respectively. This is shown in Fig. 5.12(d),(e) and yields values for the two constants of:

$K_T = 8 \times 10^7 (\mathrm{cm}^{-2}\mathrm{VsK}^{\frac{2}{3}})$

$K_C = 1.27 \times 10^{20} (\mathrm{cmVs})$

μ_I may then be determined by solving (5.16) using these values of K_T and K_C together with the measured values of mobility and temperature. At 110 K (the lowest temperature of measurement), μ_I was found to be 9850 $cm^2V^{-1}s^{-1}$. μ_T and μ_C were 69000 $cm^2V^{-1}s^{-1}$ and 30000 $cm^2V^{-1}s^{-1}$ respectively at low temperature and 9500 $cm^2V^{-1}s^{-1}$ and 4300 $cm^2V^{-1}s^{-1}$ respectively at the highest temperature of measurement (413 K). It can be seen from these values that, at low temperatures, the mobility is essentially temperature independent.

The solid curves in Figs. 5.12(b) and 5.12(c) were produced using this model and, in the case of the resistivity (Fig. 5.12(b)), values of electron concentration determined directly from the measured values of R_H. Values of carrier concentration were not determined directly from the model used to fit the Hall data as the slight discrepancy between the measured and theoretical values affected the fit to the resistivity.

Inverted p-type material

The data obtained from MCT71 are shown in Fig. 5.13. This sample had been the subject of an unsuccesful attempt at performing a low temperature anneal in mercury vapour. In this case, vacuum was lost during the ampoule sealing process and so the sample was exposed to an oxygen containing ambient during the heat treatment. In the absence of any infra-red transmission data, the composition was taken to be $x = 0.3$. R_H is negative and increases in magnitude towards the higher temperatures although the intrinsic region was not reached and the apparent Hall mobility of 90 $cm^2V^{-1}s^{-1}$ is close to that previously found for p-type material. As described in section 4.6 this type of behaviour is indicative of weakly inverted p-type material where the resistivity, unlike R_H, is essentially controlled by the concentration and mobility of holes at temperatures where the material is extrinsic. Use was made of this latter feature in order to determine the temperature dependence of the hole mobility. A power law dependence of the form of equation (5.15) was assumed and it was found that $A = -1.3$ provided the best fit to the data. The low temperature electron and hole mobilities were taken to be the same as for MCT77 i.e. 6500 $cm^2V^{-1}s^{-1}$ and 100 $cm^2V^{-1}s^{-1}$ respectively. Using this value of hole mobility the effective total acceptor concentration was determined to be 2.56×10^{19} cm^{-3} from the low temperature value of resistivity. The inversion layer electron sheet concentration was then found to be 4.72×10^{11} cm^{-2} using the two carrier expression for R_H (4.27) together with (4.35). This value of N_s compares with values of 3×10^{11} cm^{-2} to 1.3×10^{12} cm^{-2} determined from a study of accumulation layers at anodic oxide

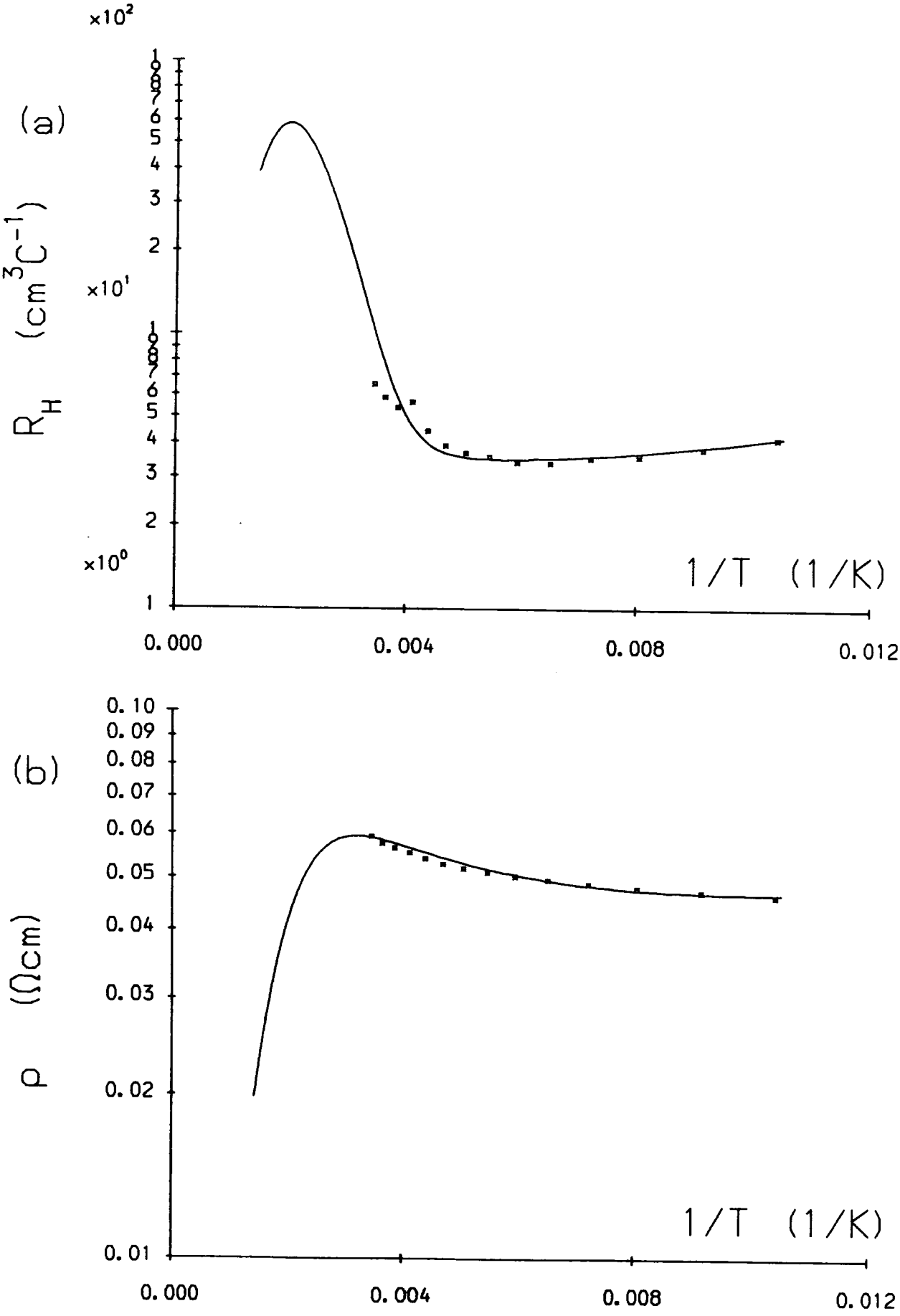

Fig. 5.13(a) Hall coefficient (R_H) versus inverse temperature ($1/T$) and (b) resistivity (ρ) versus ($1/T$) for MCT71.

films on $Hg_{1-x}Cd_xTe$ using the Shubnikov-de Haas effect made by Nasir et al.[30] . As in the case of the previously discussed p-type $Hg_{1-x}Cd_xTe$ it was necessary to assume the acceptors were distributed between low and high doped regions in order to correctly fit the rise in R_H at high temperatures. Acceptor concentrations of 5.3×10^{19} cm^{-3} and 3.0×10^{15} cm^{-3} in two sub-layers of equal thickness were used for the fit shown. It was also found necessary to include the temperature dependence of the electron mobility in order to give a satisfactory fit to the data. This was done by assuming a power law dependence as for the holes but with the constant A set equal to -0.5.

5.6 ZnTe Capped Material

A RHEED pattern obtained from a $Hg_{1-x}Cd_xTe$ layer capped with ZnTe (MCT86) is shown in Fig.5.15. The capping layer is good quality single crystal and has a smooth surface morphology as indicated by the streaks of diffracted intensity lying perpendicular to the shadow edge. Twinning is evident from the pairs of spots in this $< 110 >$ pattern, although whether this corresponds solely to the twinning expected in the $Hg_{1-x}Cd_xTe$ or is in part due to the growth of the ZnTe itself is impossible to determine. When cross-sections of capped samples were examined using EDX, no detectable level of zinc (i.e. $> 1\%$) was observed in the $Hg_{1-x}Cd_xTe$ layers. This indicated that neither residual zinc from previous growth runs nor zinc diffusing from the capping layer were affecting the composition of the $Hg_{1-x}Cd_xTe$ significantly.

Fig.5.14 shows the Hall coefficient and resistivity data taken from MCT86. To eliminate the possibility that the ZnTe cap was affecting the electrical measurements directly, it was removed using a solution of 1% bromine in methanol and the measurements repeated. These measurements are also presented in Fig.5.14 (triangles). The two sets of data are virtually identical indicating that the observed effects are not due to the ZnTe directly or to the $ZnTe/Hg_{1-x}Cd_xTe$ interface.

R_H is negative at all temperatures of measurement (95 K to 393 K) and may be divided into two regions:

(a) a low temperature region where R_H falls gradually with temperature

and

(b) a high temperature intrinsic like region where R_H is exponentially related to $\frac{1}{T}$.

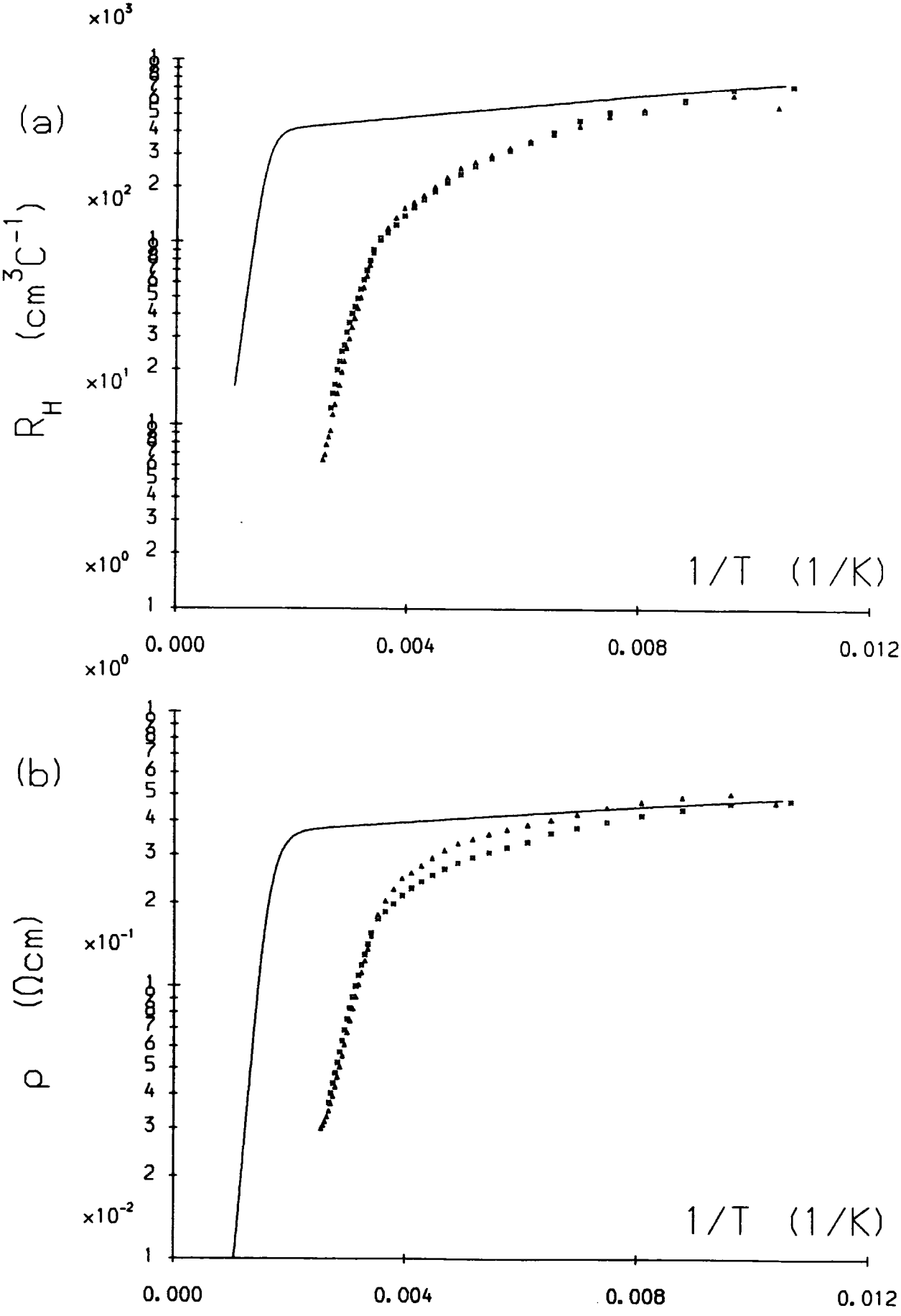

Fig. 5.14(a) Hall coefficient (R_H) versus inverse temperature ($1/T$) and (b) resistivity (ρ) versus ($1/T$) for MCT86.

	GEC630	MCT37	MCT77	MCT78	MCT71	MCT86
thickness (μm)	10.0	13.2	16.5	13.2	8.0	5.0
x (optical)	-	0.36 : 0.35	0.32	0.34	-	0.40
x (electrical)	0.29	0.3	0.32	0.32	0.3	0.25
E_g (eV) (parabolic)	-	0.376 : 0.359	0.313	0.346	-	0.430
R_H (cm^3C^{-1}) (low temperature)	163	18	7.58	-1440	-4.17	-698
ρ (Ωcm) (low temperature)	1.94	0.0545	0.0776	0.216	0.0462	0.478
crossover temperature (K)	240	214	275	-	-	-
N_a (cm^{-3}) (sublayer 1)	5.0×10^{16}	5.0×10^{17}	2.0×10^{19}	-	5.3×10^{19}	4.0×10^{17}
(sublayer 2)	5.0×10^{16}	3.0×10^{15}	1.0×10^{16}	-	3.0×10^{15}	4.0×10^{17}
N_s (cm^{-2})	-	-	-	-	4.72×10^{11}	2.4×10^{12}
N_d (cm^{-3})	-	-	-	4.2×10^{15}	-	-
μ_h ($cm^2V^{-1}s^{-1}$)	65	140	100	-	100	20
μ_e ($cm^2V^{-1}s^{-1}$)	3000	14000	6500	6700	6500	2000
b	46	100	65	-	65	100

Table 5.2 Summary of electrical properties.

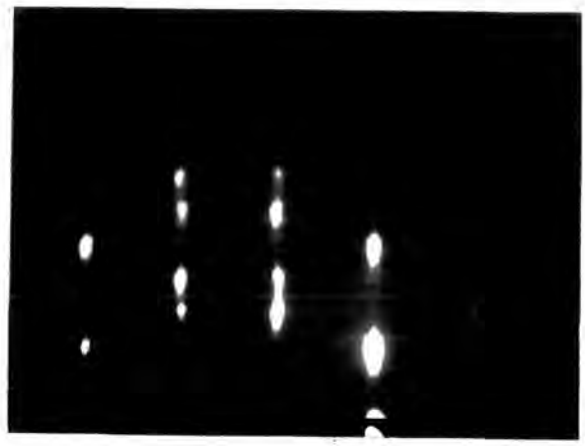

Fig. 5.15 RHEED pattern obtained from the ZnTe capping layer on MCT86.

At the lowest temperature of measurement, the apparent Hall mobility is 1460 $cm^2V^{-1}s^{-1}$. This is intermediate between the values previously found for electrons and holes. Taken with the form of the characteristic, this observation suggests that the layer is a strongly inverted p-type layer as described in section 4.5. Equations (4.27) and (4.28) may then be applied using the low temperature values of R_H and ρ to yield the hole concentration and the effective inversion layer concentration at low temperature if electron and hole mobilities are assumed. The acceptor concentration could then be determined from the low temperature hole concentration by solving (4.14). It was found that, in order to satisfy the condition for strong inversion ($n_e.\mu_e > n_h.\mu_h$ equation (4.47)), it was necessary to assume mobilities of 2000 $cm^2V^{-1}s-1$ and 20 $cm^2V^{-1}s-1$ respectively if the mobility ratio was taken to be 100, much lower than found previously. This analysis yielded values for Ns and Na of 2.4×10^{12} cm^{-2} and 4×10^{17} cm^{-3} respectively. The solid curve in Fig. 5.14 gives the prediction of the multicarrier/multilayer model for these parameters and an x value of 0.4 as determined from the optical measurements. It can be seen that there is a considerable discrepancy between the theoretical curve and the experimental data. In particular, intrinsic behaviour appears to occur at a much lower temperature than predicted. Additionally, the slope of the predicted intrinsic region is not the same as that of the high temperature data from the sample indicating that activation energy of the conduction process is not consistent with the energy gap of $x = 0.4$ $Hg_{1-x}Cd_xTe$.

The fact that the observed data does not match the expected behaviour of intrinsic $Hg_{1-x}Cd_xTe$ at high temperatures taken together with the anomalously low mobilities required to fit the data indicates that the observed electrical behaviour is not due to the layer itself but is in fact a surface or interface effect. Further evidence for this hypothesis comes from the resistivity which is one order of magnitude greater than for the previously discussed p-type Durham grown material (Table 5.2). It may be that the capping layer has reduced mercury loss from the layer and that the resulting reduced conductivity has revealed surface or interface effects which are not significant in the more heavily doped samples. This particular sample was also less than half the thickness than the earlier layers due the growth problems described in chapter 2 and this would also act to increase the significance of surface or interface effects. The nature of such surface or interface effects is not certain. If they were due to the the sample surface then the etching carried out in order to remove the cap would be expected to change electrical measurements. In fact no such change was observed. It may be that

the observed behaviour is due to the $Hg_{1-x}Cd_xTe$/CdTe interface.

5.7 Discussion and Conclusions

The infra-red transmission data obtained from Durham grown $Hg_{1-x}Cd_xTe$ show that the IMP process described in chapter 2 was yielding material with composition generally in the range $x = 0.32$ to $x = 0.36$. This range of compositions corresponds to energy gaps in the range 0.31 eV to 0.38 eV and to cutoff wavelengths from 4μm to 3.3μm. Except for one early layer lateral composition and thickness uniformity is excellent over the sample areas used in this work ($\sim 1\text{cm}^2$) as evidenced by the overlap of I.R. spectra taken from different parts of the same sample. This uniformity is a consequence of the Interdiffused Multilayer Process used for the growth and is due to the alternate growth of the constituent binaries where the reaction rates are controlled simply by the concentration of one of the precursors.

The optical absorption data also indicate the presence of an exponential band tail extending approximately 40 meV below the parabolic band edge, an effect which is generally observed in $Hg_{1-x}Cd_xTe$. For bulk material, grown under conditions of thermal equilibrium, it has been suggested that this band tailing is due to the presence of structural defects. In the case of the epitaxial material considered here, although the poor crystalline quality of the CdTe substrates must have been reflected in the quality of the layers, a sharpening of the absorption edge was observed for the later samples, for which, presumably, preparation procedures had been improved. It may be that the substrate preparation prior to growth was affecting the quality of the layers. Interestingly, the absorption coefficient is exponentially dependent on photon energy up to an absorption coefficient of $\sim 1000\ \text{cm}^{-1}$ both for the material reported here and for that reported in the literature.

In order to interpret the electrical transport data, a multicarrier/multilayer model was used. This model contains a large number of variable parameters and so the fits to the data obtained may not be unique. However, it is still possible to make a number of points about Durham grown material. Firstly in p-type Durham material the effective total acceptor concentration is very high, in the region of $10^{19}\ \text{cm}^{-3}$. This is approximately 2 orders of magnitude greater than that predicted by the theory of Yang et al[(5.13)] although it is in good agreement with the acceptor concentration found

in sample GEC630 which was grown under nominally the same conditions of temperature and mercury vapour pressure. Furthermore for Durham grown material it was also necessary to assume the presence of much lower doped regions (10^{15} cm^{-3} to 10^{16} cm^{-3}) in each sample in order to explain the observed crossover temperatures. It may be concluded, therefore, that the acceptor concentration varied through the thickness of the layers with a concentration lower than that expected for the growth conditions in some regions and a higher concentration in others. The Hall data for the ZnTe capped sample are difficult to interpret on the basis of the known properties of $Hg_{1-x}Cd_xTe$. One reason for this is the relatively high resistivity found for this sample. This low conductivity indicates that the acceptor concentration in this sample was at least one order of magnitude lower than found in the uncapped samples. Accordingly it may be concluded that the capping layer prevented mercury loss during the cool down phase of the growth cycle and thus that it is conditions during the cool down which lead to the non-uniform acceptor concentration in the uncapped samples.

For Durham grown material which had been converted to n-type by annealing under almost saturated mercury vapour pressure at low temperature the analysis of the electrical data was straight forward with the x value as determined by the optical and electrical characterisations are in good agreement. The 110 K electron mobility was found to be 6700 $cm^2V^{-1}s^{-1}$ which is consistent with the electron mobilities found to provide a good fit to the data obtained from p-type material. This value is approximately 65 times greater than the hole mobility thus justifying the use of the simplifications afforded by the assumption of a large mobility ratio. The residual donor concentration was found to be 4×10^{15} cm^{-3}, in good agreement with that typically reported in the literature[25] .

It has also been possible to give some consideration to the temperature dependence of carrier mobilities in $Hg_{1-x}Cd_xTe$. For p-type Durham grown material, a power law temperature dependence of the hole mobility with the constant A in the range -1.1 to -1.3 was found to give a good fit to the experimental data. This is slightly lower than the value of -1.5 expected for lattice scattering. In the case of the GEC sample, however, a satisfactory fit was obtained by assuming that the mobilities were constant. Mobilities in $Hg_{1-x}Cd_xTe$ are generally found to be virtually temperature independent in the impurity scattering regime[31] and so, given that the hole mobility for the GEC sample is ~65% of that found for Durham material, it may be concluded that this sample

contained a higher concentration of defects than the Durham material. For the n-type sample, the electron mobility was found to be relatively insensitive to temperature at low temperatures, presumably the result of impurity scattering, but to have an extremely strong temperature dependence at higher temperatures. At high temperatures, the temperature dependence of the electron mobility was modelled empirically in order to fit the resistivity data and no explanation of the origin of this effect is offered.

In conclusion, the optical and electrical properties of Durham grown $Hg_{1-x}Cd_xTe$ have been assessed. The layers have been shown to be of excellent compositional uniformity, a consequence of the IMP growth process, but to contain very high and non-uniform concentrations of acceptors. These acceptors were assumed to be due to ionised mercury vacancies which may be present in high concentrations as a consequence of the inherent weakness of the Hg-Te bond which is further weakened by the presence of Cd in the $Hg_{1-x}Cd_xTe$ lattice[21] .

REFERENCES

1. J.C. Brice in Properties of Cadmium Mercury Telluride, EMIS Datareviews Series No. 3 (1987) Ed. J.C. Brice and P. Capper.
2. Numerical Data and Functional Relationships in Science and Technology, Group III: Crystal and Solid State Physics Vol. **17** Semiconductors Ed. Landolt and Bornstein.
3. J.L. Schmit J. Vac. Sci. Technol. **A4** (1986) 2141.
4. G.J. Russell, N.F. Thompson and J. Woods. J. Crystal Growth **71** (1985) 621.
5. K. Durose and G.J. Russell. J. Crystal Growth **86** (1988) 471.
6. K. Durose and G.J. Russell. J. Crystal Growth in press.
7. H.F. Schaake and H.Y. Liu, Mat. Res. Soc. Symp. Proc. (1990) to be published.
8. J.E. Hails, G.J. Russell, P.D. Brown, A.W. Brinkman and J. Woods. J. Crystal Growth **86** (1988) 516.
9. P.D. Brown, K. Durose, G.J. Russell and J. Woods. J. Crystal Growth to be published.
10. P.D. Brown, J.E. Hails, G.J. Russell and J. Woods. J. Crystal Growth **86** (1988) 511.
11. J.E. Hails, G.J. Russell, A.W. Brinkman and J. Woods. J. Crystal Growth **79** (1986) 940.
12. J.B. Mullin, S.J.C. Irvine, J. Giess, J.S. Gough, A. Royle, M.C.L. Ward and G. Crimes, SPIE **1106** Future Infrared Detector Materials (1989).
13. E. Finkman and Y. Nemirovsky, J. Appl. Phys. **50** (1979) 4356.
14. F. Urbach. Phys. Rev. **92** (1953) 1324.
15. J.A. Mroczkowski, D.A. Nelson, R. Murosako and P.H. Zimmermann, J. Vac. Sci. Technol. **A1** (1983) 1756.
16. E. Finkman and S.E. Schacham J. Appl. Phys. **56** (1984) 2896.
17. K. Seeger, Semiconductor Physics, 3rd ed. (Springer-Verlag, 1985) ch.11.
18. J. Chu, S. Xu and D. Tang Appl. Phys. Letters **43** (1983) 1064.

19. G.L. Hansen, J.L. Schmidt and T.N. Casselman, J. Appl. Phys. **53** (1982) 7099.

20. J.B. Mullin, J. Giess, S.J.C. Irvine, J.S. Gough and A. Royle, Mat. Res. Soc. Symp. Proc. **90** (1987) 367.

21. W.E. Spicer, J.A. Silberman, J. Morgan, I. Lindau, J.A. Wilson, A.B. Chen and S. Sher, Phys. Rev. Lett. **49** (1982) 948.

22. H.R. Vydyanath, J.C. Donovan and D.A. Nelson, J. Electrochem. Soc. **128** (1981) 2625.

23. J. Yang, Z. Yu, D. Tang, J. Crystal Growth **72** (1985) 275.

24. CRC Handbook of Chemistry and Physics 59th Edition (1978) Ed. R.C. Weast

25. H.F. Schaake, J.H. Tregilgas, J.D. Beck, M.A. Kinch and B.E. Gnade, J. Vac. Sci. Technol. **A3** (1985) 143.

26. E. Finkman and Y. Nemirovsky, J. Appl. Phys. **59** (1986) 1205.

27. M.C. Chen, J. Appl. Phys. **65** (1989) 1571.

28. D.E. Lacklison and P. Capper, Semicond. Sci. Technol. **2** (1987) 137.

29. R.A. Smith in Semiconductors, Cambridge University Press 1978 ch.5.

30. F. Nasir, J. Singleton and R.J. Nicholas, Semicond. Sci. Technol., **3** (1988) 654.

31. L.F. Lou and W.H. Frye, J. Appl. Phys. **56** (1984) 2253.

6. Properties of Epitaxial ZnTe and HgTe:ZnTe and CdTe:ZnTe Superlattices

6.1 Introduction

The principal aim of the work reported in this chapter was to characterise HgTe:ZnTe superlattices with regard to their application as infra-red materials. As described in section 1.5, this system was selected as an alternative to the more widely studied HgTe:CdTe superlattice system as consideration of the interdiffusion expected between HgTe and ZnTe suggested that growth by thermal MOVPE would be feasible. Prior to the commencement of the work reported in this chapter there was, to the author's knowledge, only one report in the literature relating to the HgTe:ZnTe superlattice system[1] . This report proposed HgTe:ZnTe superlattices as an alternative to HgTe:CdTe superlattices and presented an initial characterisation of some samples grown by Molecular Beam Epitaxy. A prerequisite for the present study was the characterisation of epitaxial layers of ZnTe as this material had not previously been grown at Durham and this work is also reported here. As described in chapter two, growth of both epitaxial ZnTe and the HgTe:ZnTe superlattices was initially carried out at $\sim 400°C$ using di-ethyl tellurium. Subsequently, the tellurium precursor was changed to di-isopropyl tellurium enabling the growth temperature to be reduced to as low as 300°C. It was of interest to compare the structural properties of epitaxial layers grown in the two temperature regimes and, in particular, to determine the extent to which interdiffusion occurred within the superlattices as this would determine the feasibility of growing such structures by thermal MOVPE.

In section 6.2 the properties of ZnTe layers grown on both GaAs substrates where the lattice mismatch is large (7%) and on near lattice matched GaSb substrates (mismatch = 0.09%) are described. The HgTe:ZnTe superlattices were grown either directly onto GaAs or onto thin ($\sim$ 1000Å) ZnTe buffer layers grown on GaAs which reduced, but did not eliminate, the large lattice mismatch (7 - 12%) between GaAs and the free standing in-plane lattice parameter expected for the superlattices. In section 6.3, the structural, and in the case of one sample, optical, properties of HgTe:ZnTe superlattices grown at the higher temperatures are described. The optical data is discussed in terms of a simple calculation of the electronic structure expected for that sample. Superlattices grown at the lower temperatures are described in section 6.4. It may be possible to

use CdTe:ZnTe strained layer superlattices as buffer layers for the growth of HgTe:ZnTe superlattice active layers as discussed in chapter one. Accordingly, in section 6.5, some initial studies of CdTe:ZnTe superlattices are presented. This chapter is concluded in section 6.6.

The salient growth parameters for all of the epitaxial layers of ZnTe and HgTe:ZnTe and CdTe:ZnTe superlattices considered during the course of this work and an outline of the characterisation work performed on them are presented in Appendix II.

6.2 Properties of ZnTe

ZnTe grown on GaAs

For the growth of ZnTe at $\sim$ 400°C using di-ethyl tellurium it was found[2] that, for growth on both $\{\bar{1}\bar{1}\bar{1}\}$B CdTe and $\{\bar{1}\bar{1}\bar{1}\}$B GaAs substrates, the resulting layers were of good crystalline quality as determined by RHEED and also exhibited good morphology as evidenced by SEM observations and streaking in the RHEED patterns. In contrast, layers grown on the {100} oriented GaAs, while single crystal, were found to be ridged. The ridges lay along the [110] axis as has been previously reported[3] . A secondary electron micrograph of a 1 μm thick ZnTe layer grown on {100} GaAs at 410°C , is shown in Fig. 1. Similar observations have previously been made concerning epitaxial layers of ZnS and ZnSe grown by MOVPE on {100} GaAs[4] . In the latter case, it was suggested that there was a differential growth rate on the {111}A and $\{\bar{1}\bar{1}\bar{1}\}$B planes of the sphalerite structure, leading to the formation of ridges along one particular $< 110 >$ direction. It may be that this model is applicable here. This ridging also manifests itself in RHEED in the form of shaping of the spots for incident electron beams parallel to the [110] ridging direction. This is illustrated, for the same sample, in Fig. 2. It can be seen that for the [110] zone axis the spots have a cross-shaped distribution of intensity.

The crystalline quality of ZnTe grown at the reduced temperatures was comparable to that of layers grown at the higher temperatures , as described above. Fig.3. shows a RHEED pattern obtained from a ZnTe layer grown on {100}GaAs at 350°C . However, in contrast to growth at 410°C , the surfaces of the layers were specular and essentially featureless. Fig.4 shows a secondary electron micrograph of a ZnTe layer grown on {100}GaAs at 325°C . Use has been made of a particle on the sample surface to provide for focussing. It is of interest to note that the shape effect previously observed in RHEED for electron beams incident along the [110] ridging axis was no longer observed.

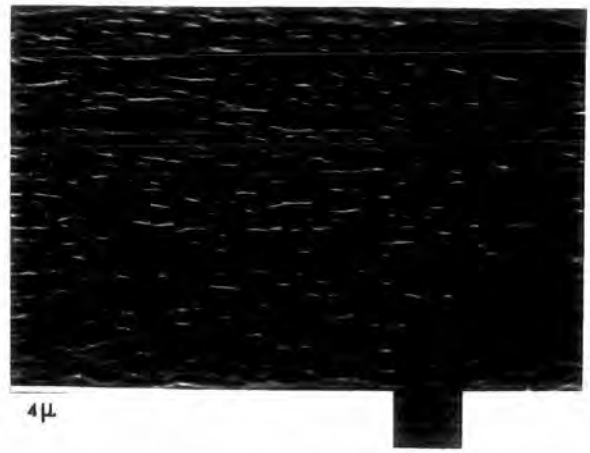

Fig.61SE micrograph of a 1μm thick ZnTe layer grown on {100} GaAs at 410°C.
(ZNTE 12)

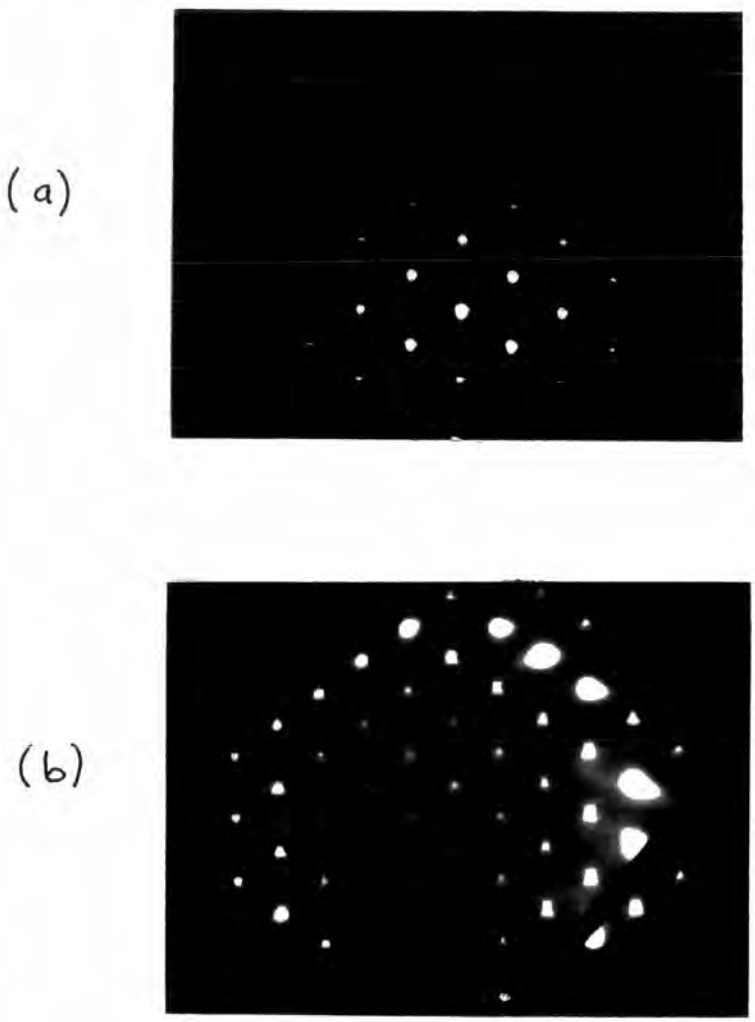

Fig. 6.2. RHEED patterns from epitaxial ZnTe on {100} GaAs with the beam incident (a) along the [1$\bar{1}$0] zone axis and (b) along the orthogonal [110] axis.
(ZNTE 12)

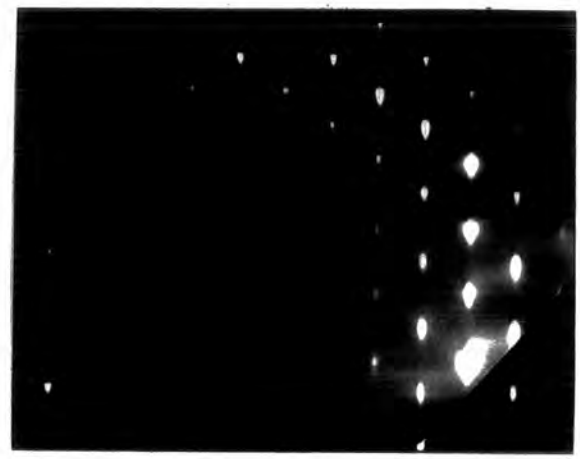

Fig.6.3 RHEED pattern obtained from a ZnTe layer grown on {100} orientated GaAs at 350°C
(ZNTE 28)

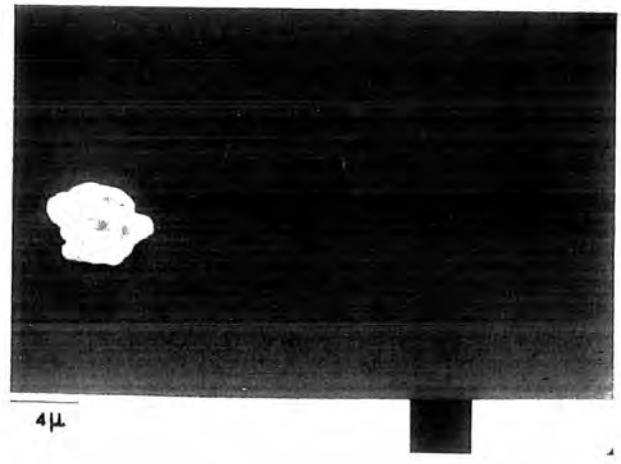

Fig.6.4 SE micrograph of a 0.8 μm thick ZnTe layer grown on {100} GaAs at 325°C
(ZNTE 29)

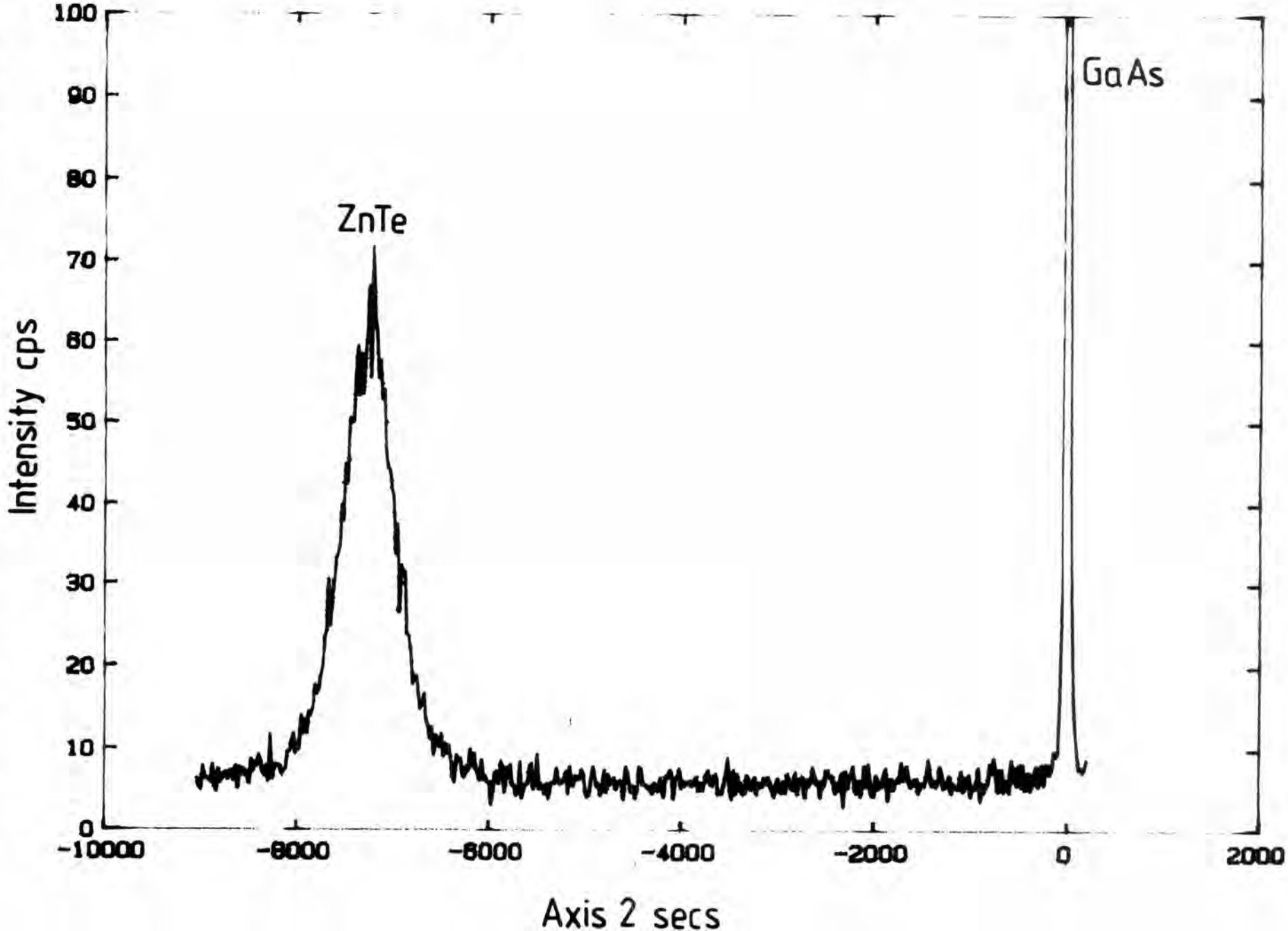

Fig. 5 DCXRD scan about the (400) reflection from a 1μm thick ZnTe layer grown on {100} GaAs at 350°C . (Z N T E 3 5)

Fig4.6. T.E. micrograph of a ZnTe layer grown on {100} GaAs at 350°C .
(ZNTE35)

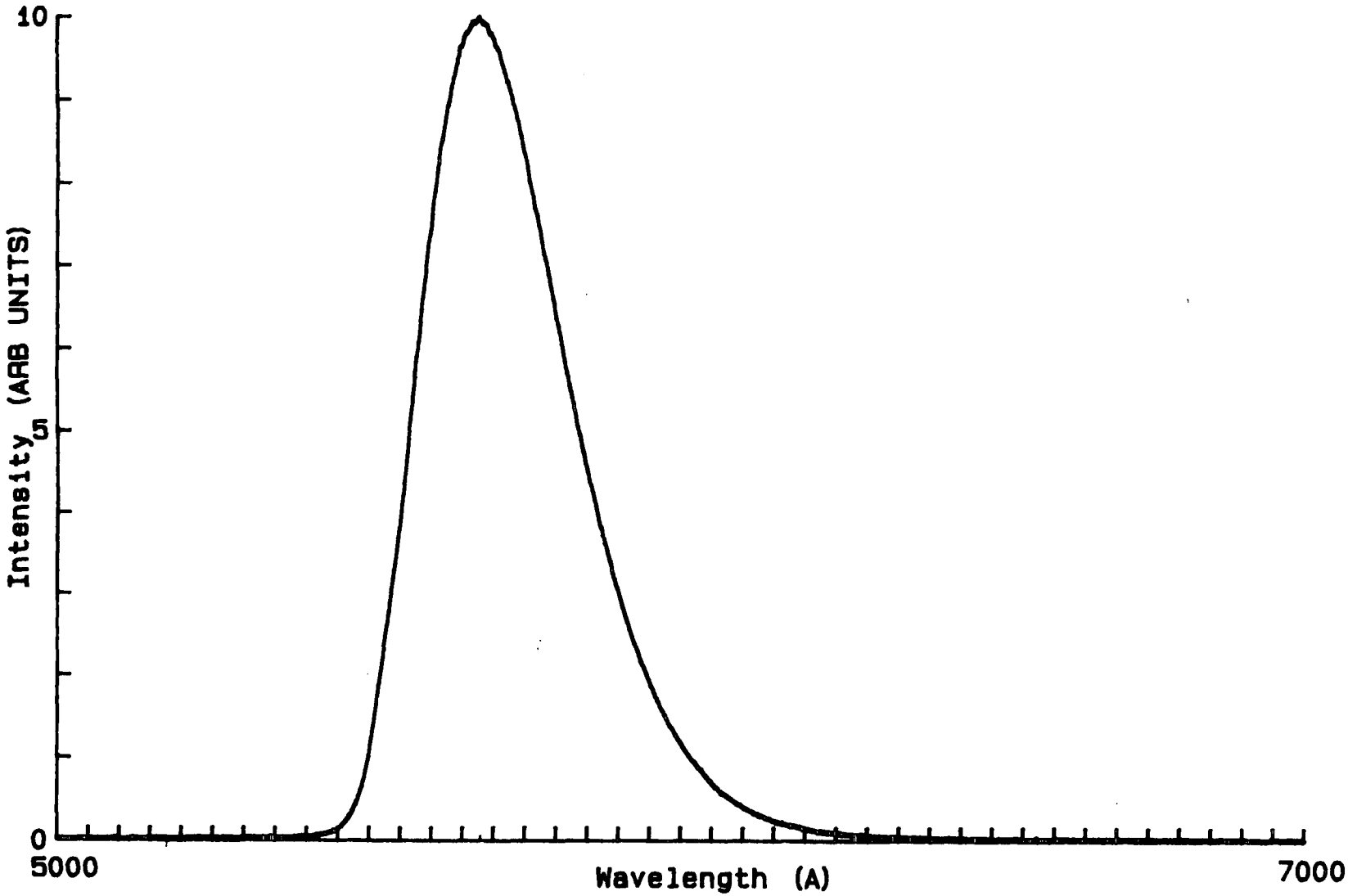

Fig.6.7. Photoluminesence spectrum obtained at 4K from a 1μm thick ZnTe layer grown on {100} GaAs at 350°C. (ZNTE35)

A DCXRD rocking curve obtained*** from a 1 μm thick ZnTe layer grown on {100} GaAs at 350°C is shown in Fig.5. DCXRD scan about the (400) reflection from ZNTE35, a 1μm thick ZnTe layer grown on {100} GaAs at 350°C . Fig.5. This scan was made with the rocking axis parallel to a $< 100 >$ crystal axis. The position of the peak is consistent with a misorientation of the ZnTe by $\sim 1°$ with respect to the GaAs substate along the [110] axis as reported by Shtrikman and coworkers[3] . Its magnitude is lower by a factor of ~ 60 than the peak from the GaAs substrate. The full width half maximum (FWHM) of the ZnTe peak is 630 seconds of arc. By comparison a perfect ZnTe layer 1 μm thick would be expected to give a peak with a magnitude comparable to the GaAs peak and a FWHM of ~ 200 seconds of arc[5] . Both of these observations indicate that the layer is of relatively poor quality as determined by DCXRD which is a far more sensitive test of crystalline quality than RHEED. Nevertheless, this rocking curve width is approximately half that obtained by Shtrikman et al for ZnTe layers of this thickness grown by MOVPE on {100} GaAs using DET at $\sim 400°C$. The absence of ridging in the sample considered here may have contributed to this reduction.

A T.E. micrograph** of a ZnTe layer grown on {100} GaAs at 350°C is shown in Fig. 6. There is an extremely large density of threading dislocations at the ZnTe:GaAs interface generated as a consequence of the relaxation of the large (7.6%) lattice mismatch. Dislocations correspond to slight misorientations of the lattice and it is these misorientations which lead to the broadening of the DCXRD peaks as described above. It can be seen, however, that the dislocations grow out to a significant extent through the thickness of the layer thus demonstrating the potential of such layers as buffers for the subsequent growth of the superlattices or other active layers.

Fig. 7 shows a photoluminesence spectrum obtained+ at 4K from a 1μm ZnTe layer grown on {100} GaAs at 350°C. This shows a single broad peak without any structure. Iodine is used during the synthesis of di-methyl zinc and it is probable that the batch of DMZ used throughout the work reported in this chapter was heavily contaminated with iodine[6] . The observed broad photoluminesence peak is consistent with this suggestion[7] . The effect of a large halogen concentration on the structural and other properties of the layers and superlattices is not clear although the halogens are known to act as compensating centres in other II-VI compounds.

*** A. Turnbull, Solid State Physics Group, Department of Physics, University of Durham
** P.D. Brown, Applied Physics Group, S.E.A.S. University of Durham.
+ J.E. Nicholls, Department of Applied Physics, University of Hull.

ZnTe grown on GaSb

In contrast to the 7.6% lattice mismatch between ZnTe and GaAs, the mismatch between ZnTe and GaSb is only 0.09% . On the basis of lattice matching, GaSb would be expected to provide an excellent substrate for ZnTe. However, much depends on the availability of a surface preparation technique which will leave a stoichiometric single crystal GaSb surface. The bromine/methanol based hydroplane polishing technique used for this work was shown by RHEED to yield single crystal GaSb surfaces and X-ray photoelectron spectroscopic studies[8] have shown that bromine/methanol etching leaves only a thin layer of gallium and antimony oxides on GaSb surfaces. It is expected that such oxide layers are reduced during heat cleaning in the MOVPE reactor.

Fig.8 shows a RHEED pattern obtained from a ZnTe layer grown on {100} GaSb at 300°C and demonstrates the good crystallinity obtained. The morphology of these layers is essentially featureless as found for growth on {100} GaAs at the same temperature. A transmission electron micrograph** of ZnTe grown on {100} GaSb at 350°C is shown in Fig.9. There appears to be a region of low defect concentration close to the layer/substrate interface which has a density consistent with the low lattice mismatch between the two materials. In addition to this however, a denser network of dislocations can be seen to start between 1000 Å and 2000 Å above the ZnTe/GaSb interface. The origin of these dislocations is not clear. Petruzzello et al.[9] observed a similar increase in dislocation density for much thicker ($> 1.3\mu$m) ZnTe layers grown on {100} GaAs by MBE. It may be that these dislocations are a growth phenomenon or they may be related to some form of strain in the layer. Alternatively, in the case of the Durham grown ZnTe, they may be a consequence of the presence of iodine in the layer.

6.3 HgTe:ZnTe Superlattices Grown at High Temperature

Structure and Interdiffusion

The surface morphology of superlattices grown at $\sim$ 400 °C on {100} GaAs substrates was similar to that of those grown on $\{\bar{1}\bar{1}\bar{1}\}$B GaAs and $\{\bar{1}\bar{1}\bar{1}\}$B CdTe substrates with no pronounced features in either case. A S.E. micrograph of a HgTe:ZnTe superlattice grown on {100} GaAs at 395°C is shown in Fig. 10. It should be noted that this micrograph was taken using a Cambridge Instruments S180 SEM instead of the

** P.D. Brown, Applied Physics Group, S.E.A.S. University of Durham.

Fig.6.10. S.E. micrograph of a HgTe:ZnTe superlattice grown at 395°C.
(MZTSL 12)

Fig.6.11. T.E. micrograph of part of a HgTe:ZnTe superlattice grown on {100} GaAs at 395°C.
(MZTSL 12)

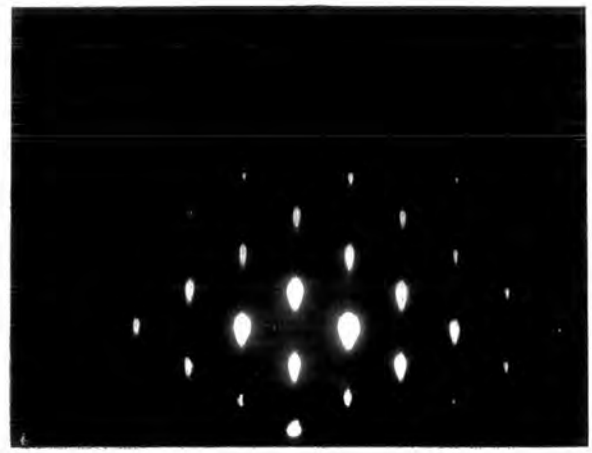

Fig.6.8 RHEED pattern obtained from a ZnTe layer grown on {100} GaSb at 300°C. (2NTE30)

Fig.6.9 TE micrograph of ZnTe grown on {100} GaSb at 350°C

(2NTE35)

S600 used for the previous two micrographs in this chapter and is of significantly higher resolution. This result contrasts with the case of single layers of ZnTe or HgTe grown on {100} oriented substrates at 395°C where the ZnTe exhibits ridging as described above and growth of HgTe results in layers with a fairly large density of $\sim 10\mu$m pyramidal features[10] . It may be that by growing thin alternating layers of the binary compounds to produce a superlattice, the tendancy of layers grown on the {100} orientation to facet is reduced.

A cross-sectional transmission electron micrograph** of a 0.75μm thick 60 period HgTe-ZnTe superlattice grown on {100} GaAs at 395°C is shown in Fig. 11. This clearly demonstrates the presence of a multilayer structure with a period of 125 Å although there is a large number of misfit dislocations which have propagated through from the substrate-superlattice interface. Such multilayer contrast was, however, only observed from the top third (20 periods) of the sample. If it is assumed that the first 40 periods had interdiffused then, knowing the period and growth time, an estimate can be made for the interdiffusion coefficient $\tilde{D}$ at the growth temperature. The characteristic diffusion length, l_c, is given by:

$$l_c = \sqrt{\tilde{D}t} \tag{6.1}$$

where t is the time for diffusion. Setting l_c equal to the superlattice period of $\approx$ 125 Å and t equal to the growth time for 20 periods (1180 seconds) yields a value for $\tilde{D}$ of $\sim 1 \times 10^{-15}$ cm^{2}s^{-1} at 395°C.

This value of the interdiffusion coefficient is one order of magnitude lower than that found for the interdiffusion of CdTe and HgTe during the development of the interdiffused multilayer process[11] for the growth of $Hg_{1-x}Cd_xTe$ which was determined under essentially similar conditions of temperature, mercury vapour pressure and annealing time. It is also at least two orders of magnitude lower than that expected from the HgTe:ZnTe diffusion couple experiments of Granger and co-workers[12] . Their work was performed in vacuum while the superlattice growth reported here took place under one atmosphere of hydrogen with a mercury partial pressure of 20 Torr. Mercury vacancies are known to have a significant influence on the interdiffusion in the $Hg_{1-x}Cd_xTe$

** P.D. Brown, Applied Physics Group, S.E.A.S. University of Durham.

system[13] and it may be that the lower interdiffusion coefficient found for the superlattice growth is due to the presence of a lower concentration of mercury vacancies.

Optical Properties

One 40 period HgTe:ZnTe superlattice grown on {100} GaAs at 395°C exhibited strong optical absorption at $\sim 6\mu$m. Calibrated EDX[++] showed this to contain 35% HgTe and 65% ZnTe. Thus, if the layer had fully interdiffused, the sample would have been an alloy of composition $Hg_{0.35}Zn_{0.65}Te$. This would have had an absorption edge at a much shorter wavelenth of $\sim 0.9\mu$m, than was observed. It was concluded that complete interdiffusion had not taken place and, from the total thickness and composition, that the layer was, at least in part, a superlattice with a 200 Å period comprising 70 Å of HgTe and 130 Å of ZnTe. Consideration of the interdiffusion coefficient discussed in the previous section suggested some interdiffusion would have taken place although even near the superlattice/substrate interface this would not have been complete as the period was greater and the growth time shorter than for the sample considered previously.

The infra-red transmission spectrum[*] for this sample is shown in Fig. 12. The optical absorption coefficient, α, was determined as a function of photon energy, $h\nu$, in the same way as was done for $Hg_{1-x}Cd_xTe$ samples in chapter 5. Graphs of α versus photon energy and $(\alpha h\nu)^2$ versus $h\nu$ for this sample are shown in Figs. 13(a) and 13(b) respectively. As found for $Hg_{1-x}Cd_xTe$, the absorption coefficient has an exponential dependence on photon energy up to values of $\sim 1 \times 10^3$ cm^{-1} and may be fitted to the empirical expression of Urbach[14]

$$\alpha = \alpha_0 exp\Big(\beta(h\nu - \epsilon)\Big) \tag{6.2}$$

where ϵ is a constant. β is the gradient of the logarithmic portion of the absorption curve and in this case is equal to 34 eV^{-1}. This value of β is approximately half that typically obtained for Durham grown $Hg_{1-x}Cd_xTe$. It may be that a variation in the degree of interdiffusion through the layer, due to the differing times that each period was at the growth temperature, has led to a variation of the energy gap through the

++ O.D. Dosser, Royal Signals and Radar Establishment, Malvern, U.K.
* J.E. Hails, Royal Signals and Radar Establishment, Malvern, U.K.

(a)

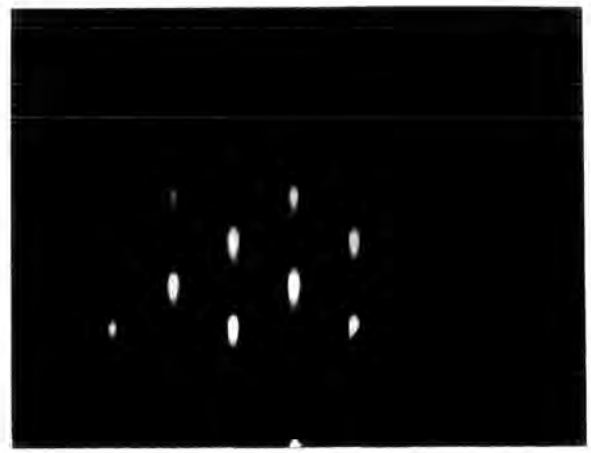

(b)

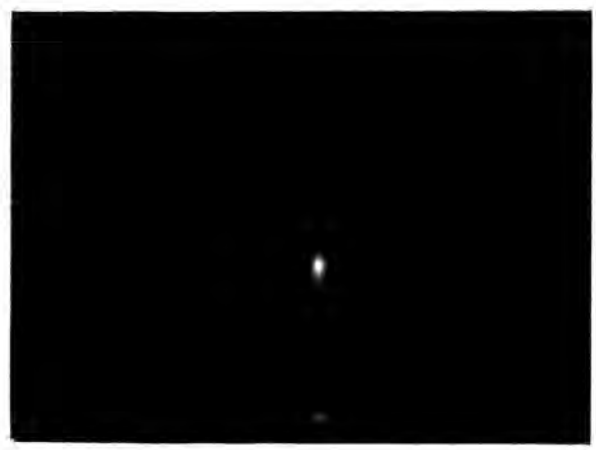

Fig.6.17. RHEED patterns obtained from a CdTe:ZnTe superlattice grown on (a) {100} GaAs and (b) $\{\bar{1}\bar{1}\bar{1}\}$B GaAs at 325°C .

(CZTSL8)

Fig.6.18. T.E. micrograph of a CdTe:ZnTe superlattice grown on {100} GaAs at 325°C .

(CZTSL8)

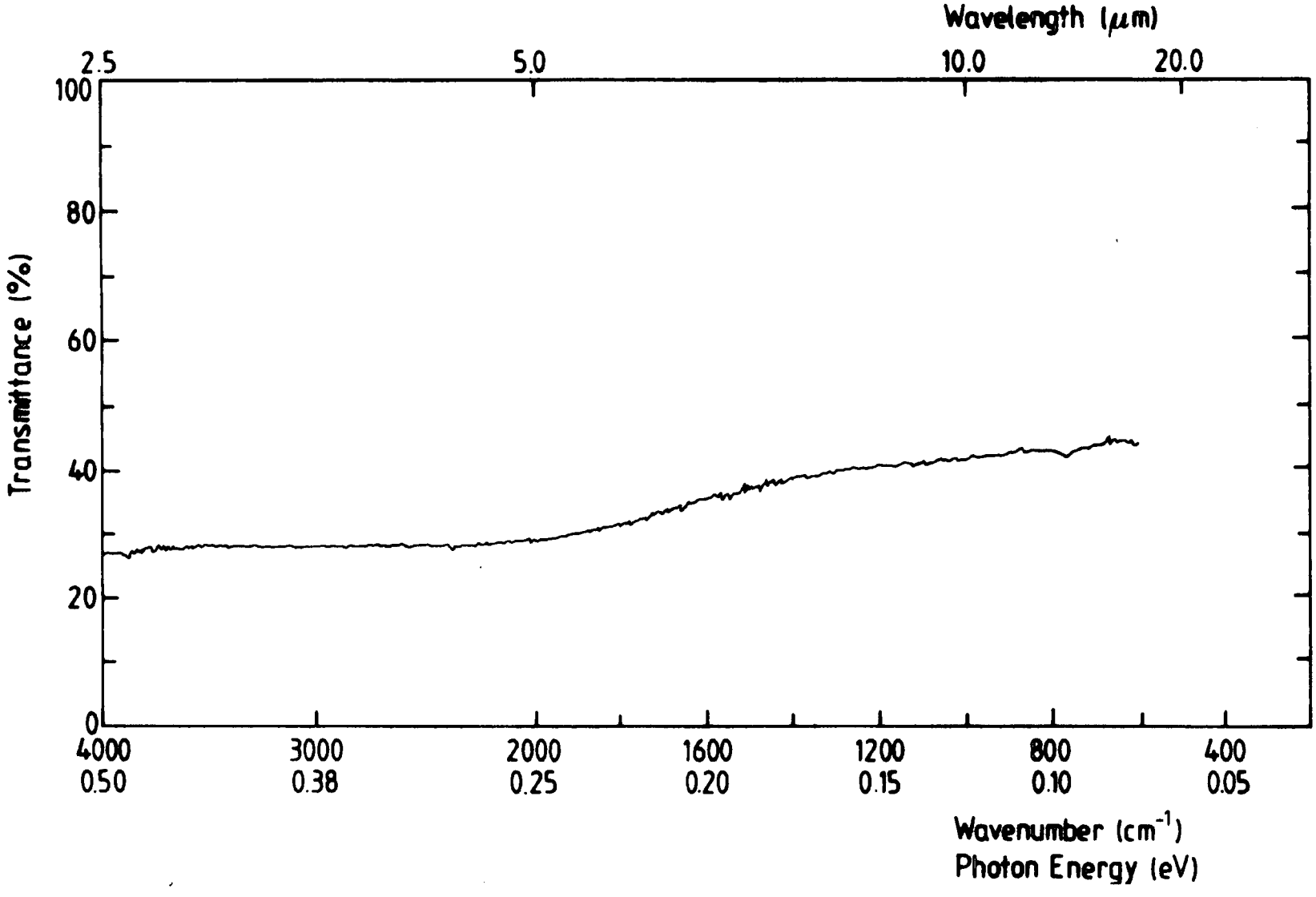

Fig.6.12. Infra-red transmission spectrum for a HgTe:ZnTe superlattice grown at 395°C. (MZTSL4)

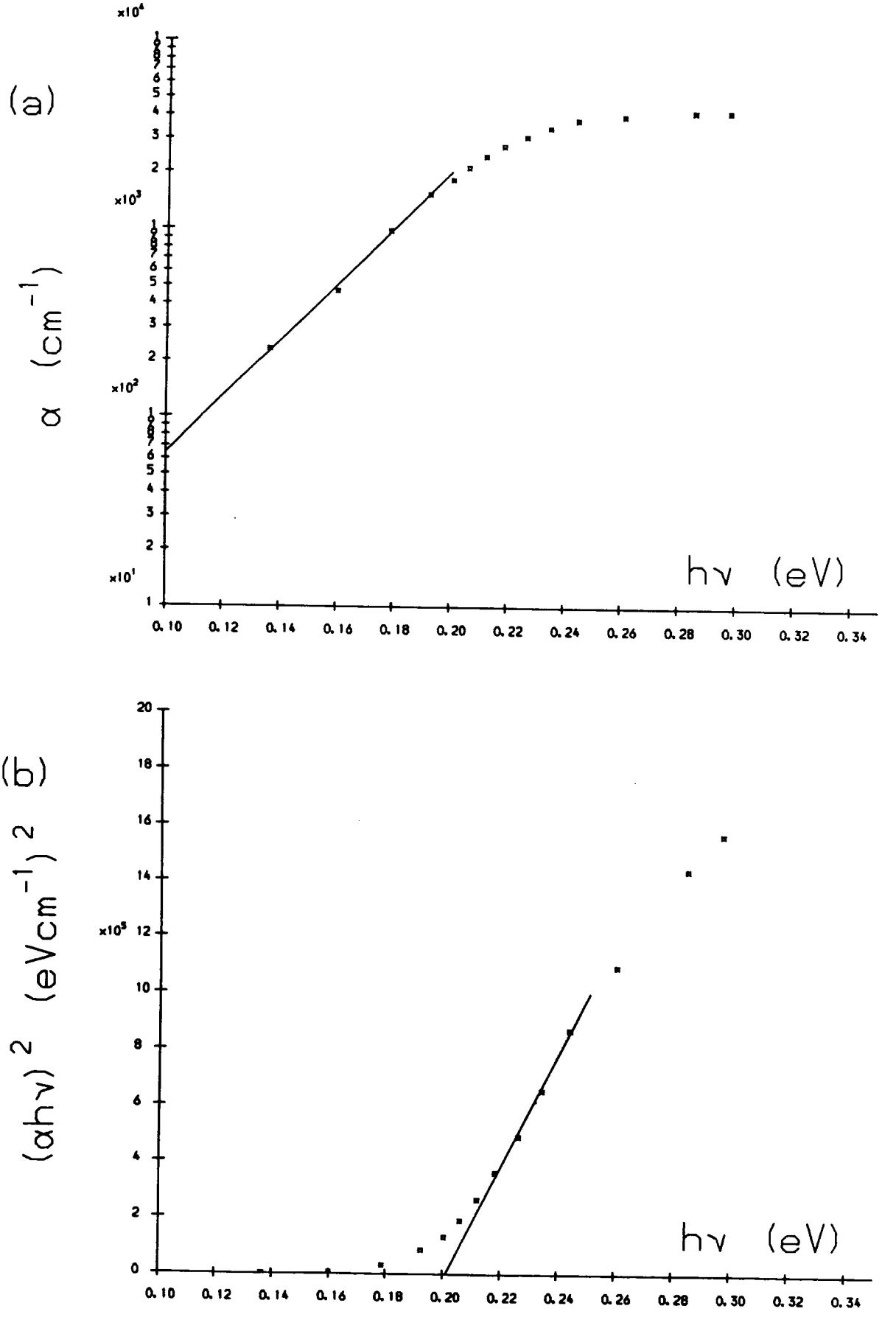

Fig.6.13.(a) Absorption coefficient (α) versus photon energy ($h\nu$) and (b) $(\alpha h\nu)^2$ versus $h\nu$ for a HgTe:ZnTe superlattice grown at 395°C. (MZTSL 4)

layer and that this has in turn led to a broadening of the optical absorption edge. For larger values of α up to the maximum of 4×10^3 cm^{-1} the dependence is parabolic. Extrapolating this parabolic region to $(\alpha h\nu)^2 = 0$ yields a value of 0.2 eV for the energy gap of the superlattice.

The energy levels in HgTe:ZnTe superlattices have been calculated[15] by Hall+++ using the Kronig-Penney model as reformulated for superlattices by Hung-Sik Cho et al[16] . In the calculations the superlattices were assumed to be free standing and fully strained. The strain in the constituent binary layers was calculated from simple elasticity theory. The effect of this strain on the energy levels was incorporated using deformation potentials as given by Wu and McGill[17] for HgTe and by Gil et al[18] for ZnTe. Conduction band effective masses of $0.01m_0$ and $0.116m_0$ were used for HgTe and ZnTe respectively while the heavy hole mass was taken to be $0.7m_0$ in both cases. The valence band offset ($E_{v,av}$ (HgTe) - $E_{v,av}$ (ZnTe)), where $E_{v,av}$ is the average energy of the light and heavy $\Gamma 8$ bands, was taken to be 250 meV as determined by Hsu et al[19] .

Here a superlattice composed of 130Å ZnTe barriers and 70Å HgTe wells as estimated for the superlattice above is considered. For this superlattice, the free standing lattice parameter, $a_{||}$, was calculated to be 6.176 Å using the expression of Mathieu et al.[20] :

$$a_{||} = \frac{l_{HgTe}/(a_{HgTe}(S_{11}+S_{12})_{HgTe}) + l_{ZnTe}/(a_{ZnTe}(S_{11}+S_{12})_{ZnTe})}{l_{HgTe}/(a^2_{HgTe}(S_{11}+S_{12})_{HgTe}) + l_{ZnTe}/(a^2_{ZnTe}(S_{11}+S_{12})_{ZnTe})} \qquad (6.3)$$

where l and S_{11} and S_{12} refer to layer thicknesses and elastic compliances respectively. In this calculation, the elastic constants were as given by Brice[21] for HgTe and by Kaldis[22] for ZnTe.

The band lineups of the binary constituents are shown in Fig. 14(a). Both the $\Gamma 8$ valence-like bands and the $\Gamma 6$ conduction-like band in the HgTe lie above the ZnTe valence bands. When the HgTe is placed under a biaxial compression corresponding to the 6.176Å in-plane lattice constant calculated for the superlattice (Fig. 14(b)), the energy gap is increased (made less negative) slightly and the light and heavy $\Gamma 8$ bands are split by the uniaxial component of the strain. In this diagram $E_{v,av}$ is represented by the dotted line. This splitting is the most significant effect the strain has on the

+++ D. Hall, Applied Physics Group, S.E.A.S., University of Durham

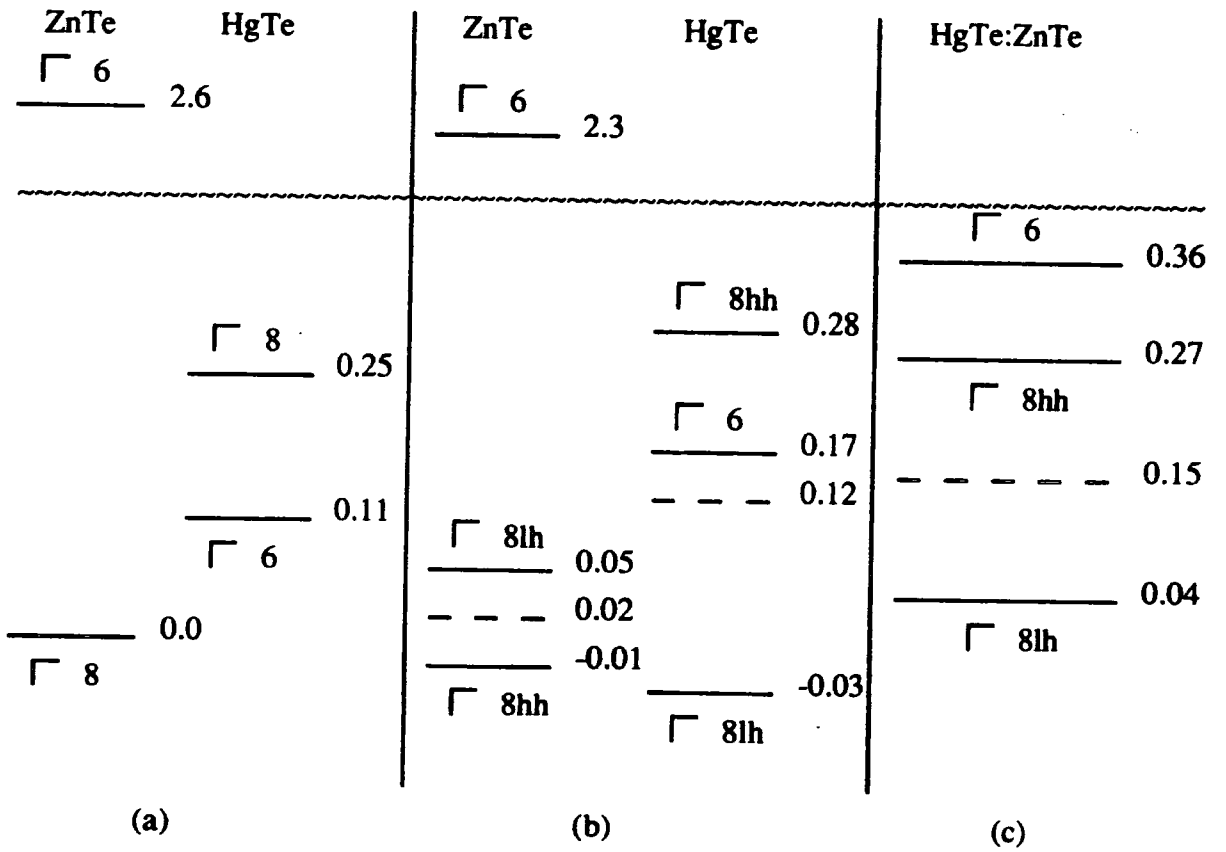

Fig.6.14. Electron energy levels in the HgTe:ZnTe system at 300K (eV).
(a) Bulk compounds (b) strained bulk compounds (c) superlattice

electronic structure. In contrast to the HgTe:CdTe case[23] , the heavy hole like Γ8 state moves up in energy while the light hole state moves down. This difference is due to the HgTe wells being under biaxial compression rather than biaxial tension as is the case for HgTe:CdTe superlattices. When the superlattice is formed, quantum confinement moves the Γ6 band up in energy by 190 meV leading to a conventional positive energy gap between the Γ6 conduction band and the Γ8 heavy hole valence band. The superlattice is type II for light holes with the Γ8 light hole band lying 230 meV below the heavy hole band and so this band is not expected to contribute to the electrical or optical properties.

The above analysis predicts a direct energy gap for the superlattice of 90 meV while the experimental value was 200 meV. This discrepancy may be explained by the effects of interface non-ideality and strain relief in the real structure and uncertainty in the input parameters for the theoretical model. In particular, this model is very sensitive to the exact value taken for the HgTe electron effective mass. The calculated energy gap may, however, be considered a good approximation to the observed value when it is considered that the alloy of corresponding composition would have an energy gap of ~ 1.3 eV.

6.4 HgTe:ZnTe Superlattices Grown at Reduced Temperature

Fig. 15.** is a T.E. micrograph showing part of an 80 period HgTe:ZnTe superlattice grown on a 1000 Å thick ZnTe buffer layer on {100} GaAs at 325°C using DIPT. For this sample the period was $\approx$ 45Å with approximately equal well and barrier thicknesses. In contrast to growth at 395°C , and despite a growth time 30% longer than for the sample discussed above, clear fringe contrast was observed throughout the layer. When the extremely short period is considered this result clearly demonstrates the feasibility of growing HgTe:ZnTe superlattices by thermal MOVPE at this temperature.

A DCXRD rocking curve obtained*** from part of the sample discussed above is shown in Fig. 16. In essence, the spectrum from the epitaxial layer consists of a very weak, broad peak due to the 1000 Å thick ZnTe buffer layer. This peak has a FWHM of approximately 1300 seconds of arc which is approximately twice that obtained from the 1 μm thick ZnTe layer considered in section 6.2. This result is consistent with the work of

** P.D. Brown, Applied Physics Group, S.E.A.S. University of Durham.

*** A. Turnbull, Solid State Physics Group, Department of Physics, University of Durham

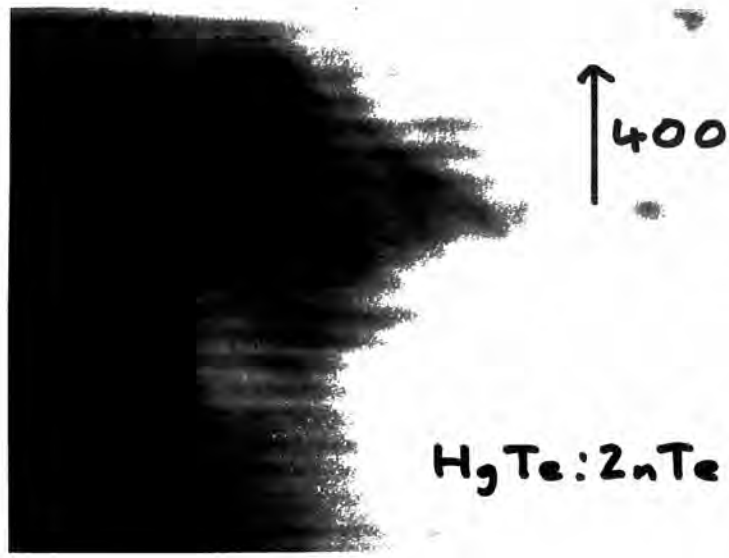

Fig.6.15. T.E. micrograph of a HgTe:ZnTe superlattice grown on a ZnTe buffer layer on {100} GaAs at 325°C .

(MZTSL16)

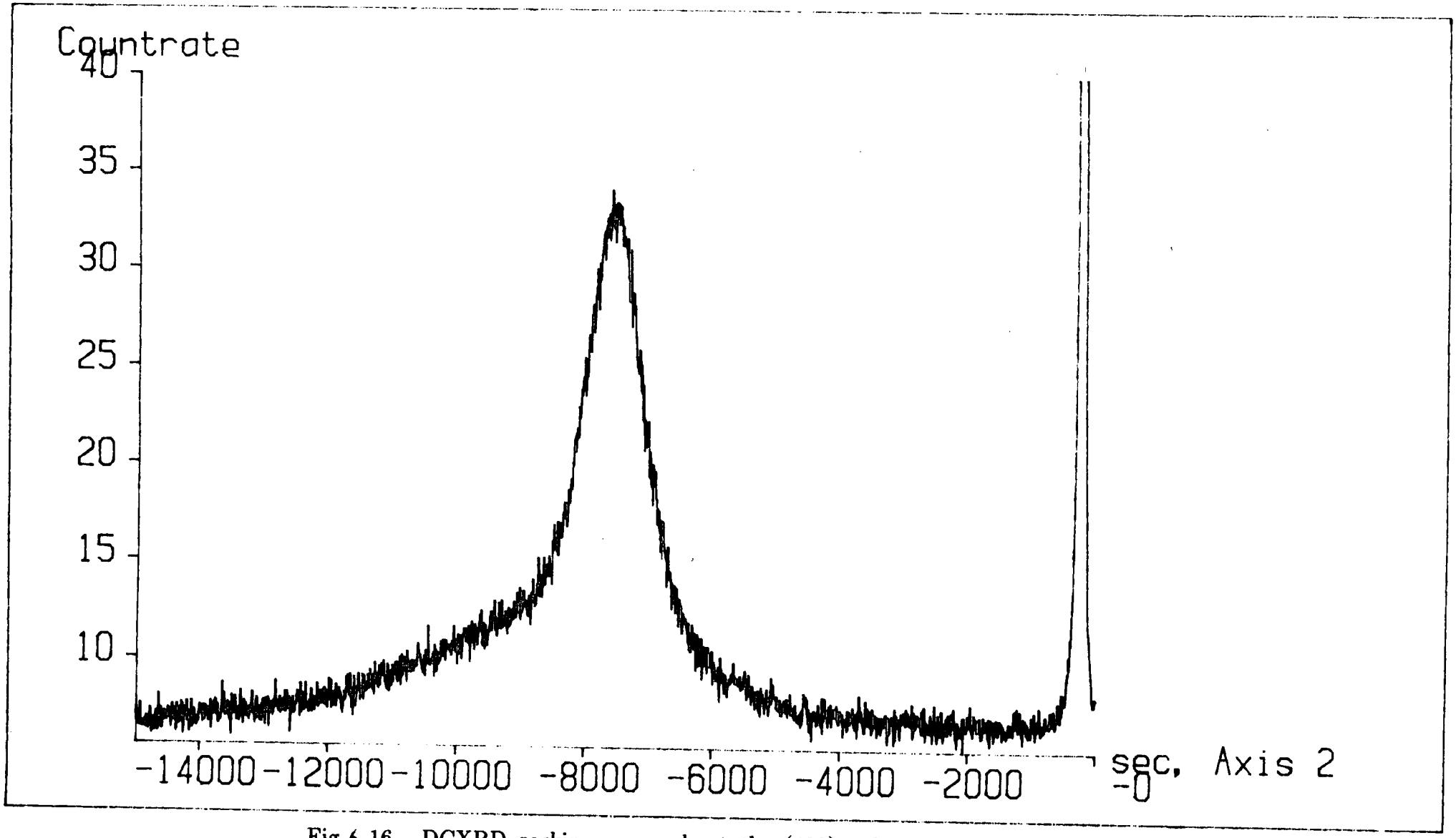

Fig. 6. 16. DCXRD rocking curve about the (400) reflection obtained from a HgTe:ZnTe superlattice grown on a ZnTe buffer on {100} GaAs at 325 °C. (MZT SL (6)

Shtrikman et al[3] , who found a decrease in rocking curve FWHM with increasing layer thickness for their ZnTe grown by MOVPE on {100} GaAs, and may be explained by a reduction in the density of threading dislocations as a layer is grown, as shown by TEM (Fig. 6.). The only evidence for the presence of the superlattice in this spectrum is a shoulder on the low angle side of the ZnTe peak. This corresponds to a layer with a larger lattice parameter than ZnTe and makes the peak asymmetric. The lack of a distinct peak from the superlattice indicates that, by the stringent criteria of DCXRD, the superlattice is of relatively poor quality. It is likely that a high density of dislocations in the superlattice is causing the X-ray diffraction peak to be broadened, thereby reducing its intensity to close to background levels. The use of a buffer layer lattice matched to the superlattice free standing lattice parameter such as the CdTe:ZnTe system discussed below is probably necessary to allow growth of good quality superlattices.

6.5 CdTe:ZnTe Superlattices

For growth at 410°C [2] , CdTe:ZnTe superlattices were also found to exhibit significantly better morphology than either of the constituent binary layers grown at the same temperature. Striations and cracking were, however, observed for growth on {100} GaAs. In contrast, layers grown at temperatures below 350°C using DIPT were found to be specular and essentially featureless under SEM observation.

RHEED provides a more sensitive test of morphology on the scale of the penetration depth of the incident electron beam. Figs. 17(a) and 17(b) show RHEED patterns obtained from two 0.65μm thick 100 period CdTe:ZnTe superlattices grown at 325°C in the same run (CZTSL8) on {100} and $\{\bar{1}\bar{1}\bar{1}\}$B oriented GaAs substrates respectively. Both demonstrate the good crystalline quality of the superlattices although the $\{\bar{1}\bar{1}\bar{1}\}$B oriented sample was twinned. Closer inspection reveals the presence of streaking perpendicular to the shadow edge for the $\{\bar{1}\bar{1}\bar{1}\}$B oriented sample. This is due to a smaller electron beam penetration depth and indicates[24] that the $\{\bar{1}\bar{1}\bar{1}\}$B surface is microscopically smoother than the {100} surface as was also the case for growth at 410°C .

A cross-sectional T.E. micrograph** of the {100} oriented sample referred to above is shown in Fig. 18. This clearly indicates the presence of a multilayer structure with a period of 65 Å although there is a large concentration of threading dislocations . Cibert

** P.D. Brown, Applied Physics Group, S.E.A.S. University of Durham.

et al[25] have shown experimentally by observations of RHEED oscillations in growth by Molecular Beam Epitaxy that the critical thickness for the growth of CdTe on ZnTe is 5 monolayers or $\sim$ 30 Å. Their work was performed using a growth temperature of 320°C and so is directly comparable with the work reported here. For a CdTe:ZnTe superlattice relaxed to its free standing in-plane lattice parameter, the critical thicknesses of the constituent binary layers would be expected to be more than twice the critical thickness for the growth of one binary on the other[26] . Accordingly, the maximum period of the corresponding superlattice comensurate with coherent growth would be expected to be greater than 120 Å. The superlattice considered here is well within that limit and so the large dislocation content may be associated with relaxtion of the superlattice from the substrate.

6.6 Discussion and Conclusions

The most significant result reported in this chapter is that the growth of HgTe:ZnTe superlattices by thermal MOVPE has been demonstrated. For growth directly onto GaAs substrates at 395°C using DET, interdiffusion of the constituent binary layers is significant, although the fact that a multilayer structure was observed at all indicates that interdiffusion in the HgTe:ZnTe system is much lower than in the HgTe:CdTe system as was expected. For growth at 325°C using DIPT interdiffusion was expected to be significantly reduced and this in fact proved to be the case as evidenced by the growth of a superlattice with a period of 45 Å. It should also be noted that this superlattice was grown on a ZnTe buffer layer on GaAs rather than directly onto GaAs as was the case for the superlattice grown at 395°C. This buffer layer was grown with the intention of reducing the lattice mismatch between the superlattice and its substrate and so was expected to improve the superlattice's structural quality. High concentrations of gallium are known to diffuse into II-VI epitaxial layers grown on gallium containing substrates and so it is possible that the buffer may also have reduced this effect. Both structural defects and the presence of gallium as a dopant may enhance interdiffusion between II-VI materials and it may be that some of the reduction in interdiffusion observed for the sample grown at 325°C can be attributed to the use of a buffer layer. A further and significant advantage of the lower growth temperatures is the greatly improved surface morphology which should enable the growth of highly two-dimensional structures. It is suggested that this effect is due to growth rates on the {100} and $\{\bar{1}\bar{1}\bar{1}\}$B planes being

more closely matched at the lower temperatures, thus preventing the development of facets. Whether this is related to the kinetics of the mercury, cadmium, zinc and tellurium ions on the growing surfaces or to the pyrolysis of the two different tellurium precursors is not clear.

For one superlattice, grown at 395°C , infra-red transmission measurements showed strong optical absorption at a wavelength considerably longer than expected for the equivalent alloy. This result clearly demonstrates the potential for using such superlattices as infra-red materials.

All of the superlattices considered in this chapter were grown either directly onto thin ZnTe buffer layers or directly onto the GaAs substrates. Although the shorter period superlattices were composed of individual layers sufficiently thin to be below the critical thickness for pseudomorphic growth, according to the work of Cibert et al.[25] , the resulting mismatch between the GaAs or ZnTe and the free standing lattice parameter of the superlattice led to the superlattices having an extremely high concentration of threading dislocations. This was reflected in the poor DCXRD spectrum obtained from one HgTe:ZnTe superlattice. Further progress in the development of these materials will probably require the use of buffer layers lattice matched to the free standing lattice parameter of the superlattice. As indicated in chapter two, the growth of suitable ternary alloys, such as (Cd,Zn)Te, directly may be difficult, and the use of an IMP type process impracticable due to the low interdiffusion coefficient. The use of a CdTe:ZnTe superlattice to perform this lattice matching may, however, be possible and initial studies of the growth of this system have been carried out. A further advantage of the use of strained layer superlattices as buffer layers is that the alternating strains in the system may act to bend over certain types of dislocations propagating from the superlattice/substrate interface. Such blocking of dislocations has been observed in CdTe:ZnTe superlattices grown by molecular beam epitaxy[27] .

In summary, the growth of HgTe:ZnTe superlattices by thermal MOVPE has been demonstrated and it has been shown that, in contrast to the HgTe:CdTe system, interdiffusion does not present a problem at the temperatures currently attainable with this growth technique. The applicability of this system to infra-red applications has also been demonstrated. Further work must be directed towards improving the structural quality of the superlattices. For growth by MOVPE, this may be achieved by the use of CdTe:ZnTe superlattice buffer layers lattice matched to the free standing lattice

parameter of the active HgTe:ZnTe superlattices.

REFERENCES

1. J.P. Faurie, S. Sivananthan, X. Chu and P.A. Wijewarnasuriya, Appl. Phys. Letters **48** (1986) 785.

2. P.A. Clifton, J.T. Mullins, P.D. Brown, G.J. Russell, A.W. Brinkman and J. Woods J. Crystal Growth **93** (1988) 726.

3. H. Shtrikman, A. Raizman, M. Oron and D. Eger J. Crystal Growth **88** (1988) 522.

4. P.D. Brown, A.P.C. Jones, G.J. Russell, J. Woods, B. Cockayne and P.J. Wright, in Microscopy of Semiconducting Materials 1987, Inst. Phys. Conf. Ser. **87**, Ed. A.G. Cullis 123.

5. A. Turnbull, Solid State Physics Group, Department of Physics, University of Durham, private communication.

6. D.J. Cole-Hamilton, Department of Chemistry, University of St. Andrews, private communication.

7. J.E. Nicholls, Department of Applied Physics, University of Hull, private communication.

8. T.D. McLean, T.M. Kerr, D.I. Westwood, J.D. Grange and I.J. Murgatroyd Inst. Phys. Conf. Ser. **No. 74**: Chapter 3

9. J. Petruzzello, D.J. Olego, X. Chu and J.P. Faurie J. Appl. Phys. **63** (1988) 1783.

10. J.E. Hails, G.J. Russell, A.W. Brinkman and J. Woods, J. Crystal Growth **79** (1986) 940.

11. J. Tunnicliffe, S.J.C. Irvine, O.D. Dosser and J.B. Mullin, J. Crystal Growth **68** (1984), 245.

12. R. Granger, C. Pobla, S. Rolland and R. Triboulet, (proceedings of the 4th International Conference on II-VI Compounds (1989), to be published in J. Crystal Growth)

13. Mei-Fan, S. Tang and D.A. Stevenson, J. Vac. Sci. Technol. **A6** (1988) 2650.

14. F. Urbach, Phys.Rev **92** (1953) 1324.

15. J.T. Mullins, P.A. Clifton, P.D. Brown, D.O. Hall and A.W. Brinkman, Mat. Res. Soc. Symp. Proc. (1990) to be published.

16. N. Hung-Sik Cho and P.R. Pracnal, Phys. Rev. B **36** (1987) 3237.

17. G.Y. Wu, and T.C. McGill, Appl. Phys. Letters **47** (1985) 634.

18. B. Gil, D.J. Dunstan, J. Calatayud, H. Mathieu and J.P. Faurie, Phys. Rev. B **40** (1989) 5522.

19. C. Hsu, Tran Minh Duc and J.P. Faurie, J. Vac. Sci. Technol. B **5** (1987) 1229.

20. H. Mathieu, J. Allegre, A. Chatt, P. Lefebvre and J.P. Faurie, Phys. Rev. B **38** (1988) 7740.

21. J.C. Brice in Properties of Mercury Cadmium Telluride, EMIS Datareviews Series No. 3.

22. H. Hartmann, R. Mach and B. Selle in: Current Topics in Materials Science **Vol 9** Ed. E. Kaldis North-Holland (1982).

23. J.R. Meyer, F.J. Bartoli, C.A. Hoffman and J.N. Schulman, Pyhsical Review B **38** (1988) 12457.

24. G.J. Russell Prog. Crystal Growth and Charact. **5** (1982) 291.

25. J. Cibert, Y. Gobil, Le Si Dang, S. Tatarenko, G. Feuillet, P.H. Jouneau and K. Saminadayar, Appl. Phys. Letters **56** (1990) 292.

26. J.W. Matthews and A.E. Blakeslee, J. Crystal Growth **32** (1976) 265.

27. P.D. Brown, T.D. Golding, G.J. Russell, J.H. Dinan and J. Woods, Inst. Phys. Conf. Ser. **100** (1989) 357.

7. Summary and Conclusions

The main themes of the work reported in this thesis were the characterisation of epitaxial layers of the narrow-gap semiconductor $Hg_{1-x}Cd_xTe$ and the development of growth techniques for, and initial characterisation of, HgTe:ZnTe superlattices as alternative narrow gap materials. $Hg_{1-x}Cd_xTe$ is a well established infra-red material while HgTe based superlattices, in general, may offer improved structural, optical and electrical properties over $Hg_{1-x}Cd_xTe$. The HgTe:ZnTe system, in particular, may be grown by thermal MOVPE. Subsidiary to the growth of the superlattices was the structural characterisation of epitaxial layers of ZnTe. Some initial studies were also performed on CdTe:ZnTe superlattices with regard to their application as buffer layers for HgTe:ZnTe superlattices.

In chapter two, the MOVPE system and the procedures used to grow these materials were described. A feature of this technique, in the case of II-VI materials, is that it is difficult to grow uniform ternary alloys directly due to the dominance of the growth of one of the binary constituents. Accordingly, the $Hg_{1-x}Cd_xTe$ layers were grown using the Interdiffused Multilayer Process (IMP). Consideration of the interdiffusion coefficient between HgTe and ZnTe suggested that growth of the HgTe:ZnTe superlattice system would be possible at the temperatures of thermal MOVPE and a suitable process, based on IMP, was developed. The process that evolved during the course of this work involved careful flushing of the growth reactor between the two phases of the growth cycle in order to overcome the supression of the HgTe growth by the ZnTe reaction. For the case of CdTe:ZnTe superlattice growth, although the conditions for the growth of the two binary compounds were more closely matched, it was still necessary to flush the reactor between the CdTe and ZnTe growth phases in order to obtain good control of layer thickness and composition.

The techniques used to characterise the epitaxial layers and superlattices were described in chapter three. This mainly involved a description of the apparatus which was designed and constructed to perform variable temperature Hall coefficient and resistivity measurements on $Hg_{1-x}Cd_xTe$ layers. This apparatus implemented a scanning current/voltage method in order to determine the Hall coefficient and resistivity using the van der Pauw technique. This method reduced the effect of poor contacts and noise and so enabled the extremely small Hall voltages produced by heavily doped $Hg_{1-x}Cd_xTe$ layers to be measured.

In chapter five, the properties of $Hg_{1-x}Cd_xTe$ layers were described. Infra-red transmission measurements showed the layers to be of excellent lateral uniformity thus demonstrating the utility of the IMP technique. The electrical measurements were interpreted using a multicarrier/multilayer model developed in chapter four to account for the effects of surface inversion layers and non-homogeneities in the material. This analysis showed the as grown layers to contain an extremely high concentration of acceptors and furthermore, the experimental data could only be fitted by assuming that the acceptor concentration was also highly non-uniform. The acceptors were assumed to be doubly ionised mercury vacancies which arise in $Hg_{1-x}Cd_xTe$ due to the weakness of the Hg-Te bond. Support for this assumption was given by the electrical data obtained from one sample which had been annealed at low temperature under conditions of almost saturated mercury vapour pressure and found to be n-type.

The properties of HgTe:ZnTe superlattices were described in chapter six. TEM observations clearly showed that thermal MOVPE offers sufficient control to grow such low dimensional structures although some interdiffusion occurred for growth temperatures in the region of 400°C . In contrast, for growth at $\sim$ 325°C interdiffusion did not present a problem. A further significant advantage of the reduced temperatures was that surface morphology was considerably improved thus enabling the growth of highly two-dimensional structures. The applicability of such materials to infra-red devices was demonstrated by strong infra-red absorption at wavelengths consistent with the formation of a superlattice rather than an alloy as calculated theoretically. Superlattices with energy gaps in the infra-red contain a much smaller proportion of HgTe than equivalent alloys and so should be structurally more stable. Furthermore, by growing a composite of two binaries rather than the alloy $Hg_{1-x}Cd_xTe$, the destabilising influence of Cd on the Hg-Te bond is eliminated. The increased structural stability of superlattices may be important for very long wavelength ($> 15\mu$m) infra-red detectors.

The large lattice mismatch between the constituent binary compounds in this system and between the superlattices and substrates led to the superlattices being highly faulted as determined by TEM and DCXRD. Further progress will require the use of buffer layers lattice matched to the free standing in-plane lattice parameter of the superlattices in order to improve their structural quality. As described above, however, the growth of uniform alloy buffers by MOVPE may be difficult. Accordingly, it was suggested that the use of CdTe:ZnTe strained layer superlattices as buffer layers is investigated.

APPENDIX I

$Hg_{1-x}Cd_xTe$ layers considered during the course of the work presented in this thesis. Experimental results reported in chapter five are marked by a hash symbol.

sample	IMP periods	ZnTe cap	RHEED	IR	electrical	comment
MCT37	70			#	#	non-uniform
GEC630	-				#	from GEC plc.
MCT71	70				#	1st attempt at annealing
MCT77	70			#	#	
MCT78	70			#	#	successful anneal
MCT84	40	*	#			1st capped sample high x
MCT86	40	*		#	#	

All of the above samples were grown on $\{\bar{1}\bar{1}\bar{1}\}$B oriented CdTe substrates under nominally identical growth conditions as described in chapter two.

APPENDIX II

Epitaxial layers of ZnTe considered during the course of the work presented in this thesis. Experimental results reported in chapter six are marked by a hash symbol.

sample	ZNTE12	ZNTE28	ZNTE29	ZNTE30	ZNTE35
growth temperature (°C)	395	350	325	300	350
tellurium precursor	DET	DIPT	DIPT	DIPT	DIPT
substrates					
{100} GaAs	*	*	*	*	*
$\{\bar{1}\bar{1}\bar{1}\}$B GaAs		*	*	*	
{100} GaSb		*	*	*	*
thickness (μm)	1.0	1.5	0.8	< 0.1	1.2
growth time (minutes)	40	60	60	60	60
SEM	#		#		
RHEED	#	#		#	
TEM					#
PL					#
DCXRD					#

APPENDIX III

HgTe:ZnTe and CdTe:ZnTe superlattices considered during the course of the work presented in this thesis. Experimental results reported in chapter six are marked by a hash symbol.

sample	MZTSL4	MZTSL12	MZTSL16	CZTSL8
growth temperature (°C)	395	395	325	325
tellurium precursor	DET	DET	DIPT	DIPT
substrates {100}GaAs	*	*	*	*
{$\bar{1}\bar{1}\bar{1}$}B GaAs		*		*
ZnTe buffer			*	
number of periods	40	60	80	100
period (Å)	200	125	45	65
SEM		#		
RHEED				#
TEM		#	#	#
calibrated EDX	#			
DCXRD			#	
IR transmission	#